# Influencing laser-accelerated ions by femtosecond-laser desorption

**Beeinflussung laserbeschleunigter Ionen mittels Femtosekunden-Laserdesorption**
Zur Erlangung des Grades eines Doktors der Naturwissenschaften (Dr. rer. nat.)
genehmigte Dissertation von M. Sc. Gabriele Hoffmeister aus Darmstadt
August 2014 — Darmstadt — D 17

TECHNISCHE UNIVERSITÄT DARMSTADT

Fachbereich Physik
Institut für Kernphysik

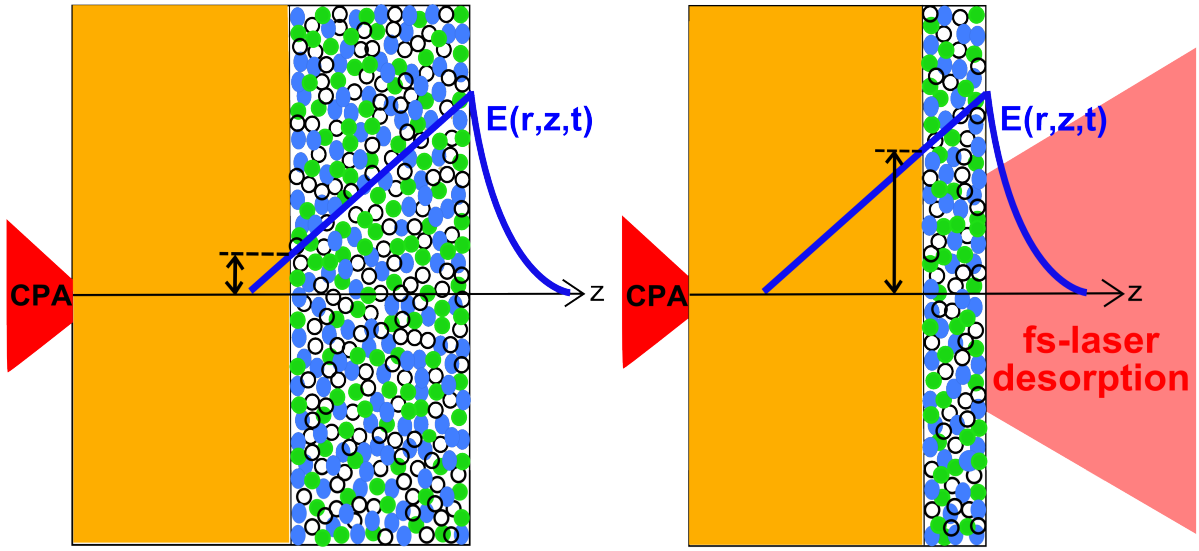

Influencing laser-accelerated ions by femtosecond-laser desorption
Beeinflussung laserbeschleunigter Ionen mittels Femtosekunden-Laserdesorption

Genehmigte Dissertation von M. Sc. Gabriele Hoffmeister aus Darmstadt

1. Gutachten: Prof. Dr. Markus Roth
2. Gutachten: Prof. Dr. Christina Trautmann

Tag der Einreichung: 27. Mai 2014
Tag der Prüfung: 07. Juli 2014

Darmstadt — D 17

# Zusammenfassung

Die vorliegende wissenschaftliche Arbeit untersucht die Beeinflussung von laserbeschleunigten Ionen durch die Femtosekunden-Laserdesorption. Durch die Bestrahlung metallischer Targetoberflächen mit ultrakurzen Laserpulsen moderater Fluenzen konnte ein sukzessives Abtragen von Oberflächenadsorbaten, bestehend aus Wasserdampf und Kohlenwasserstoffen, erzielt werden. Die anschließende Laser-Ionenbeschleunigung erfolgte somit von einer Targetoberfläche mit deutlich reduzierter Kontaminationsschicht, was sowohl die Ladungszustände der beschleunigten Ionen als auch deren Energien stark beeinflusste. Im Rahmen von separaten Laserdesorptionsmessungen wurde der für die Desorption relevante Bereich der Laserfluenz bestimmt. Die Kontaminationsschicht auf Metallfolientargets konnte hinsichtlich ihrer Dicke und atomarer Zusammensetzung charakterisiert werden.
Der im Rahmen dieser Arbeit untersuchte Mechanismus der Laser-Ionenbeschleunigung von dünnen Metallfolien beruht auf der *Target Normal Sheath Acceleration (TNSA)*. Hierbei beschleunigt ein kurzer Laserpuls mit einer Intensität größer als $10^{18}\,\mathrm{W/cm^2}$ Elektronen durch das Targetmaterial hindurch auf relativistische Energien. Beim Verlassen der Targetrückseite erzeugen die energiereichsten Elektronen ein quasistatisches elektrisches Feld in der Größenordnung von TV/m, welches die Atome auf der Targetrückseite feldionisiert und die erzeugten Ionen senkrecht zur Targetoberfläche beschleunigt. Die Oberflächenbeschaffenheit der Targetrückseite, und insbesondere die Zusammensetzung der adsorbierten Kontaminationsschicht, spielt dabei eine wesentliche Rolle, da die Targetrückseite als Ionenquelle dient. Ohne spezielle Targetbehandlung beobachtet man meist große Mengen von Protonen, gefolgt von Kohlenstoffionen, jedoch weniger ionisierte Atome des Targetmaterials, da die Kontaminationsschicht das elektrische Feld gegenüber den Targetatomen abschirmt.
Die im Zuge dieser Arbeit durchgeführte Bestrahlung der Targetrückseite mit ultrakurzen Laserpulsen moderater Fluenzen hat ein sukzessives, vorwiegend nichtthermisches Abtragen, d.h. ein Desorbieren, von Oberflächenadsorbaten zur Folge.

Ein bedeutender Teil dieser Arbeit beinhaltet die Untersuchung der Targetrückseite im Hinblick auf die Kontaminationsschicht. Dazu wurden Desorptionsmessungen unter Ultrahochvakuum-Bedingungen am Petawatt High Energy Laser for Heavy Ion eXperiments (PHELIX) der GSI Helmholtzzentrum für Schwerionenforschung GmbH durchgeführt. Gold-, Kupfer- und Aluminiumtargets wurden mit Laserpulsen mit einer Pulsdauer von 420 fs und einer Fluenz im Bereich von $(10 - 400)\,\mathrm{mJ/cm^2}$ über mehrere Minuten bei einer Repetitionsrate von 10 Hz bestrahlt. Der für die Desorption relevante Bereich der Laserfluenz betrug $(105.5 - 292.3)\,\mathrm{mJ/cm^2}$ für Gold und Kupfer sowie $(22.3 - 105.5)\,\mathrm{mJ/cm^2}$ für Aluminium. Durch laserinduzierte Desorption konnte im Folgenden ein komplettes Abtragen der Kontaminationsschicht erreicht werden. Die Messungen der desorbierten Gasteilchen ergaben eine gemittelte Flächendichte von $(4.27 \pm 1.28) \times 10^{16}$ Teilchen pro Quadratzentimeter und stellen eine zuverlässige Abschätzung der Kontaminationsschichtdicke auf Metallfolien im Bereich von wenigen Nanometern dar. Partialdruckmessungen zeigten, dass Wasserstoff sowie Kohlenstoffmonoxid mit jeweils $(40 \pm 10)\,\%$ den dominierenden Beitrag zur Zusammensetzung der Kontaminationsschicht leisten. Der große Anteil an Kohlenstoffmonoxid lässt darauf schließen, dass der Wasserstoffanteil im Wesentlichen von der Dissoziation leichter Kohlenwasserstoffe stammt. Diffusionsprozesse von Wasserstoff aus dem Targetinneren zur Tatgetoberfläche sollten zwar als Begleiteffekt zur Desorption von Oberflächenadsorbaten mitberücksichtigt werden, spie-

len jedoch nur eine untergeordnete Rolle. Die resultierenden atomaren Flächendichten von Wasserstoff, Kohlenstoff und Sauerstoff stimmen sehr gut mit Messungen auf Basis der elastischen Rückstreudetektionsanalyse (*elastic recoil detection analysis, ERDA*) überein.

Die Anwendung der Femtosekunden-Laserdesorption im Rahmen von Laser-Ionen-Beschleunigungsexperimenten zur TNSA zeigte einen starken Einfluss auf die Energiespektren der Ionen. Die Experimente hierzu fanden am Callisto-Lasersystem der Jupiter Laser Facility, Lawrence Livermore National Laboratory, statt, welches Intensitäten im Bereich von einigen $10^{19}\,\mathrm{W/cm^2}$ bei einer Pulsdauer im Bereich von 100 fs zur Verfügung stellte.
In der ersten Kampagne wurde die laserinduzierte Desorption bei einer Laserfluenz im Bereich von $(0.2-1.3)\,\mathrm{J/cm^2}$ und einer Pulslänge von 90 fs betrieben. Gold-, Kupfer- und Aluminiumfolien mit einer Dicke von 10 µm bzw. 11 µm wurden mit bis zu 165 Desorptionspulsen im 10 Hz-Takt bestrahlt, welche für ein sukzessives Abtragen von Oberflächenadsorbaten sorgten. Die folgende TNSA fand somit von einer Targetrückseite mit deutlich reduzierter Kontaminationsschicht statt. Dies führte sowohl zu einer Abnahme des Protonensignals um etwa eine Größenordnung als auch zu einer Verringerung der maximalen Protonenenergie um einen Faktor von bis zu vier. Eine Umverteilung der Ladungszustände von Kohlenstoff- und Sauerstoffionen zu höheren Ladungszuständen trat ein. Vor allem jedoch konnten Ionen des jeweiligen Targetmaterials beschleunigt werden, was ohne laser-induzierte Desorption nicht beobachtet wurde. Die experimentellen Ergebnisse wurden in *Phys. Rev. ST Accel. Beams* veröffentlicht [1] und konnten durch numerische Simulationen qualitativ bestätigt werden.
In der zweiten Kampagne fand die Laserdesorption bei einer Laserfluenz von $(0.5 \pm 0.2)\,\mathrm{J/cm^2}$ und einer Pulslänge von 250 fs im 10 Hz-Takt über eine längere Bestrahlungsdauer resultierend in mehreren tausend Desorptionspulsen statt. Targets bestehend aus einer 5 µm dicken Goldfolie mit einer aufgesputterten Nickelschicht im Nanometerbereich kamen mit dem Ziel zum Einsatz, nach einer vollständigen Entfernung der Kontaminationsschicht die Eindringtiefe des beschleunigenden elektrischen Feldes anhand der gemessenen TNSA-Ionenspektren zu bestimmen. Aufgrund gravierender Laserprobleme während der gesamten Strahlzeit konnte für dieses Vorhaben keine hinreichende Ionenbeschleunigung erzielt werden. Es wurden jedoch höhere Teilchenzahlen und Energien von beschleunigten Protonen sowie Kohlenstoffionen infolge der Langzeit-Desorption gemessen. Diese könnten aus einer weiteren zwischen Gold und Nickel eingebetteten Kontaminationsschicht stammen. Elektronenmikroskopische Aufnahmen der bestrahlten Targetfolien haben in einigen Fällen gezeigt, dass die Nickelschicht durch die Laserbestrahlung abgetragen wurde. Dies führte zum Freilegen der eingebetteten Kontaminationsschicht.

Die vorgestellten Ergebnisse konnten erste Schritte zur Bestimmung der Eindringtiefe des beschleunigenden elektrischen Feldes mittels Femtosekunden-Laserdesorption aufzeigen, welche die Beschleunigung der Ionen maßgeblich beeinflusst hat. Das erfolgte sukzessive Abtragen von Oberflächenadsorbaten kann zur Untersuchung der elektrischen Feldverteilung, welche für ein tieferes Verständnis der TNSA unabdingbar ist, einen wertvollen Beitrag leisten.

# Abstract

The present scientific work investigates the influence of laser-accelerated ions by femtosecond-laser desorption. The irradiation of metallic target surfaces with ultrashort laser pulses of moderate fluences enabled to successively remove surface adsorbates consisting of water vapor and hydrocarbon contaminations. Therefore, the subsequent laser-ion acceleration occurred from a target surface with a significantly reduced contamination layer which influenced both the charge states and the energies of the ions substantially. In the frame of separate desorption measurements the relevant laser fluence regime in which the desorption takes place was determined. The contamination layer could be characterized regarding its thickness as well as its atomic composition.

The laser-ion acceleration mechanism from thin metal foils investigated in the framework of this thesis bases on the *Target Normal Sheath Acceleration (TNSA)*. Hereby, a short laser pulse with an intensity exceeding $10^{18}\,\mathrm{W/cm^2}$ accelerates electrons through the target material to relativistic energies. When leaving the target rear side the most energetic electrons establish a quasistatic electric field in the order of TV/m, which field-ionizes the atoms on the target rear side and accelerates the generated ions normal to the target surface. The surface structure of the target rear side, and in particular the composition of the adsorbed contamination layer, plays a fundamental role since the target rear surface acts as the ion source. Without special target treatment one observes a large amount of accelerated protons, followed by carbon ions, but only very few ionized atoms from the target material itself because the contamination layer screens the electric field from the target atoms.
The irradiation of the target rear side with ultrashort laser pulses of moderate fluences conducted in this thesis induced a stepwise and predominantly nonthermal removal, i.e. desorption, of surface adsorbates.

An important part of this work represents the investigation of the target rear surface, especially of the contamination layer. Desorption measurements were carried out under ultrahigh vacuum conditions at the Petawatt High Energy Laser for Heavy Ion eXperiments (PHELIX) at GSI Helmholtzzentrum für Schwerionenforschung GmbH. Gold, copper and aluminum targets were irradiated with laser pulses having a pulse duration of 420 fs and a fluence in the regime of $(10-400)\,\mathrm{mJ/cm^2}$ over several minutes at a repetition rate of 10 Hz. The fluence regime, in which the desorption takes place, resulted in $(105.5-292.3)\,\mathrm{mJ/cm^2}$ for gold and copper as well as $(22.3-105.5)\,\mathrm{mJ/cm^2}$ for aluminum. Due to laser-induced desorption in this fluence regime a complete removal of the contamination layer could be realized. The measurement of the desorbed particles resulted in an averaged areal density of $(4.27 \pm 1.28)\times 10^{16}$ particles per square centimeter and represents a reliable estimate on the typical thickness of contamination layers on metal targets lying in the regime of few nanometers. Partial pressure measurements revealed that the dominant molecular contribution to the desorbed gases results from carbonoxide apart from hydrogen, each amounting to a fraction of $(40 \pm 10)\,\%$. The large fraction of carbonoxide allows to conclude that the hydrogen content stems predominantly from the dissociation of light hydrocarbons. Diffusion processes of hydrogen from the bulk to the surface have to be regarded as a concomitant effect to the desorption of surface adsorbates, but they should rather play a minor role. The resulting atomic areal densities for hydrogen, carbon and oxygen agree very well with measurements basing on the *elastic recoil detection analysis (ERDA)*.

The application of femtosecond-laser desorption in the frame of laser-ion acceleration experiments regarding the TNSA showed a strong influence on the ion spectra of the ions. The respective experiments took place at the Callisto laser system of the Jupiter Laser Facility, Lawrence Livermore National Laboratory, which delivered a laser intensity of several $10^{19}\,\mathrm{W/cm^2}$ at a pulse duration in the regime of 100 fs.
During the first campaign the desorption was applied at a laser fluence in the regime of $(0.2 - 1.3)\,\mathrm{mJ/cm^2}$ and a laser pulse length of 90 fs. Gold, copper and aluminum foils of thicknesses of 10 µm and 11 µm, respectively, were irradiated with up to 165 desorption pulses at 10 Hz providing a successive removal of surface adsorbates. Therefore, the subsequent TNSA occurred from a target rear surface on which the contamination layer was clearly diminished. This led both to a drop of the proton signal by about one order of magnitude and to a decrease of the maximum proton energy by up to a factor of four. A re-distribution of the charge states of carbon and oxygen ions to higher charge states occurred. But most notably, ions stemming from the respective target material were accelerated which was not observed without the application of laser-induced desorption. The experimental results were published in *Phys. Rev. ST Accel. Beams* [1] und could be validated qualitatively by numerical simulations.
During the second campaign the laser desorption at a fluence of $(0.5 \pm 0.2)\,\mathrm{J/cm^2}$ and a pulse length of 250 fs was carried out at 10 Hz over a longer period of time involving several thousand desorption pulses. Targets consisting of a 5 µm thick gold foil with a sputtered nickel layer in the nanometer regime were used with the aim of determining the penetration depth of the electric field by means of the resulting TNSA-ion spectra after having completely removed the contamination layer by desorption. Due to severe laser problems throughout the whole beam time the resulting ion acceleration was not sufficient for this experimental goal. But a higher amount and higher energies of accelerated protons as well as carbon ions were noted as a consequence of the long-term desorption. These could stem from an additional contamination layer embedded between gold and nickel. Electron microscopic images have shown in some cases that the nickel layer has been removed due to the laser irradiation. This might have laid open the embedded contamination layer.

The presented results could show the first steps towards a determination of the penetration depth of the accelerating electric field by applying femtosecond-laser desorption, which exerts a strong influence on the laser-ion acceleration. The successive removal of surface adsorbates can contribute significantly to the study of the electric field distribution, which is indispensible for a more profound understanding of the TNSA.

# Contents

# 1 Introduction

## 1.1 Motivation

Ultrahigh intensity lasers have become a fundamental device for addressing phenomena in high energy density physics. Their nowadays prominent role in scientific research can be traced back to the introduction of the technique of the chirped pulse amplification (CPA) [2] in 1985. This technique enables to generate very short laser pulses of femtosecond pulse duration and to access a laser peak power in the order of terawatt (TW) to petawatt (PW). When these pulses are focused down to a micrometer scale they achieve intensities well exceeding $10^{18}\,\mathrm{W/cm^2}$. This intensity characterizes the significant threshold at which electrons in the elecromagnetic field of the laser are accelerated to relativistic energies in only one laser oscillation cycle. The rising edge of the laser pulse impinging on a target is already intense enough to instantaneously ionize the target material on the irradiated surface. A plasma is created with which the main laser pulse interacts. The unbound plasma electrons oscillate with relativistic velocities in the laser field [3] which has an acceleration gradient exceeding $10^{12}\,\mathrm{V/m}$. This field strength is more than four orders of magnitude larger than that obtained by conventional particle accelerators operating at radio frequencies. Due to the relativistic Lorentz force the electrons do not only follow the transverse oscillations of the electric field component, which alone would lead to a net drift of zero, but they experience also a force in longitudinal direction by the magnetic field component. Additionally, the light pressure scaling with the laser intensity becomes important and pushes the electrons in forward direction. The electrons are accelerated to relativistic energies between several MeV and even GeV [4–6], but on an acceleration length in the order of micrometers to millimeters. This made it possible to enter a new physical regime of laser-matter interaction. Especially the acceleration of electrons and ions by high intensity laser fields has become a very extensive field of research with continuously growing interest.

Very intense ion beams of up to several ten MeV generated by the laser irradiation of thin target foils [7–10] were discovered in 1999. For example, the group of Snavely *et al.* [10] detected a proton beam containing roughly $2 \times 10^{13}$ particles of an energy larger than 10 MeV and with a maximum proton energy of 58 MeV when irradiating thin solid foil targets with a laser intensity of $3 \times 10^{20}\,\mathrm{W/cm^2}$. Apart from the common features of a high particle number and maximum energy, the protons were emitted from the non-irradiated, therefore called “rear” target surface as a rather collimated and laminar [11] beam perpendicular to the surface. The observation of the high quality characteristics of these ion beams such as high particle intensities [10, 12, 13], short pulse lengths and a very low transverse source emittance [11] exceeding the parameters of standard particle accelerators revolutionized the research field of laser-ion acceleration. A strong potential of numerous possible applications was recognized in those ion beams. Due to their low source emittance they can be inserted as ion sources of small dimensions [11, 14, 15] or as an ignitor beam in inertial confinement fusion [16], which was proposed as fast ignition [17, 18]. The short pulse length makes the laser-accelerated ions attractive as a diagnostics for imaging the fast electromagnetic field dynamics in a dense plasma [19, 20]. Due to their high beam laminarity they can also be applied for imaging objects complementary to X-rays, which became known as proton radiography [21, 22]. By isochoric heating of matter laser-accelerated ions can create high energy density states like warm dense matter [23–25] or

they can produce a high neutron yield by nuclear interactions with a secondary converter target in form of a laser-driven neutron source, as could be demonstrated recently [26]. As future perspectives, there are also considerations of integrating laser-accelerated ion beams into the particle therapy for the treatment of cancer [27–29]. However, it is still a long way to go for their implementation as ion therapy beams requiring ion energies of $(70-250)$ MeV with a very small energy spread of few per cent collimated in a bunch of about $10^{10}$ particles [30].

Shortly after the discovery of those high energetic ion beams the underlying mechanism of their generation and acceleration was introduced by Wilks *et al.* [31] in 2001. In this scenario, electrons having penetrated the target establish a dense electron sheath at a distance of few micrometers from the target rear side. This electron sheath provides a quasistatic electric field which field-ionizes the atoms on the target rear surface and accelerates these produced ions. Since their emission occurs normal to the target surface this mechanism was named *Target Normal Sheath Acceleration (TNSA)*. The acceleration of energetic ions stemming from the target rear surface could be proven experimentally [22, 32, 33]. It was identified as the dominating mechanism for short-pulse high-intensity lasers interacting with metal foils of thicknesses below 50 µm [34, 35] which became confirmed also by simulations [36].

Without special target treatment and independently from the target material protons are always accelerated first by the quasistatic electric field in the TNSA as they have the highest charge-to-mass ratio. These protons stem from water vapor and hydrocarbon contaminations which are always present on the target surface due to the air contamination of the target. Protons from the topmost contamination layer on the target surface are exposed to the highest field gradients and screen the electric field for protons and ions coming from the successive layers. The acceleration of particles from different target depths results in a broad ion energy distribution which becomes broader with increasing contamination layer thickness. The inhomogeneous electron distribution in the sheath additionally leads to an inhomogeneous accelerating field in the transverse direction [1].
The laser-driven ion beams generated by the TNSA therefore exhibit the common feature of a complete energy spectrum instead of a peaked energy distribution, as obtained in conventional particle accelerators. Their particle number decays exponentially for increasing energies until a certain energy cut-off is reached, at which the particle number drops to zero. This cut-off energy is referred to the obtained maximum ion energy, which was tried to increase over the years, and belongs to one of the most important parameters when comparing TNSA data. The analysis of experimental data on proton acceleration obtained at various laser facilities up to 2006 proclaimed a scaling of the proton energy with the product of laser intensity $I$ and the squared laser wavelength $\lambda_L$, i.e. $\propto I\lambda_L^2$ [37–39]. Numerical simulations could describe the maximum proton energy for a large range of laser and target parameters [38]. Theoretical models were developed by Mora *et al.* [40–42] describing the longitudinal ion acceleration dynamics by a plasma expansion model with which the maximum ion energy could be estimated.

Up to now the TNSA constitutes the most investigated laser-driven ion acceleration mechanism, so far, and provoked a vast amount of scientific publictions in the last fourteen years. Plenty of experiments studied the influence of the laser as well as target parameters on the TNSA. For example, the angular and spatial distribution of the TNSA ions was found to be strongly affected by the target characteristics and a strong correlation between the electron transport and the ion beam profile was found [22, 43]. Nevertheless, there are still many open questions on the details of the TNSA process itself. The distribution of the quasistatic electric field into the target is still not sufficiently ascertained. This is due to the complexity of the TNSA process itself depending on many different parameters of the laser as well as

the target properties. A single parameter study, in which only one parameter is changed, is impossible to perform since the other involved parameters, like e.g. the laser energy or the laser beam profile, will not be identical from shot to shot. Unlike the ion energy spectra, there is no experimental method available up to now which allows to directly measure the electrons establishing the electric sheath field. The only experimental way to get information about the electric field distribution constitutes its indirect access via the measured energy spectra of the accelerated ions, so far. One approach of analyzing the penetration depth of the electric field into the target was the ion acceleration from layers with thicknesses of only few nanometers which were buried in the target at depths between 3 nm and 200 nm [44]. The obtained results could indicate a decrease of the number of accelerated ions from a buried layer at a depth of 200 nm, but no quantitative results on the electric field strength could be obtained.

In the framework of this thesis, a different approach was chosen to address the TNSA electric field distribution including its penetration depth. Since the target rear surface acts as the ion source in the acceleration process, it is essential to learn more about its surface structure and, in particular, about the composition of the adsorbed contamination layer. An elaborate characterization of this contamination layer will furthermore help to improve numerical simulations of the TNSA process [45] and, thus, is of great value. The irradiation of the target rear surface with ultrashort laser pulses in the regime of femtosecond pulse durations and of moderate laser fluences below 1 J/cm$^2$ permits to remove monolayers of contaminants successively by a nonthermal desorption process. Unlike ns-laser ablation [46], the laser-matter interaction takes place on an ultrashort time scale such that the heating of the target surface becomes significantly suppressed [47]. In contrast to other target cleaning methods as resistive heating [48], also intermediate states between a fully contaminated target surface and a completely cleaned one are obtainable. This stepwise removal of adsorbates provides the possibility of scanning through the electric field distribution to a certain degree. As the target surface structure strongly influences the generated charge states and maximum energies of the TNSA ions, information about the spatial decrease of the TNSA electric field potential into the target can be deduced. From the maximum ion energies the passed potential difference in the quasistatic electric field can be calculated. The location of the atoms in the target determines to what extent the accelerating field potential is experienced by them. Thus, it determines their degree of ionization and their subsequent acceleration [1].
For future laser-ion acceleration projects with the aim of controllably accelerating ions of distinct charge state in a certain energy window a clear understanding of the TNSA electric field distribution as well as a characterization of the ion source are both indispensable.

## 1.2 Thesis structure

The content of this thesis can be divided into four parts.
The first part, chapter two, is dedicated to a theoretical introduction into the laser-matter interaction and refers predominantly to laser pulses of intensities exceeding $10^{18}$ W/cm$^2$. The interaction of an intense laser pulse with a single electron is taken into account before going over to a multiple particle description. Different mechanisms of laser-induced plasma generation are discussed, followed by an overview of the laser-plasma interaction. The absorption of the laser energy by electrons, the electron transport through the target and their energy transfer to the ions lead over to the laser-ion acceleration with a special focus on the Target Normal Sheath Acceleration (TNSA). Besides the physical description, a theoretical approach to model the TNSA is given and laser-ion acceleration mechanisms beyond the TNSA are briefly discussed.

The second part, chapter three, bases on the characterization of the target surface by the elastic recoil detection analysis providing information about the target surface composition.

The third part of the thesis, chapter four, is dedicated to the femtosecond-laser desorption. After an introduction into sorption processes on the target surface a phenomenological as well as numerical approach to laser-induced desorption will be given. This numerical approach was used to calculate the threshold fluence of laser desorption, at which melting of the target surface sets in. After the description of the experimental setup of the laser-induced desorption measurements as well as the discussion of the re-adsorption of gas molecules in the meantime of two consecutive laser pulses the obtained results are presented. Firstly, the data resulting from total pressure measurements are exhibited. Besides the experimental determination of the regimes of desorption as well as plasma formation, they focus on the estimation of the total amount of desorbed gas molecules having formed the contamination layer. Secondly, the data from the partial pressure measurements are discussed which provide an insight into the composition of the contamination layer. The chapter ends with concluding remarks on the obtained data.

The fourth and also main part of this thesis is treated in chapter five and focuses on the influence of fs-laser desorption on the TNSA. Since the experiments on this topic were performed at the Jupiter Laser Facility using the Callisto laser, an overview of the Callisto laser system is first given. The general experimental setup of such an experiment is presented, followed by the detailed setup of the two experimental campaigns. The methods of ion detection are discussed which include both the proton imaging by radiochromic films and the ion detection using a Thomson Parabola Spectrometer representing the main ion diagnostics in the performed TNSA experiments. Following to that, the results obtained from influencing the TNSA ion spectra by preceded laser-induced desorption are presented which are subdivided into two parts. In the first part, the fs-laser desorption is applied over a short period of time such that a maximum of 165 laser pulses irradiated the target surface before the main laser beam initiated the TNSA. The obtained results for the three used target materials gold, copper and aluminum were qualitatively validated by numerical simulations. The second part deals with the long-term laser desorption involving thousands of laser pulses. The experimental results on the application of both the short-term and the long-term laser desorption are discussed, interpreted and compared to each other.

The thesis ends with a conclusion of the obtained results and gives an outlook of future perspectives in the field of laser-ion acceleration.

# 2 Laser-matter interaction

Since the discovery of laser-accelerated ions in 1999 [9, 10, 12] this research field has gained a lot of attention by scientists worldwide. Due to the possibility of ion acceleration with compact laser systems of small dimensions compared to huge linear or circular accelerators the laser-ion acceleration has become a well-established issue in modern high energy density physics. Thanks to the availability of very powerful laser systems with very high intensities largely exceeding $I > 10^{18}\,\mathrm{W/cm^2}$ solid targets can rapidly be converted into the plasma state. In the plasma the electromagnetic laser field can couple to free electrons –at ultrahigh intensities $I > 10^{24}\,\mathrm{W/cm^2}$ also to ions– which rapidly begin to oscillate with velocities near the velocity of light. In this relativistic regime, nonlinear processes play an important role since the magnetic forces cannot be neglected anymore. The light propagation becomes dependent on the intensity and gets strongly influenced by the electron motion in the generated plasma.
In this chapter a theoretical description of the principles of laser-matter interaction is presented. A deeper insight into this topic is given in [49–51] on which this chapter bases. In section 2.1 the influence of an intense laser field on an electron in the single-particle picture is explained. The ponderomotive force is introduced which arises due to the nonuniform spatial intensity distribution of the laser pulse and pushes the plasma electrons out of regions of higher intensity. Section 2.2 considers the propagation of laser light in the generated plasma. Intense laser pulses are usually preceded by prepulses, amplified spontaneous emission (ASE) or simply by a rising intensity edge which already suffices to create a preplasma on the irradiated target surface. The laser propagation into this plasma is influenced by the plasma properties, e.g. its density and the induced plasma oscillations. The plasma electrons can absorb energy from the laser via different mechanisms, presented in section 2.3, and get accelerated. Their transport through the target is described in section 2.4. The most energetic electrons are capable to escape from the non-irradiated target rear surface into the vacuum where they build up a strong electron sheath. This charge separation generates a strong electric field which is able to ionize atoms on the rear surface and to accelerate these ions normal to the target surface. This laser-ion acceleration mechanism named target normal sheath acceleration (TNSA) is presented in more detail in section 2.5. The chapter concludes with a brief discussion on laser-ion acceleration mechanisms beyond the TNSA.

## 2.1 Single electron motion in a laser field

For the study of the interaction of a laser pulse with a single electron the laser pulse is considered as a plane electromagnetic, linearly polarized wave propagating in z-direction. Its electric and magnetic field components are given by

$$\mathbf{E}(\mathbf{r},t) = E_0(t)\,\mathrm{e}^{i\left(kz-\omega_L t\right)}\mathbf{e}_x\,, \tag{2.1}$$

$$\mathbf{B}(\mathbf{r},t) = B_0(t)\,\mathrm{e}^{i\left(kz-\omega_L t\right)}\mathbf{e}_y\,, \tag{2.2}$$

with $B_0 = E_0/c$ and $c$ as the light velocity. The quantities $E_0(t)$ and $B_0(t)$ describe the time-dependent field amplitudes, $\omega_L$ is the laser angular frequency, $k = \omega_L/c$ indicates the absolute value of the laser wave vector and $\mathbf{e}_{x,y}$ denote the unit vectors in x- or y-direction, respectively,

both perpendicular to the laser propagation direction. The intensity of this electromagnetic wave in vacuum corresponds to the cycle-averaged modulus of the directional energy flux density, the Poynting vector **S**,

$$I = \left|\overline{\mathbf{S}}\right| = \frac{1}{\mu_0}\left|\overline{\mathbf{E}\times\mathbf{B}}\right| = \frac{c\epsilon_0}{2}E_0^2, \tag{2.3}$$

where $\mu_0$ is the magnetic constant (permeability) and $\epsilon_0$ the electric constant (permittivity). In the presence of the electromagnetic laser field a single electron gets accelerated and deflected. The relativistic equation of motion of the electron in vacuum is given by the Lorentz force

$$\frac{d\mathbf{p}}{dt} = m_e\gamma\frac{d\mathbf{v}}{dt} = -e\left(\mathbf{E}(\mathbf{r},t) + \mathbf{v}\times\mathbf{B}(\mathbf{r},t)\right) \tag{2.4}$$

acting on the electron, where $\gamma = 1/\sqrt{1-\beta^2} = \sqrt{1+\mathbf{p}^2/\left(m_e c\right)^2}$ is the relativistic factor and $\beta = |\mathbf{v}|/c$. In case of a non-relativistic electron velocity $\beta \ll 1$ which corresponds to the lowest order, i.e. in the linear approximation of equation (2.4), the magnetic part of the Lorentz equation can be neglected such that the equation of motion of the electron results in a harmonic oscillatory motion in direction of the electric field with the quiver velocity

$$\mathbf{v}_{osc}(t) = \frac{-ie}{m_e\omega_L}\mathbf{E}(\mathbf{r},t) \tag{2.5}$$

and with the electron position

$$\mathbf{r}(t) = \frac{e}{m_e\omega_L^2}\mathbf{E}(\mathbf{r},t). \tag{2.6}$$

During the laser pulse the electron oscillates perpendicular to the laser propagation direction with a maximum elongation being much smaller than the laser wavelength $\lambda_L$, i.e. $r_0 = eE_0/m_e\omega_L^2 \ll \lambda_L$, and comes to rest after the laser pulse without being displaced.

For laser pulses with electric field amplitudes $E_0 > 3.22\times10^{12}$ V/m, which according to equation (2.3) applies to intensities exceeding $1.37\times10^{18}$ W/cm$^2$, the electron motion becomes relativistic. In this case, the dimensionless electric field amplitude, which is defined as

$$a_0 \equiv \frac{eE_0}{m_e c\omega_L} = 0.854\times10^{-9}\left(I\left[\mathrm{W/cm^2}\right]\right)^{\frac{1}{2}}\lambda_L\left[\mu\mathrm{m}\right], \tag{2.7}$$

becomes larger than one and the nonlinear $\mathbf{v}\times\mathbf{B}$ term in the Lorentz equation is not negligible anymore. The parameter $a_0$ provides a convenient measure of the relativistic character of the interaction. For $a_0 \ll 1$ the electron motion can be treated classically while in case of $a_0 \approx 1$ the electron motion enters the relativistic interaction regime and for $a_0 \gg 1$ the interaction becomes ultra-relativistic. For example, in case of a titanium:sapphire (Ti:sapphire) laser[1] having a wavelength of $\lambda_L = 800\,\mathrm{nm}$ and with an assumed intensity of $1\times10^{19}$ W/cm$^2$, the electron motion is already relativistic for $a_0 \geq 2.16$. The following chapters will mainly focus on that relativistic regime since the experiments presented in this thesis were performed at values of $a_0$ ranging between three and six.

The relativistic electron motion in a plane electromagnetic wave can be solved exactly [49].

[1] This notation refers to the lasing medium, a crystal of sapphire ($Al_2O_3$) which is doped with titanium ions.

The electron dynamics is then described by the full Lorentz equation (2.4) including its magnetic interaction part and by adding the energy equation

$$\frac{d}{dt}\left(m_e\gamma c^2\right) = -e\,\mathbf{v}\mathbf{E}. \tag{2.8}$$

While the electric part of the Lorentz force points into the direction of the electric field, its magnetic part $F = evB \propto a_0^2$ is orientated along the propagation direction of the electromagnetic wave, thus, perpendicular to the magnetic field direction. The relativistic electron motion will no longer be a linear oscillation in direction of the electric field but will be described by a more complex trajectory. The electric and magnetic fields can be expressed by the vector potential $\mathbf{A} = \mathbf{A}(z,t)$, for which $\mathbf{e}_z \cdot \mathbf{A} = 0$ and with the scalar potential being zero in vacuum, which leads to

$$\mathbf{E} = -\frac{1}{c}\partial_t\mathbf{A}, \qquad \mathbf{B} = \nabla\times\mathbf{A} = \mathbf{e}_z\times\partial_z\mathbf{A}. \tag{2.9}$$

This ansatz is inserted in equation (2.4) and (2.8), assuming that the electron initially is at rest before the electromagnetic wave arrives, i.e. $t = 0$, $p_z = 0$, $p_x = 0$, $\gamma = 1$. After some algebra following [49, 51] the equation of motion for an electron in a linearly polarized electromagnetic wave results in

$$p_z = \frac{a_0^2}{4}m_e c\left[1+\cos 2\phi\right], \qquad z = \frac{a_0^2 c}{4\omega_L}\left[-\phi - \frac{\sin 2\phi}{2}\right] \tag{2.10}$$

$$p_x = a_0 m_e c\cos\phi, \qquad x = -\frac{a_0 c}{\omega_L}\sin\phi \tag{2.11}$$

with the phase $\phi = kz - \omega_L t$. The relativistic electron motion consists of a net drift superposed with an oscillatory motion of the double laser frequency $2\omega_L$ in propagation direction of the electromagnetic wave (z-direction), while in direction of the electric field (x-direction) the electron oscillates with the single laser frequency $\omega_L$. Averaging over one oscillation period the electron experiences a net drift

$$\bar{z} = \frac{a_0^2}{a_0^2+4}ct = v_d t \tag{2.12}$$

where $v_d = a_0^2/\left(a_0^2+4\right)$ corresponds to the cycle-averaged drift velocity. Contrary to the non-relativistic case, in which the electron will be at the same position after the laser pulse has passed, the electron will be displaced in laser propagation direction after the pulse has passed. However, the electron will not have gained kinetic energy under the assumptions made above concerning the electromagnetic wave. The *Lawson-Woodward* theorem [52, 53] stating that no energy can be gained by electromagnetic fields in vacuum, thus, remains valid. However, the theorem underlies the constraints that (i) the region of interaction is infinite, (ii) the laser fields are in vacuum with no walls or boundaries present, (iii) the electron is highly relativistic ($v \approx c$) along the acceleration path, (iv) no static electric or magnetic fields are present and (v) nonlinear effects due to ponderomotive, $\mathbf{v}\times\mathbf{B}$, and radiation reaction forces are neglected. For a nonzero net energy gain at least one of these requirements has to be violated. In real laser-matter interactions plasma is generated, so the assumption of a vacuum condition does not hold anymore. The plasma medium gives rise to other electronic interaction channels like plasma beat waves [54, 55] and nonlinear effects will certainly occur. Furthermore, the laser pulse has a limited pulse duration which sets up a boundary of the electromagnetic wave in space, thus, limiting the interaction distance.

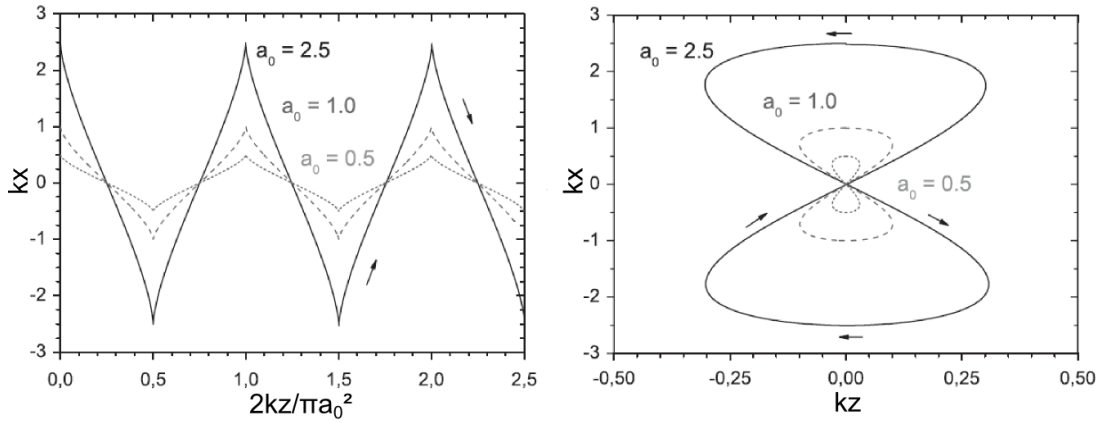


**Figure 2.1:** Electron trajectories induced by a plane linearly polarized laser pulse with different values of the dimensionless electric field amplitude $a_0$. On the left, the electron motion is seen from the laboratory frame while on the right, it is seen from the frame moving with the cycle-averaged drift velocity of the electron. The picture was taken from [56].

In Figure 2.1, the electron trajectories in dimensionless spatial coordinates, according to equations (2.10) and (2.11) with $k = \omega_L/c$, are shown for three different parameters $a_0 = 0.5, 1.0, 2.5$. These correspond to intensities of $5 \times 10^{17}\,\mathrm{W/cm^2}$, $2 \times 10^{18}\,\mathrm{W/cm^2}$ and $1.4 \times 10^{19}\,\mathrm{W/cm^2}$ for $\lambda_L = 800\,\mathrm{nm}$. The left picture demonstrates the electron trajectory as they are seen from the laboratory system while the right image shows the electron trajectories for the same values of $a_0$, but seen from a frame moving with the drift velocity $v_d$ of the electron. Here, the electron movement describes the figure of an "eight".

### 2.1.1 Ponderomotive force

The equations of motion in the previous section were derived under the assumption of a plane linearly polarized electromagnetic wave in vacuum varying only slowly in time and whose electric and magnetic field amplitudes are spatially constant. These idealized properties are far from being real for the laser pulses which are applied in experiment. For example, the laser pulses used for the experiments concerning this thesis have a short pulse duration in the sub-ps regime, thus, being limited in time and space. They are tightly focused to the target creating high radial intensity gradients over a distance of a few micrometers and their radial electromagnetic field distribution usually corresponds to a Gaussian beam shape, i.e. it is not constant in space anymore. Due to the Gaussian beam shape the laser intensity in the center is highest and decreases radially. Also in propagation direction the laser intensity profile is not constant but has a rising (and falling) edge.
Mathematically, the electromagnetic fields can be expressed by an envelope function [49] which contains the spatial information about the transversal and longitudinal beam profile varying slowly in time with respect to the oscillation period $T = 2\pi/\omega_L$ and a fast oscillating part leading to

$$\mathbf{E}(\mathbf{r},t) = \Re\left(\widehat{\mathbf{E}}(\mathbf{r},t)\,\mathrm{e}^{-i\omega_L t}\right) = \frac{1}{2}\widehat{\mathbf{E}}(\mathbf{r},t)\,\mathrm{e}^{-i\omega_L t} + \text{c.c.}\,, \tag{2.13}$$

$$\mathbf{B}(\mathbf{r},t) = \Re\left(\widehat{\mathbf{B}}(\mathbf{r},t)\,\mathrm{e}^{-i\omega_L t}\right) = \frac{1}{2}\widehat{\mathbf{B}}(\mathbf{r},t)\,\mathrm{e}^{-i\omega_L t} + \text{c.c.}\,. \tag{2.14}$$

An electron which is initially at rest on the laser axis will be shifted towards a region of lower intensity during the first half cycle of the laser wave. In the second half cycle the electron experiences a lower electric field on its new position and therefore cannot travel back the whole distance of its shift. It will not stop at its original position but at a displaced one. The next half laser cycle pushes the electron again out of the region of higher intensity while in the following half laser cycle the restoring force is again decreased, and so on. As a consequence, the electron gets expelled from the region of locally higher intensity. The force which is responsible for this process is the so-called *ponderomotive force* and is derived from a first order perturbation analysis of the Lorentz equation (2.4) around the oscillation center. The electric field amplitude is no longer constant in space but has a radial intensity dependence according to the Gaussian beam profile and since this spatial variation of the field envelope is small it can be expanded in a Taylor series resulting in

$$\mathbf{E}(\mathbf{r},t) = E(\mathbf{r}=\mathbf{r}_0,t) + \mathbf{r}\,\nabla\mathbf{E}(\mathbf{r},t) + O\left(\mathbf{r}^2\right). \tag{2.15}$$

Inserting this ansatz in the Lorentz equation the equation of motion for an electron oscillating near the center of the focused beam in the nonrelativistic limit $\beta \ll 1$ becomes

$$\frac{\partial \mathbf{v}^{(2)}}{\partial t} = -\frac{e^2}{m_e^2\omega_L^2}\mathbf{E}(\mathbf{r},t)\,\nabla\mathbf{E}(\mathbf{r},t) = -\frac{e^2}{2m_e^2\omega_L^2}\underbrace{\nabla\left(\mathbf{E}^2(\mathbf{r},t)\right)}_{\propto\nabla I} \tag{2.16}$$

where the $^{(2)}$ stands for the second order term of the Taylor expansion of equation (2.15). The $\nabla\left(\mathbf{E}^2(\mathbf{r},t)\right)$ -term consists of terms varying with a frequency of $0\omega_L$ as well as $2\omega_L$. The zero-frequency term describes the averaged particle motion varying only slowly in time. It serves as the physical quantity describing the oscillation center dynamics which is superposed with a fast oscillating term of $2\omega_L$. The ponderomotive force is obtained by multiplying equation (2.16) with the electron mass $m_e$ and by taking the cycle-average. Since the $2\omega_L$-term is neglected due to $\overline{\cos 2\phi} = 0$, the ponderomotive force results in

$$\mathbf{F}_p = -\frac{e^2}{4m_e\omega_L^2}.\nabla\left(\widehat{\mathbf{E}}\cdot\widehat{\mathbf{E}}^*\right) = -\nabla\Phi_p\,. \tag{2.17}$$

It corresponds to the gradient of the cycle-averaged oscillation potential of the electron which actually is the cycle-averaged oscillation energy of an electron at the oscillation center position.

While the presented nonrelativistic derivation of the ponderomotive force underlies certain constraints, like the perturbation analysis of the momentum, the assumption of harmonic electromagnetic fields as well as oscillation amplitudes much smaller than the laser wavelength, a relativistic expression of the ponderomotive force has been derived by Bauer *et al.* [57] without those limitations. From the relativistic Hamiltonian of a point charge q in an electromagnetic field having the canonical momentum $\mathbf{p} = \gamma m\mathbf{v} + q\mathbf{A}$

$$H = \sqrt{m^2c^4 + c^2\left(\mathbf{p} - q\mathbf{A}\right)^2} + \Phi \tag{2.18}$$

the particle motion is exactly solvable for a monochromatic wave in vacuum, where the scalar potential $\Phi$ can be set to zero since there are no charges (Coulomb gauge). The cycle-averaged oscillation energy of an electron in the oscillation center gained by the relativistic ponderomotive potential is then given by

$$H_0 - m_ec^2 = m_ec^2\left(\sqrt{1 + \frac{e^2}{\alpha m_e^2c^2}\,(\mathbf{A}\cdot\mathbf{A}^*)} - 1\right) = m_ec^2\left(\overline{\gamma} - 1\right) = W_{\text{pond}} = \overline{\Phi}_p \tag{2.19}$$

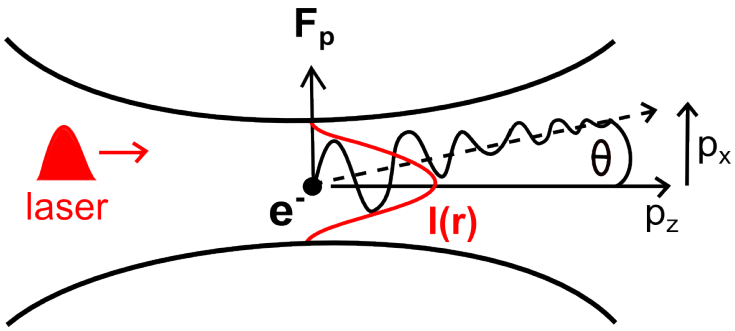


**Figure 2.2:** Schematic description of the electron motion in the focus of a Gaussian laser beam with intensity profile $I(r)$: The ponderomotive force $\mathbf{F}_p$ expels the electron from the region of higher intensity in direction of the negative electric field gradient ($p_x$) while the relativistic drift pushes the electron in laser propagation direction ($p_z$) [51].

with $\alpha = 2$ for a linearly polarized wave and $\alpha = 1$ for a circularly polarized wave and where $\overline{\gamma}$ denotes the cycle-averaged gamma-factor $\overline{\gamma} = \sqrt{1 + a_0^2/\alpha}$.
For linearly polarized laser light the relativistic ponderomotive force in the oscillation center frame, in which the electron initially is at rest, is obtained by

$$\mathbf{F}_p = -\nabla W_{\text{pond}} = -m_e c^2 \nabla \overline{\gamma} = -m_e c^2 \nabla \left( \sqrt{1 + \frac{a_0^2}{2}} \right). \tag{2.20}$$

While the ponderomotive force expels the electron in direction of the negative gradient of the electric field the laser pulse pushes the electron in its propagation direction by its light pressure, thereby exerting a relativistic drift motion on the electron.

The influence of the ponderomotive force on a single electron in a relativistic laser field is shown in Fig. 2.2. Since the electron momentum in laser propagation direction is conserved according to the Hamiltonian equations of motion, a proportional amount of momentum in propagation direction of the laser wave, $p_z = W_{\text{pond}}/c = m_e c\left(\overline{\gamma} - 1\right)$, has to be delivered from the electromagnetic wave to the electron. Together with the relativistic energy relation $E^2 = m_e^2 c^4 + c^2\left(p_x^2 + p_z^2\right)$, the angular spread of the electron trajectory can then be calculated and yields

$$\tan\theta = \frac{p_x}{p_z} = \sqrt{\frac{2}{\bar{\gamma} - 1}}. \tag{2.21}$$

This relation shows that for laser intensities of $a_0 > 4$ (i.e. for $I > 3.4 \times 10^{19}\,\text{W/cm}^2$ and $\lambda_L = 0.8\,\mu\text{m}$) the acceleration of the electron in forward direction dominates, i.e. $v_z > v_x$. A detailed derivation of the relativistic single electron dynamics comparable to equation (2.10) and (2.11) can be found in [50].

## 2.2 Ionization mechanisms and laser propagation in plasma

In this section the basic processes of the interaction of intense laser light with matter, its transition into the plasma state and the absorption of laser energy by charged particles are described. The generated plasma state is a quasineutral gas consisting of free electrons and ions which both can interact with the electromagnetic laser wave and which can be accelerated by different mechanisms. These laser-particle acceleration mechanisms depend on several parameters

like the laser intensity $I$, its pulse duration $\tau_L$, its incidence angle $\theta$ and the laser prepulse conditions. But they depend also on the target material itself, e.g. the target geometry, its thickness, its conductivity or the respective surface conditions.

The achievement of high laser pulse intensities in the order of $I \geq 10^{18}\,\mathrm{W/cm^2}$ depends on the one side on the focusing quality and the energy of the laser beam and on the other side on the laser pulse duration. However, when talking about intense short laser pulses in the range of $\tau_L \leq 1\,\mathrm{ps}$ it has to be considered that the intensity increase cannot occur arbitrarily sharply, i.e. the temporal profile of the pulse does not correspond to an ideal Gaussian beam. The main laser pulse is preceded by a pedestal due to amplified spontaneous emission (ASE) in the pre- and main amplifier providing a slowly rising edge of the temporal intensity profile of the beam. Usually, one or even more prepulses in the regenerative amplifier chain rise up which are marked by slight peaks on top of the rising edge of the main pulse. This occurs all on a time scale of ns to ps before the arrival of the main pulse. The intensity ratio of the prepulse to the main pulse is called the laser contrast (ratio) and tells about the quality of the laser beam shape. For intense laser beams the intensity of the pedestal and/or prepulse is already sufficient to generate a plasma on the target surface before the main pulse arrives. This preplasma is generated at intensities exceeding $I \approx 10^9\,\mathrm{W/cm^2}$.

The electromagnetic laser wave will eject electrons from the atoms of the target such that they can escape from their bound state to the continuum state. This overcoming of the atomic Coulomb potential is achieved by different ionization mechanisms depending on the laser intensity. Ionization by the *photoelectric effect*, where the photon energy has to be larger than the work function $W_A \approx (2-5)\,\mathrm{eV}$ needed to remove the electron immediately from its atomic binding, would require a photon wavelength in the UV regime but most lasers work in the red to infrared light regime. Like shown in Figure 2.3a), in case of *multiphoton ionization (MPI)*, a bound electron simultaneously absorbs $n$ photons with energy $\hbar\omega$ and is directly emitted from the atom with minimal kinetic energy. For the so-called *above-threshold ionization (ATI)* more photons get absorbed by the electron than it is necessary for its emission, so the electron escapes from the atom with a certain amount of kinetic energy.
In the interaction regime of intense short pulse lasers the ponderomotive potential of the laser field disturbs the Coulomb field of the atoms such that electrons can tunnel through the decreased Coulomb potential barrier. This tunneling process, as it is sketched in Figure 2.3b), occurs when the tunneling time of the electron is smaller than half of the oscillation period of the laser field. Thus, this ionization process is more effective for lower laser frequencies or longer laser wavelengths. The so-called *tunnel ionization* becomes important at intensities in the order of $I \approx 10^{12} - 10^{13}\,\mathrm{W/cm^2}$.
For even higher laser field strengths the *barrier suppression ionization* takes over which is depicted in Figure 2.3c). The Coulomb potential gets even more decreased by the laser field such that it lies beneath the ionization potential of the electron for a short period of time. As a consequence, the electron can escape from the atom without having to tunnel through a potential barrier. The modified Coulomb potential $V(r,t)$ with the perturbation $V'(r,t) = -eE_0(t)\,r$ of the laser field and the charge $Z$ of the produced ion reads

$$V(r,t) = -\frac{1}{4\pi\epsilon_0}\frac{Ze^2}{r} + eE_0(t)\,r \tag{2.22}$$

The laser intensity necessary for the occurence of this process can be calculated from the local maximum of the potential $V_{\max}$, given by setting $\partial V(r)/\partial r = 0$ and equating $V_{\max}$ with the

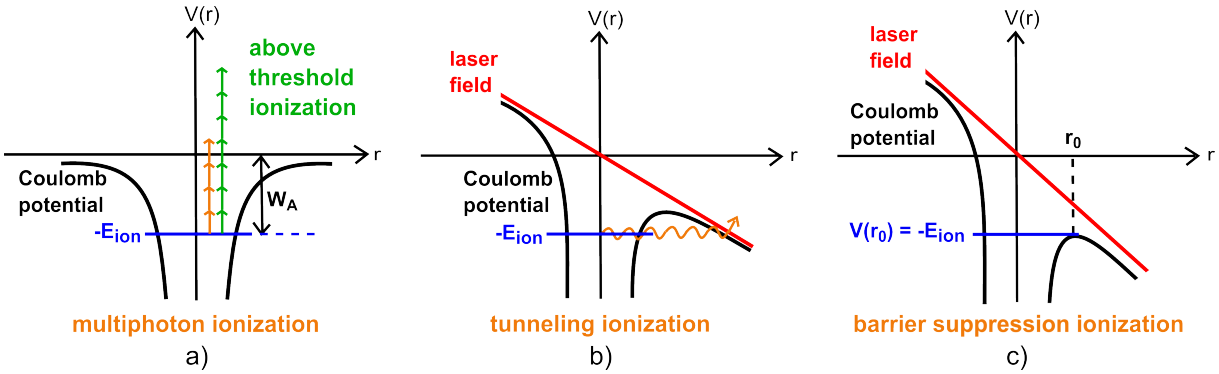


**Figure 2.3:** Laser-induced ionization mechanisms in plasma: a) Multiphoton (orange arrows) and above threshold ionization (green arrows) where an arrow symbolizes the energy of a single photon $E = \hbar\omega$. b) Tunneling ionization in the presence of a strong laser field which distorts the Coulomb potential, thereby making tunneling possible. c) Barrier suppression ionization in the presence of a very strong laser field distorting the Coulomb field such that electrons are immediately freed.

ionization potential $U_{\text{ion}}$ of the electron, i.e. $V_{\max}\left(r_{\max}, t\right) = -\sqrt{Ze^3E_0/(\pi\epsilon_0)} = -U_{\text{ion}}$. With $I = c\epsilon_0 E_0^2/2$, the intensity threshold for the barrier suppression ionization regime results in

$$I_{\text{thr}} = \frac{\pi^2 c\epsilon_0^3}{2e^6}\frac{U_{\text{ion}}^4}{Z^2} = 4\times 10^9 \frac{U_{\text{ion}}^4\,[\text{eV}]}{Z^2}\left[\text{W/cm}^2\right]. \tag{2.23}$$

In order to ionize gold atoms via this mechanism to a charge state of $Z = 1$ the laser intensity would have to exceed $I_{\text{thr}} = 2.8\times 10^{13}$ W/cm$^2$. After the first ionization processes are initiated by the laser interaction with matter the free electrons will ionize further atoms by collisional ionization for high density (solid) targets [51].

The properties of the generated preplasma, i.e. its scale length or its density, are mainly determined by the laser prepulses. While for some experiments the preplasma is needed, since it delivers free electrons and ions to be accelerated through the target. For other experiments, e.g. for studying the laser breakout afterburner (BOA) [58] mechanism (see section 2.5) where ultrathin targets are used, it is more important to keep the preplasma as small as possible. Depending on the special prepulse requirements the laser contrast ratio has to be adjusted.
Assuming a one-dimensional isothermal expansion [40] the generated preplasma expands from the target surface with an exponentially decaying density profile. Its expansion velocity is given by the ion speed of sound $c_s = \sqrt{k_B\left(ZT_e + T_i\right)/m_i}$ and depends on the electron and ion temperature $T_e$ and $T_i$, the degree of ionization $Z$ as well as on the ion mass $m_i$. The scale length $l = c_s t$ of the expanded preplasma is then defined as the position where the exponentially decaying density $n(z) = n_0(z)\exp\left(-z/(c_s t)\right)$ is decreased by a factor of $1/\exp(1)$ with respect to its density value at the beginning of the expansion, i.e.

$$l = \left|\frac{dn(z)/dz}{n(z)}\right|^{-1}. \tag{2.24}$$

Typical values for the plasma scale length are in the order of a few micrometers. The plasma ablation creates a high pressure on the laser irradiated target surface. This ablation pressure compresses and heats the surface material. Furthermore, it initiates a shock wave travelling into the solid target due to energy conservation. When the main pulse arrives it interacts with the already rarefied preplasma.

The electrons in the preplasma get disposed by the laser field versus the positive ions which can be regarded as a stationary positive ion background due to their much higher inertial mass. The established charge separation violates the quasineutrality of the plasma. An electric field builds up and the electrons are driven back by the resulting repulsive force $F = -eE$. The electrons begin to perform harmonic oscillations around their equilibrium position against the stationary ion background with the oscillation frequency

$$\omega_p = \sqrt{\frac{e^2 n_e}{\epsilon_0 \overline{\gamma} m_e}} \tag{2.25}$$

which is the so-called *(electron) plasma frequency*. It is obtained by solving the equation of motion of the electrons

$$\frac{d^2 z}{dt^2} = -\frac{eE}{\overline{\gamma} m_e} = -\frac{e^2 n_e}{\epsilon_0 \overline{\gamma} m_e} z = -\omega_p^2 z\,. \tag{2.26}$$

The plasma frequency only depends on the electron density in the plasma and on the electron mass. In the relativistic regime the latter increases, thus, the plasma frequency gets diminished which will have an important impact on the further laser propagation in the plasma as well as on the laser energy absorption. The electron oscillations involve the electrons as a whole which is expressed by its dependency on the electron density. Thus, they describe a collective behavior.

The propagation of the laser pulse in the plasma not only affects the electrons, but it experiences a back-coupling effect from the electrons, since it is itself strongly influenced by the oscillatory electron motion and, hence, by the electron plasma density. As long as the laser frequency $\omega_L$ is larger than the plasma frequency $\omega_p$, the electrons cannot keep up with the fast oscillating laser field and the laser pulse propagates further into the target. With increasing laser propagation length the plasma density continuously rises and with it also the plasma frequency increases according to equation (2.26). When $\omega_p$ approaches $\omega_L$, the electrons begin to follow the fast oscillations of the laser field and screen it by their charge. The absolute value of the laser wave vector $k = \sqrt{\omega_L^2 - \omega_p^2}/c$ vanishes. Due to the electron shielding the laser pulse can only propagate evanescently further with an exponentially decaying field amplitude and gets reflected. Its penetration depth is the so-called *skin depth* which is obtained by $l_s = c/\omega_p$. The critical density $n_c$ at which the laser light reflection sets in is characterized by $\omega_p = \omega_L$ and reads

$$n_c = \frac{\omega_L^2 \epsilon_0 \overline{\gamma} m_e}{e^2} = \frac{1.1 \times 10^{21}}{\lambda_L^2\,[\mu\mathrm{m}]}\,\mathrm{cm}^{-3} \tag{2.27}$$

according to equation (2.25). Assuming a laser wavelength of $\lambda_L = 800\,\mathrm{nm}$ and $\overline{\gamma} = 1$, the critical density has a value of $n_c = 1.75 \times 10^{21}\,\mathrm{cm}^{-3}$ which is roughly about two orders of magnitude below the solid state density of $n_{ss} \approx 10^{23}\,\mathrm{cm}^{-3}$. For longer laser wavelengths the critical density is smaller and the laser light is reflected earlier than it is the case for short laser wavelengths.

A helpful parameter for classifying the different density regimes of the plasma constitutes the refractive index of the plasma

$$\eta = \sqrt{1 - \frac{\omega_p^2}{\omega_L^2}} = \sqrt{1 - \frac{n_e}{n_c}}\,. \tag{2.28}$$

If $\eta$ becomes imaginary, which corresponds to $\omega_L < \omega_p$, the laser pulse cannot propagate further into the plasma and gets reflected. The plasma is therefore called *overdense*. In contrast, for a laser frequency of $\omega_L > \omega_p$, the refractive index becomes a real number. In this case, the laser propagation into the plasma proceeds and the plasma is called *underdense*. The critical density represents the plasma density at which this transition from underdense to overdense plasma occurs. It is equivalent to the transition from a real to an imaginary refractive index.

If the electron motion becomes relativistic, i.e. $\overline{\gamma} > 1$, the plasma frequency will decrease as a consequence of the growing mass inertia of the electrons while the critical density will increase according to equation (2.27). The laser pulse can propagate further into the plasma than in the nonrelativistic case. This phenomenon is known as *relativistic transparency* [59]. This effect becomes amplified by the ponderomotive effect due to which the electrons are expelled from regions of higher intensity. As a consequence, the electron density in the laser beam center drops and a plasma channel builds up in which the laser pulse can penetrate further. The contribution of the ponderomotive effect is therefore known as *self-channeling*. Both processes cause an increase of the local refractive index in the beam center and, hence, have a focusing effect on the laser pulse.
Moreover, the focusing of an intense laser beam into the plasma involves an additional variation of the refractive index in dependence of the radial laser intensity. In the central region of highest laser intensity the refractive index is higher than in the outer regions of the laser beam. In total, this spatial dependency of the refractive index acts as a focusing lens. The effect is therefore called *relativistic self-focusing*. This intensified focusing with an increased energy density in the beam center enforces the electron acceleration and thereby leads to increased ion energies.

## 2.3 Laser energy absorption by electrons

The energy transfer from the electromagnetic field of the laser pulse to the plasma is one of the most important aspects in the laser-ion acceleration since it influences both the maximum obtainable ion energy and the number of accelerated ions. Up to now, the highest laser intensities still do not suffice to accelerate plasma ions directly which would request intensities about $I \geq 5 \times 10^{24}\,\mathrm{W/cm^2}$. Therefore, the laser energy has to be mediated to the ions by the plasma electrons having a much lower inertia than ions. These accelerated plasma electrons can deliver their energy to the plasma ions by collisions, electrostatic field generation or other processes.

The laser energy absorption by electrons is determined by several parameters, beginning from the laser prepulse and the properties of its generated preplasma, serving as the source of free electrons, over the laser pulse parameters, e.g. intensity, pulse duration, pulse shape and incidence angle, to the target properties like thickness, surface roughness and conductivity. The electron motion in the laser-generated plasma is generally determined by the Lorentz force, equation (2.4). The Lorentz force must have an oscillating component in direction of the density gradient $\nabla n_e$, i.e. $\mathbf{E} \cdot \nabla n_e \neq 0$, in order to drive plasma oscillations, which finally lead to electron acceleration [60].
At laser intensities $I \leq 10^{16}\,\mathrm{W/cm^2}$ collisional processes dominate. An electron collides with an ion or with another electron in the underdense plasma and thereby gains energy by absorbing a photon in the presence of the laser field. Contrary to the case, where an electron loses energy by irradiating a photon –known as bremsstrahlung–, this mechanism is therefore called *inverse bremsstrahlung* since it physically describes the opposite process. But it is also known as *collisional absorption* in the literature due to its property of collisional electron heating. The electron-ion collision frequency scales as $\nu_{ei} \propto n_e Z / T_e^{3/2}$. It reduces as the effective electron

temperature rises which occurs for increasing laser intensities. Therefore, this mechanism plays only a negligible role at laser intensities exceeding $I \approx 10^{18}\,\mathrm{W/cm^2}$ at which the electron motion becomes relativistic. In this intensity regime collisionless processes govern the laser energy absorption by relativistic electrons, in the following named as hot or fast electrons, whose energy roughly corresponds to the ponderomotive energy $W_{\mathrm{pond}}$ given in equation (2.19).
One option of classifying the different absorption mechanisms is to divide them according to the plasma regime in which they arise. While laser energy absorption by the ponderomotive acceleration and the direct laser acceleration may occur in the underdense plasma, resonance absorption, Brunel heating, laser hole boring and $\mathbf{j} \times \mathbf{B}$ heating set in at the critical density surface, i.e. in the overdense plasma region.

### 2.3.1 Ponderomotive acceleration and laser hole boring

The ponderomotive acceleration usually becomes the dominating electron acceleration mechanism in the relativistic laser plasma interaction. The ponderomotive force, like it is described in section 2.1.1, acts along the negative gradient of the electric field und pushes electrons out of regions of higher intensity. The radial push of electrons out of the laser beam center occurs due to a radial intensity profile of a nearly Gaussian beam shape. Due to the rising edge of the laser pulse in its propagation direction the laser pulse has also a longitudinal intensity profile. The ponderomotive force can therefore act also in the longitudinal direction. When the main laser pulse is incident on the already extended preplasma, its major interaction with the plasma electrons occurs at the critical density surface. Here, the laser pulse can propagate further only evanescently into the overdense plasma and becomes reflected. Since the electric field gradient achieves its highest value here, the ponderomotive force is most effective at the critical surface and accelerates the electrons normal to the critical surface into the target. Thereby, the electrons gain a mean relativistic energy in the order of the ponderomotive potential

$$\overline{\Phi}_p = m_e c^2 \left(\overline{\gamma} - 1\right) = 0.511\,\mathrm{MeV} \left( \sqrt{1 + \frac{I\,\lambda_L^2}{1.37 \times 10^{18}\,\mathrm{W/cm^2\,\mu m^2}}} - 1 \right) \cong k_B T_e \qquad (2.29)$$

which can be assigned to an effective temperature $T_e$ of the electron population.
The depletion of electrons in the central region of the laser beam induced by both the ponderomotive effect and the relativistic self-focusing of the laser let the laser penetrate deeper into the plasma. The *laser hole boring effect* [61] occurs when the light pressure $p_L = I/c$ exceeds the electron plasma pressure $p_e$ and thereby pushes the critical surface further into the target. The preplasma cannot expand anymore in longitudinal direction and even becomes compressed. This leads to a steepening of the plasma density profile. The preplasma can only expand laterally back into the underdense plasma region which resembles boring a hole into the plasma.

### 2.3.2 Resonance absorption

For p-polarized laser light irradiating the target under an incidence angle $\theta$ with respect to the target normal the reflection of the laser pulse sets already in at a density $n_e = n_c \cos^2\theta < n_c$. The electric field component in direction of the target normal can tunnel further into the target up to the critical density where it can excite resonantly growing electron oscillations over some laser oscillations. When the electron oscillaton amplitude reaches a critical value the electrons

are driven into the plasma in form of a resonant electron plasma wave with $\omega_L = \omega_p$. This process is therefore called *resonance absorption*. Since for s-polarized laser light there is no electric field component in direction of the target normal no electron plasma wave can be generated with that polarization. The same argument is valid in case of normal incident laser light. The effectiveness of resonance absorption depends on the laser incidence angle $\theta$ as well as on the scale length $l$ of the preplasma. For a large value of $\theta > 80°$ the distance between the reflection surface and the critical surface will be too long for tunneling while for a small value of $\theta < 10°$ the electric field component parallel to the target normal will be very small and an electron plasma wave cannot be driven efficiently. In case of a steepened density profile, e.g. due to the ponderomotive force, the tunneling distance becomes smaller and the dependency on the incidence angle gets less important. In contrast to inverse bremsstrahlung, where almost all electrons absorb small amounts of the laser energy, only a small part of the electrons receives an energy transfer from the laser field in the resonance absorption process, but this energy transfer turns out to be larger.

### 2.3.3 Brunel heating

If the density gradient of the preplasma is very steep[2], similar to a step-like vacuum-plasma interface, the field amplitude of the resonantly driven electron plasma wave at the critical density will be in the same order as the incident electric field $E_0$ of the laser [51]. The electrons will oscillate with an amplitude of $z = eE_0/(m_e\omega_L^2) = v_{osc}/\omega_L$ in direction of the density gradient. If this amplitude is larger than the plasma scale length (equation (2.24)), i.e. $v_{osc}/\omega_L > l$, resonantly driven plasma waves cannot propagate any further but are extinguished after one laser oscillation cycle [62]. At relativistic intensities the ponderomotive force provides a steepening of the density profile by piling the electrons radially up. The resonance absorption goes over into the so-called *not-so-resonant absorption* introduced by Brunel [63] and therefore also known as *Brunel heating* or *vacuum heating* in the literature. In this electrostatic model the electrons can be pulled away from the plasma region into the vacuum by the p-component of the incident plus reflected electric field of the laser pulse. This happens in the first half oscillation cycle while the electrons flip and get accelerated into the plasma in the second half laser cycle with reversed field polarity. A pulsed electron acceleration into the target occurs resulting in one pulse of hot electrons per laser cycle. The electrons which have gained sufficient energy can cross the critical surface and propagate further into the overdense plasma region where the laser pulse cannot follow them due to its reflection at the skin depth (see section 2.2).

### 2.3.4 Direct laser acceleration

In the underdense plasma region relativistic self-focusing of the laser beam and the relativistic mass increase of the electrons lead to a much higher refraction index and to a higher intensity on the laser beam axis where a plasma channel builds up. The ponderomotive force drives a large amount of the electrons radially outwards which generate a radial electric field. The residual electrons produce an electron current in forward direction which induces an azimuthal magnetic field. These generated electric and magnetic fields act back on those electrons, which move forward with a small deviation from the laser beam axis, forcing them to oscillate with the so-called betatron frequency $\omega_\beta = \omega_p/\sqrt{2\gamma}$. If the betatron frequency matches the Doppler-shifted laser frequency and the phase of both the laser and the electron wave coincides the

[2] Such a steep density profile is achieved by a laser with a high contrast ratio.

electrons can be accelerated to high energies due to the established resonance condition [64]. A necessary demand for this *direct laser acceleration* is that the laser pulse length $\lambda_L = c\tau_L$ has to be larger than the plasma wavelength $\lambda_p = 2\pi c/\omega_p$ so that resonant coupling of the electron oscillation with the electric laser field can occur.

### 2.3.5 $\mathbf{j} \times \mathbf{B}$ heating

As soon as the laser intensity becomes relativistic, the magnetic component of the Lorentz equation (2.4) contributes to the laser energy absorption by electrons and is therefore known as $\boldsymbol{j \times B}$ *heating* [65]. The longitudinal $\mathbf{v} \times \mathbf{B}$ force drives nonlinear plasma oscillations with a similar electron dynamics like in case of Brunel heating, i.e. producing a strong electron heating. In case of Brunel heating the driving force of plasma oscillations is of electrostatic nature and is caused by the electric field component of a p-polarized obliquely incident laser pulse perpendicular to the target surface, while the driving force vanishes for s-polarized as well as for normal incident laser pulses. In contrast to Brunel heating, the $\mathbf{v} \times \mathbf{B}$ force does not underly these constraints. Since the magnetic force acts along the propagation direction of the laser pulse it is most efficient for normal incident laser light. Additionally, the main differences to the electrostatic driving field are that the excitation of plasma oscillations by the magnetic force requires a resonance frequency of $\omega_p = 2\omega_L$ instead of $\omega_L$, i.e. two relativistic electron bunches are generated in one single laser cycle. Furthermore, the magnetic force scales with $a_0^2$ instead of simply $a_0$. The quadratic scaling underlines the importance of the magnetic field in the ultrarelativistic regime, where $a_0 \gg 1$, and its insignificance in the non-relativistic regime, where $a_0 \ll 1$. A detailed analysis of the magnetic force effects using a non-relativistic perturbative approach is given in [49], illustrating that the oscillating term of the magnetic force is strongest in case of linear polarization and vanishes in case of circular polarization while the cycle average of the $\mathbf{v} \times \mathbf{B}$ force describes the ponderomotive force being independent of the polarization. The first experimental validation of $\mathbf{j} \times \mathbf{B}$ heating was published by Malka and Miquel [66] using an ultrahigh intensity laser pulse ($I > 10^{19}\,\mathrm{W/cm^2}$) of 400 fs pulse duration. By measuring the optical transition radiation (OTR), which is emitted by electrons from the target rear surface when crossing the plasma-vacuum interface [67], both frequency components, $2\omega_L$ and $\omega_L$, could be differentiated in dependence on the polarization and laser incidence angle [68].

## 2.4 Electron transport through dense matter

The above described mechanisms of laser energy absorption by electron acceleration in a plasma convey a qualitatively good theoretical picture of the first regime in the laser-plasma interaction. There are plenty of publications, which confirm the basic ideas of those mechanisms by both experimental results and numerical simulations. The latter demonstrate the sensitivity of the numerical results to certain parameters like the total electron density $n_0$, the laser entrance angle $\theta$ and the plasma scale length $l = n_c / \left|\partial_x n_e\right|_{n_e = n_c}$ as well as the strong dependence of the electron trajectories on the initial conditions [49, 57]. But it has to be considered that the simulation results are based on idealized assumptions of the underlying physics. For example, the real shape of the laser pulse of finite width is unknown and leads to a deformation of the plasma surface and, thus, to locally varying laser incidence angles with the consequence of a time-dependent absorption. Furthermore, the ion motion is usually neglected which results in local density modifications having an impact on the local electromagnetic fields.
From the experimental viewpoint, for the validation of the absorption mechanisms only indirect measurement techniques like bremsstrahlung radiation and optical transition radiation [69, 70]

or $K_\alpha$-imaging [71–73] exist up to now. Since the energy transfer from the laser field to the electrons cannot be analyzed on its own, i.e. detached from the electron dynamics in the plasma, for all these detection methods the electron transport dynamics through the plasma is involved, too. This is where the second regime in the laser-plasma interaction comes into play which also addresses the most complex and less understood part of all [74]. Here, one has to cope with collective effects like self-generated electric and magnetic fields and instabilities, but also with single particle effects like collisions and multiple small-angle scattering [75]. A thorough introduction to the electron transport is given in [76].

The whole process of hot electron generation and transport in the overdense plasma region is schematically represented in Figure 2.4 and is described in the following.
The laser impact on the target produces a large current density $j_{\text{fast}} = en_c c \approx 5$ TA/cm$^2$ (for $\lambda_L = 1\,\mu$m) of fast electrons which is transported through the plasma. Assuming that the current density flows in a cylindrical channel with a radius in the order of the laser spot size $r_0 \approx 10\,\mu$m, the corresponding current results in $I_{\text{fast}} = j_{\text{fast}}\pi r_0^2 \approx 1.6 \times 10^7$ A. This current generates an azimuthal magnetic field $B_\theta = \mu_0 I_{\text{fast}}/(2\pi r_0) \approx 3 \times 10^5$ T according to Ampère's law. The magnetic energy contained in the cylinder volume amounts to

$$E_{\text{mag}} = \frac{B^2}{2\mu_0}\pi r_0^2 d \approx 200\,\text{J}, \tag{2.30}$$

supposing a typical value of the target thickness $d = 10\,\mu$m. This value exceeds the absorbed laser energy in almost all cases which contradicts energy conservation. It implies that this huge current density has to be neutralized by a return current density $j_{\text{ret.}}$ such that

$$j_{\text{total}} = j_{\text{fast}} + j_{\text{ret.}} \approx 0 \tag{2.31}$$

locally [77]. The same request is obtained when regarding the space-charge electric field. If there was no return current, a surface charge density would be built up at the target surface from which the fast electron current leaves such that a uniform electrostatic space-charge field $E \approx 4\pi e n_c ct$ would establish. An electron would experience the work $W_{es} = eEx \approx 4\pi e^2 n_c (ct)^2 = m_e c^2 (\omega_L t)^2$ exerted on it, thus, relativistic electrons would be stopped within less than one laser oscillation cycle [49].
The response of the target material to the established space-charge electric field depends strongly on the material conductivity [76], as was shown in experiments investigating the fast electron transport in metal and plastic targets [78]. While in conducting materials the return current can rapidly be produced by cold background electrons, which permit the fast electrons to penetrate the overdense plasma, so-called *electric field inhibition* may occur in insulators. The electric response in insulators is much slower. Hence, the fast electron current cannot be compensated immediately by a return current. Since the material conductivity increases with the plasma temperature, electric field inhibition becomes unimportant for relativistic laser intensities, where the plasma temperature rises up to the order of keV. But in front of the fast electron current the plasma temperature is much lower such that electric field inhibition could occur there.
As a consequence of the required counterpropagating charge flow $j_{\text{ret.}}$, an anisotropy in the plasma temperature is produced and kinetic instabilities in form of electromagnetic two-stream instabilities, a special case of Weibel instabilities [79], evolve [80]. These lead to current filamentation in the underdense plasma regime [81–83] and, hence, to self-generated magnetic field filamentation [84]. These filaments permit to transport a much higher current than the Alfvén current[3] $I_A = \left(m_e c^3/e\right)\beta\gamma \approx 17.1\beta\gamma$ kA [86, 87]. Shielded by the return current surrounding the filaments, the latter get mutually attracted by the magnetic force [88] and finally

[3] The Alfvén current describes the transport limit set by the interaction of a current with its self-generated magnetic field [85] in vacuum.

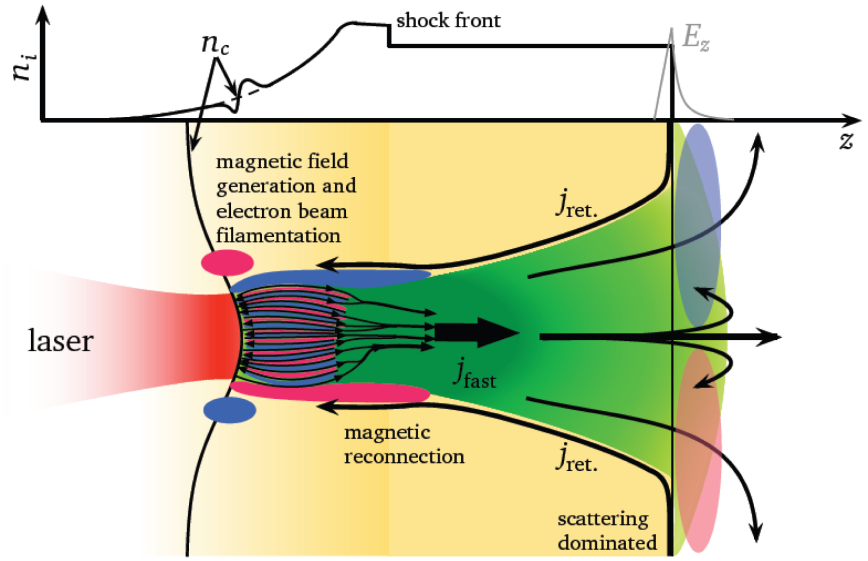


**Figure 2.4:** Schematic description of the hot electron transport in the laser-generated plasma. A laser pulse of high intensity deforms the already generated preplasma surface by its radiation pressure leading to a steepening of the density profile as shown in the one-dimensional diagram on top. A shock wave created by the ablation plasma travels into the target where it ionizes, heats and compresses the material. The generation of fast electrons leads to a high current $j_{fast}$ flowing to the target rear side and to a self-generated magnetic field (blue- and red-colored regions). This current is neutralized by a counterpropagating return current $j_{ret.}$ which causes streaming instabilities in form of fast electron beam and magnetic field filamentation. A global magnetic field arises due to mutual attraction and coalescence of magnetic field filaments which pinches the electron current on axis. In contrast, multiple scattering of fast electrons with background electrons and ions induces a beam broadening. The most energetic electrons escape from the target rear surface into vacuum establishing a strong electrostatic sheath field (gray line in the diagram on top). Lower energetic electrons get deflected by this field, reenter the target and can recirculate. This picture was taken from [84].

merge into a single global current channel [81, 89]. With this forward travelling global net current a global azimuthal magnetic field establishes. The magnetic field rises with increasing plasma density and begins to pinch the current such that the fast electrons propagate to the target rear side in a collimated beam channel on axis. On the contrary, the slow electrons get deflected by the magnetic field with backward travelling trajectories [90].
While a filamented structure of the electron current could be evidenced in insulating materials [91] as well as in layered targets [92, 93], conducting targets did not show any proof of a filamented electron transport, but demonstrated a uniform transport profile [94]. Therefore, metal targets are usually used for laser-ion acceleration experiments in which the electron transport through the target plays a major role.

While the fast electrons are propagating through the plasma they begin to lose energy due to the self-generated space-charge field and the cold background electrons get ohmically heated. As a consequence of the experienced multiple small-angle scattering [75], the electron distribution broadens during their propagation through the plasma, thus, counteracting the pinching effect of the magnetic field. The divergence angle of the hot electrons at the target rear side was indirectly measured in several experiments [69, 73, 94, 95] by different methods, e.g. imaging the $K_\alpha$ emission, bremsstrahlung or shadowgraphy of the plasma expansion on the rear surface. The obtained values lay between $\theta_e \approx 30°$ [95] and $\theta_e \approx 54°$ [73] refering to the full

divergence angle. Furthermore, it was observed that the electron beam divergence rises with increasing laser intensity [95].

The dependence of the hot electron production on a variety of parameters makes it difficult to compare the individual experiments with each other. Commonly, values like the conversion efficiency, i.e. the fraction of absorption, in hot electrons $\eta_e$ and the hot electron temperature $T_{e,\mathrm{hot}}$ evaluated by the ponderomotive energy (see equation (2.19)) are indicated in a phenomenological way. The hot electron distribution is commonly described by a Maxwell-Boltzmann distribution with a temperature $T_{e,\mathrm{hot}}$ according to

$$n_{e,\mathrm{hot}}(E) = n_0 \mathrm{e}^{-E/(k_B T_{e,\mathrm{hot}})} \tag{2.32}$$

since it fits best to the most used numerical model [61] and also to experimental data. A more detailed discussion on the hot electron distribution function is found in [96].
The conversion efficiency of laser energy into hot electrons is estimated by

$$\eta_e = \frac{N_{e,\mathrm{hot}} k_B T_{e,\mathrm{hot}}}{E_L} \tag{2.33}$$

where $E_L$ denotes the energy of the laser pulse and $N_{e,\mathrm{hot}}$ the total number of hot electrons. Experimental measurements delivered conversion efficiency values between 0.1 and 0.5 [60, 71, 97] with experimental hints of much higher values for ultrarelativistic laser intensities [98]. Assuming a mean conversion efficiency of $\eta_e = 0.3$, a hot electron temperature of $k_B T_{e,\mathrm{hot}} = 1\,\mathrm{MeV}$ and a laser energy of $E_L = 10\,\mathrm{J}$, a rough estimate of the total number of hot electrons yields $N_{e,\mathrm{hot}} \approx 2 \times 10^{13}$.

## 2.5 Laser-ion acceleration

As already discussed at the beginning of section 2.3, direct acceleration of ions would require laser pulses with intensities of $I \geq 5 \times 10^{24}\,\mathrm{W/cm^2}$. This is more than two orders of magnitude larger than the current record of about $10^{22}\,\mathrm{W/cm^2}$ obtained at the HERCULES laser in 2008 [99]. So far, the acceleration of ions is therefore driven by hot electrons which underlines their fundamental role as laser energy transmitters.
Measurements of proton acceleration made in 1999 observed collimated proton beams which had multi-MeV energies and were emitted from the target rear side of solid targets [8–10]. This observation caused a strong worldwide attention towards the field of laser-ion acceleration since the previous experiments recorded accelerated protons of only few MeV which were emitted from the target front side and had a broad angular distribution [100–102].
The generation and acceleration of protons from the target rear surface is based on a different mechanism compared to the observed acceleration from the target front surface since the hot electrons have gained more energy and have a higher directionality after having passed the overdense plasma. The most prominent and best investigated mechanism constitutes the *target normal sheath acceleration (TNSA)* mechanism. During the TNSA the most energetic electrons escape from the target rear surface into vacuum and establish an electric sheath field of such a strength that it is able to instantaneously field-ionize the atoms on the target rear surface and to accelerate these ions in target normal direction. The TNSA mechanism was introduced by Wilks *et al.* [31] in 2001 and was able to explain the experimental data on proton acceleration from the target rear surface [10, 12].
In the last decade there was a lot of research done regarding the laser-ion acceleration, especially the TNSA. Theoretical models of the TNSA were developed basing either on a static

or a dynamic description of the electric sheath. The ion dynamics is treated electrostatically and nonrelativistically within a fluid model [40, 41, 103] with electrons supposed to be in a Boltzmann equilibrium. The models do not consider the preceded laser-matter interaction but use the resulting electron temperature $T_{e,\mathrm{hot}}$ as well as density $n_{e,\mathrm{hot}}$ as initial conditions. The experimental improvements made on the TNSA concerned the increase of the maximum ion energy, but also the aim of obtaining monoenergetic ion beams with high directionality. These improvements led to the discovery of new laser-driven ion-acceleration mechanisms like the laser break out afterburner [58] and the radiation pressure acceleration [104].

### 2.5.1 Target Normal Sheath Acceleration

A schematic description of the temporal evolution of the TNSA is presented in Figure 2.5. In (a), the focused laser pulse interacts with the expanding preplasma which is created by the laser prepulse on the target front surface. As shown in (b), in the underdense plasma and at the critical density, where the laser pulse is reflected, hot plasma electrons are accelerated in forward direction. The hot electron transport through the target is maintained during the laser pulse by the established return current. When the hot electrons reach the target rear side the most energetic ones, having energies $k_B T_{e,\mathrm{hot}}$ in the range of a few MeV, can break out of it and can escape into the vacuum, as Figure 2.5(c) illustrates. There, the resulting charge separation induces an electrostatic potential $\Phi$ according to the Poisson equation and reads in an one-dimensional approach [49]

$$\frac{\partial^2 \Phi}{\partial z^2} = \frac{e\left(n_{e,\mathrm{hot}} - n_i\right)}{\epsilon_0} = \frac{e n_0}{\epsilon_0}\left(\mathrm{e}^{e\Phi/(k_B T_{e,\mathrm{hot}})} - \theta(-z)\right), \tag{2.34}$$

Herein, the electron density is given by equation (2.32), in which the kinetic energy is substituted by the potential energy $-e\Phi$. The ion density profile is supposed to have a step at the target rear surface at $z = 0$ and is described by $n_i = (n_0/Z)\,\theta(-z)$ with the charge state $Z$ of the ions, i.e. all the ions are inside the target marked by $z < 0$. Furthermore, the plasma is regarded as globally neutral, thus, the integral of equation (2.34) from $-\infty$ to $\infty$ is zero and the derivative of the potential $\partial_z \Phi$ has to vanish at $\pm\infty$. Deep in the target material the electron density should equal the background density $n_0$ while it vanishes in the vacuum far away from the surface, i.e. $\Phi(-\infty) = 0$ and $\Phi(\infty) = -\infty$. The Poisson equation can then be solved analytically in the vacuum region ($z > 0$) [106]. The field potential results in [49]

$$\Phi = -\frac{2k_B T_{e,\mathrm{hot}}}{e} \ln\left(\frac{z}{\sqrt{2}\lambda_D} + \exp(1)\right) \tag{2.35}$$

and the established electric field yields

$$E(z) = -\frac{\partial \Phi}{\partial z} = \frac{2k_B T_{e,\mathrm{hot}}}{e} \frac{1}{z + \sqrt{2}\exp(1)\lambda_D}. \tag{2.36}$$

In these equations the quantity $\lambda_D$ denotes the electron Debye length given by

$$\lambda_D = \sqrt{\frac{\epsilon_0 k_B T_{e,\mathrm{hot}}}{n_{e,0} e^2}} = 7.43\,\mu\mathrm{m}\sqrt{\frac{T_{e,\mathrm{hot}}[\mathrm{MeV}]}{n_{e,0}[10^{18}\mathrm{cm}^{-3}]}} \tag{2.37}$$

with the maximum electron density $n_{e,0}$ on the target rear side. The Debye length defines the characteristic length at which the electric charges begin to be screened. It gives a good

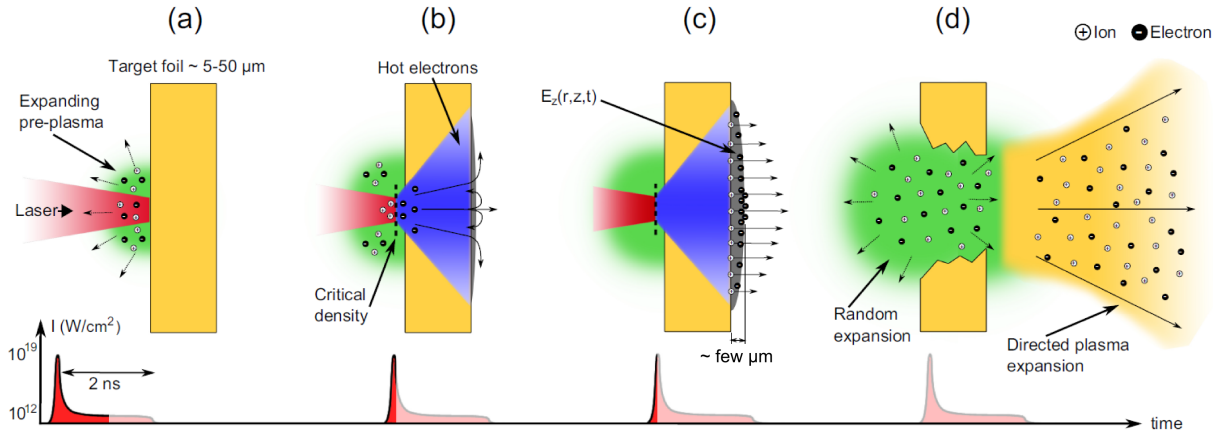


**Figure 2.5:** Schematic description of TNSA. a) The focused laser pulse interacts with the expanding preplasma on the target front surface. b) In the underdense plasma and at the critical density, where the laser pulse is reflected, hot plasma electrons are forward accelerated and a return current of cold background electrons builds up. c) The hot electrons escape from the target rear side with a broadened distribution and establish a dense electron sheath. Atoms on the target rear side get ionized by the strong electric field created by the charge separation. d) These ions are accelerated in direction of the target normal. A quasi-neutral plasma expansion with co-moving electron sets in while the target is destroyed. This picture was taken from [105].

estimate on the longitudinal extension of the electron sheath and usually is in the order of few micrometers. For example, assuming an electron density of $n_{e,0} = 10^{21}\,\mathrm{g/cm^3}$ near the critical density and an electron temperature of 1 MeV the Debye length yields 0.23 µm.
At the target-vacuum interface, i.e. $z = 0$, the electric field reaches its maximum value which is

$$E(z=0) = \frac{\sqrt{2}k_B T_{e,\mathrm{hot}}}{e\exp(1)\lambda_D} = 0.52\,\mathrm{TV/m}\,\frac{k_B T_{e,\mathrm{hot}}[\mathrm{MeV}]}{e\,\lambda_D[\mu\mathrm{m}]}\,. \tag{2.38}$$

The strength of this electric field is comparable to the strength of the laser electric field.
The electrons which become deflected by the electric field reenter the target moving towards the target front side. For laser pulses with pulse durations exceeding the time $\tau \approx 2d/c$, which the electrons need to propagate forth and back through a target of thickness $d$, the refluxing electrons can be accelerated again at the target front side. This phenomenon of repeated electron acceleration by the laser pulse is therefore called *recirculation* and could be confirmed by several experiments [69, 92] and also by simulations [90]. The pattern of electron recirculation enables to maintain the electrostatic sheath field for a time scale in the order of the laser pulse duration. In case of a laser wavelength of 800 nm one laser oscillation period results in $t_{osc} = \lambda_L/c = 2.67\,\mathrm{fs}$ and is considerably exceeded by the pulse duration of the laser. Therefore, the electric sheath field can be considered as quasi-static compared to other relevant time scales in this process. Due to the electron recirculation enhanced proton energies were gained, first demonstrated by MacKinnon *et al.* [107]. For long laser pulses, the electron recirculation may be limited by the shock wave which is induced by the ablation pressure on the target front side and travels into the target. When the shock wave front reaches the target rear surface the recirculation ceases and the target material is blown away.

Like depicted in Figure 2.5(c), besides the deflection of lower energetic electrons the generated electric field is strong enough to ionize the target atoms on the rear surface and to accelerate these ions. The governing ionization process constitutes the *field ionization by barrier suppression (FIBS)* [108, 109], described in section 2.2. The electric sheath field deforms

the Coulomb potential of the atoms on the target rear surface such that the Coulomb barrier is lowered beneath the ionization potential of the electron for a short period of time. The electron is immediately emitted into the continuum (see Figure 2.3c)). The threshold electric field $E_{\mathrm{thr}}$ necessary for this ionization process is obtained from equation (2.23) and yields

$$E_{\mathrm{thr}} = \frac{\pi \epsilon_0 U_{\mathrm{ion}}^2}{Ze^3} \,. \tag{2.39}$$

For the field-ionization of $C^{4+}$ having a binding energy of $U_{\mathrm{ion}} = 64.5\,\mathrm{eV}$ [110] an electric field of 0.18 TV/m is required [111]. This value is exceeded by the electric sheath field by at least one order of magnitude and a very fast field ionization of $C^{4+}$ occurs followed by its acceleration. The threshold value for $C^{6+}$ already results in 7 TV/m, thus, requiring a much stronger electric field.
Since the direction of the electric sheath field is along the target normal the ions are accelerated perpendicularly to the target surface. As Figure 2.5(d) illustrates, the ion acceleration occurs in a directed plasma expansion in forward direction.
Due to recirculation TNSA at the target front surface occurs as well, but the generated expanding preplasma blurs the density gradient, which therefore becomes smoother compared to the sharp density profile at the target rear surface. This results in a less pronounced accelerating field potential leading to smaller ion energies as well as a larger broadening of the emitted ions compared to the strong acceleration of ions from an initially cold target rear surface exhibiting an ultralow source size emittance [11]. However, the suppression of a preplasma expanding on the target front surface demonstrated that a rather symmetric proton acceleration from both target surfaces is obtained [112]. This emphasizes the importance of the arising density profile for the TNSA.

The protons accelerated in the TNSA process stem from target impurities being partly present in the target bulk material but predominantly from a contamination layer on the target surface consisting of hydrocarbons and water vapour. Unless the target is specially treated, this contamination layer is always present due to the target's exposure to air prior to the experiment. Rear surface atoms with the lowest ionization potential are preferably ionized and the ions with the highest charge-to-mass ratio q/m are favorably accelerated by the electrostatic sheath field. Protons from the topmost target surface layer are exposed to the highest electric field gradients –therefore they constitute the predominant accelerated ion species– and screen the electric field for protons and ions coming from the successive layers. These in return experience a decreased electric field gradient and, consequently, get less accelerated. The acceleration of particles from different target depths results in a broad energy distribution which becomes broader with increasing contamination layer thickness [1]. With the help of different techniques of target surface cleaning the contamination layer becomes reduced. This has a strong impact on the subsequent ion acceleration as it was investigated in the frame of this thesis. An additional energy broadening may result from the inhomogeneous electron distribution in the sheath which produces an inhomogeneous accelerating field in the transverse direction.

The broad TNSA ion energy spectrum represents one of the two main disadvantages of this laser-ion acceleration process since for most of its applications, e.g. the injection into particle accelerators [11, 14, 15] or proton therapy [27, 30, 113], an ion beam with a distinct energy and a collimated beam profile is needed. The second main disadvantage represents the still relatively large divergence angle of the emitted ions with a half opening angle of up to 30° [114] resulting from the spatially inhomogeneous electron sheath. The initial ion source size radius

can be approximated by the electron broadening angle $\theta_e$ during their propagation through the target of thickness $d$ and results in

$$r_{\text{source}} = r_0 + d \tan\left(\frac{\theta_e}{2}\right). \tag{2.40}$$

It is relatively small, e.g. for a laser focal spot radius of $r_0 = 10\,\mu\text{m}$, $\theta_e = 40°$ and a target thickness of $d = 10\,\mu\text{m}$ the ion source size radius yields $13.6\,\mu\text{m}$ corresponding to a source size of $\pi r_{\text{source}}^2 = 585\,\mu\text{m}^2$. But once the ions detach from the target rear surface they expand in a plasma cloud. Furthermore, the electron sheath also expands laterally as the electrons recirculate several times within the target. This contributes to the effect of ion beam broadening. Nevertheless, laser-accelerated ions provide high quality beam properties like a high particle intensity [10, 12], a short pulse length and a very low transverse source emittance [11]. These characteristics exceed the parameters of standard particle accelerators and that is why laser-accelerated ion beams have gained a large interest in scientific research since their discovery.

### Theoretical approach to TNSA

A complete theoretical description of the TNSA is highly complicated since it involves not only the multi-dimensional electron expansion into vacuum, and correlated to that the induced electric field distribution, but also the atomic composition on the target rear surface, ionization processes and the ion acceleration. The following diagram illustrates the interplay of these three parts with each other:

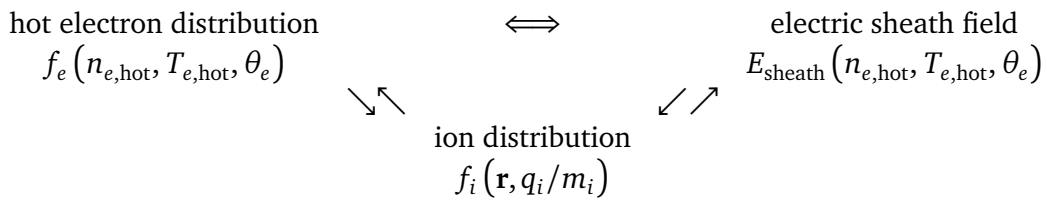


Almost all TNSA models do not include the laser absorption regime and the complex electron transport dynamics through the target but initiate with a given distribution function $f_e$ of hot electrons. The hot electrons leaving the target rear side generate an electric field with its peak value on the target rear side. The electric field itself depends on the hot electron density distribution $n_{e,\text{hot}}$ and temperature $T_{e,\text{hot}}$ and both acts on the lower energetic electrons by deflecting them backwards into the target and on the atoms located at the target rear surface. These atoms become ionized in dependence on their ionization potential and accelerated according to their spatial position $\mathbf{r}$ and their charge-to-mass ratio $q_i/m_i$. The electric field reduces as the electrons lose energy to the ions via the Coulomb force. These electrons are supposed to accompany the accelerated ions and are therefore called co-moving electrons. Thus, the particle acceleration can be regarded as a quasi-neutral plasma expansion.

### Analytical models

The current analytical TNSA models all have the common aim of giving a reliable prediction on which parameters influence the ion acceleration, especially regarding the maximum ion energy and their energy distribution, and how the scaling with these parameters looks like. The analytical models can be categorized into mainly two different approaches. The first one bases on a quasistatic approach [115]. It is valid only for a very short time scale on which collective

ion reactions to the generated electron sheath cannot occur. Only the most energetic ions are accelerated by the electron sheath before the latter expands. Therefore, the quasistatic model is well suited for an estimation of the maximum ion energies.
The second type of model bases on a fluid approach [40, 41] and considers longer time scales on which the ions follow the expansion of the electron sheath. The isothermal plasma expansion model by Mora [40] was one of the earliest TNSA models finding its justification in the continuous supply with hot electrons during the laser pulse. It is widely used since it provides a good estimate of both the ion energy spectrum and the maximum ion energy. The prediction of the exponential ion energy spectrum

$$\frac{dN_i}{dE_i} = \frac{n_{i,0} c_s t_{\mathrm{acc}}}{\sqrt{2Zk_B T_e E_i}} \mathrm{e}^{-\sqrt{2E_i/(Zk_B T_e)}} \tag{2.41}$$

with the ion speed of sound $c_s = \sqrt{Zk_B T_e/m_i}$, the ion acceleration time $t_{\mathrm{acc}}$ and the assumption of quasineutrality $n_{e,0} = Zn_{i,0}$ could be reproduced relatively well by experimental results and numerical simulations [38]. The ion acceleration time $t_{\mathrm{acc}}$ can roughly be approximated by the laser pulse duration $\tau_L$ or, according to [38], by $t_{\mathrm{acc}} \approx 1.3 \times \tau_L$. The maximum energy an ion can gain during the isothermal plasma expansion results in

$$E_{i,\max} \approx 2Zk_B T_e \ln\left(\tau + \sqrt{\tau^2 + 1}\right) \tag{2.42}$$

with the dimensionless time variable $\tau = \omega_{p,i} t_{\mathrm{acc}}/\sqrt{2\exp(1)}$, where $\omega_{p,i} = \sqrt{n_{e,0} Ze^2/(\epsilon_0 m_i)}$ denotes the ion plasma frequency. In the original work of Mora the acceleration time $t_{\mathrm{acc}}$ in the equations above was substituted by the continuous time $t$. However, in this case the maximum ion energy would continuously increase. This unphysical behavior was avoided by inserting a phenomenological cutoff [60] in form of the finite maximum time for the ion acceleration $t_{\mathrm{acc}}$, which was determined experimentally by Fuchs *et al.* [38] with the relation written above. In a revised version the plasma expansion was treated adiabatically [41] considering the electron cooling due to their energy loss by plasma expansion, collisions and radiative losses.

### Numerical simulations

While the analytical TNSA models are a good estimate for one-dimensional quantities, they cannot provide information about the much more complicated multi-dimensional quantities like the time-dependent spatial or velocity distribution function of the ions. A more extensive picture of the time-dependent ion acceleration including its transversal expansion can be addressed by numerical simulations like particle-in-cell (PIC) simulations [116]. PIC simulations are widely applied in laser-plasma interactions because they permit a kinetic description of the plasma particles in a three-dimensional (3D) coordinate space. In this computational method particles are allocated on fixed points in a grid according to their initial distribution function. Each computational particle represents a group of particles and can be visualised as a small piece of phase space, i.e. a particle in a cell, which explains the name of this simulation procedure. After the computation of the particle's charge density the Maxwell equations are solved and the electromagnetic fields are obtained on discretized grid positions. The influence of the fields on the particles by the Lorentz force is calculated leading to a modified particle distribution and charge density on the grid. This procedure enables a 3D particle tracking in relativistic laser-plasma interactions with a time resolution in the order of $\Delta t \leq \omega_p^{-1} = 0.177/\sqrt{n_e[10^{22}\mathrm{cm}^{-3}]}\,\mathrm{fs}$ [105] such that plasma oscillations can be resolved and with a corresponding grid size of about $c/\omega_p$ or even smaller than the local Debye length $\lambda_D = \sqrt{\epsilon_0 k_B T_e/(n_e e^2)}$ when self-generated fields

should be resolved. These requests of temporal and spatial resolution as well as the incorporation of a high number of simulated particles, which is needed to resolve large density gradients in the plasma expansion, lead to very long computation times. In order to reduce the latter, one has to cope with some limitations like switching to a 2D simulation, using smaller simulation boxes or implementing macro-particles which carry a higher mass and charge, i.e. being composed of a higher number of single particles.

### 2.5.2 Other ion acceleration mechanisms

The optimization of certain laser parameters like the increase in intensity of the laser pulse or the laser contrast improvement by few orders of magnitude and the further development of the target design led to the discovery of new possible acceleration mechanisms. In 2007 first hints of a new acceleration mechanism were found in PIC simulations which emerged when a laser pulse of $I \approx 10^{21}\,\mathrm{W/cm^2}$ interacted with an ultrathin target foil comparable to the skin depth, i.e. a few nm [58]. After an initial TNSA phase the target electrons become heated so strongly that the skin depth becomes comparable to the target thickness. The laser can penetrate the target plasma and therefore, this mechanism was named *laser breakout afterburner (BOA)* [58, 117]. When the laser pulse penetrates the target rear side its ponderomotive force generates an intense relativistic electron beam propagating in forward direction. This electron beam is supposed to experience un instability, the so-called relativistic Buneman instability [118, 119], which arises due to the relative particle drift of electrons and ions. Energy transfer from the electrons to the ions occurs leading to assumed ion energies in the GeV-regime. Recent experiments performed at the TRIDENT laser facility at the Los Alamos National Laboratory (LANL) could provide enhanced proton and carbon ion energies [120] compared to the ion energies obtained via TNSA when testing the BOA regime. According to simulations this is related to the enhanced and volumetric heating of electrons.
Another new acceleration mechanism for circularly polarized laser pulses producing highly monoenergetic proton beams of up to GeV-energies and with a very small divergence angle ($< 4°$) was numerically discovered in 2007 [104, 121, 122]. In this so-called *radiation pressure acceleration (RPA)* regime a thin foil is accelerated as a whole by the radiation pressure of a laser pulse with $I \approx 10^{20}\,\mathrm{W/cm^2}$. For thick targets the RPA is more commonly known as hole boring (see section 2.3.1) since the light pressure of the laser pulse deforms the plasma surface parabolically, thereby steepening the density profile. For thin targets, a complete hole boring sets in and the laser pulse can directly accelerate ions to high energies because the ions are not screened by the background plasma anymore [60]. This regime is also known as the *light sail regime* [123] due to the visualisation of a very thin object having an extended surface and low mass. First experimental results [124] could confirm the supposed enhanced ion energies. More detailed information about BOA and RPA, their differences to TNSA and the involved technical challenges for their realization can be found in [117].

There were several new approaches made towards the improvement of laser-accelerated ion beams. From the laser side a lot of improvement was achieved in the field of ASE contrast enhancement where values about $10^{-10}$ and better are obtained, e.g. by direct amplification of the oscillator pulses in an ultrashort optical parametric amplifier (uOPA) [125]. A high temporal contrast is mandatory for laser-ion acceleration experiments using ultrathin target foils, as in case of BOA [126] and RPA [127], in which the prepulse or pedestal of the laser can already destroy the target. A rise in laser intensity was mostly achieved by reducing the pulse duration to values in the order of few ten fs and by improving the focusing optics since an increase in laser energy is usually more difficult to achieve and also more expensive. However, it has to be

considered that for an ultrashort pulse duration the ion acceleration time is also very short. From the viewpoint of target fabrication a lot of research was done concerning a sophisticated target geometry, e.g. specialized hemispherical and cone targets. These have the ability to guide the generated particles in a collimated beam in forward direction, thus, acting as a focusing device [128]. The recent development tends to use thinner and mass-reduced targets for permitting the laser pulse to penetrate the target. The coupling of the electromagnetic laser field to electrons and ions in a confined space leads to volumetric heating and energy confinement which are able to accelerate the particles more efficiently, like it is the case for BOA and RPA [58, 104]. For example, the energy loss of electrons as a consequence of multiple small-angle scattering while propagating through the dense plasma is almost completely prevented because the electron transport regime, as described in section 2.4, is omitted for thin targets. They become subject of relativistic transparency.

The modification of the detailed properties of both the laser pulse and the irradiated target enabled to enter a new regime of laser-ion acceleration beyond the TNSA as this section illustrated. Besides the properties of the laser pulse, this underlines the importance of the target characteristics for laser-ion acceleration experiments. Irrespective of the particular ion acceleration mechanism the target –either its rear side in case of the TNSA or the complete target in case of BOA and RPA– represents the ion source and determines the accelerated ion species as well as their energy spectra decisively. Thus, a thorough target characterization contributes to a more profound understanding of the laser-ion acceleration process.

# 3 Target surface characterization

The knowledge of the structure of the target rear surface is of central concern for studies regarding the laser-ion acceleration by the TNSA since the target rear surface acts as the ion source. On the one hand, its atomic composition determines the elements, which can be ionized and accelerated, and their fraction gives an indication of how many ions of a certain ion species could in principal be accelerated. On the other hand, the measured ion spectra give important information about the strength of the electric field potential. The accelerating electric field pointing perpendicular to the target surface is experienced strongest for atoms located at the topmost positions of the target rear surface. Due to particle screening it is experienced weaker and weaker for atoms located at deeper positions. Furthermore, the ionization potential increases both with the atomic masses of the single elements and with the respective charge states. More energy is needed in order to additionally remove the electrons from inner atomic shells than only those from outer ones since the electrons on inner shells experience a higher bonding force to the nucleus. The accelerating force exerted on the produced ions is proportional to their charge-to-mass ratio q/m. Light atoms are preferentially ionized and ions with the highest charge-to-mass ratios become favorably accelerated.
Adsorption of residual atmospheric gases on the target surface leads to the formation of a contamination layer. Due to its topmost position on the target surface this contamination layer is therefore exposed to the highest electric field gradients. The contaminants shield the electric field for atoms from the target material, which consequently get less ionized and accelerated. The experiments conducted in the framework of this thesis concentrated on the stepwise removal of these contaminants by the irradiation with fs-laser pulses inducing desorption.

In this chapter the examination of the target surface structure plays the central role. The target surface composition, summed over a depth of about 1 µm, was measured by using the elastic recoil detection analysis (ERDA) technique. The obtained results are presented in the following.

## 3.1 Elastic recoil detection analysis

The composition of the target surface contamination was investigated for copper and aluminum by performing an elastic recoil detection analysis (ERDA) [129, 130] carried out at GSI Helmholtzzentrum für Schwerionenforschung GmbH and at the Maier-Leibniz-Laboratorium of the Ludwig-Maximilians-Universität as well as the Technical University in Munich. The elastic recoil detection analysis represents a well-established method for depth profile measurements of the target materials. ERDA with heavy ions is particularly sensitive to the light ion content of the target surface and is suited well for examining the contribution of target surface contaminations like hydrocarbons or oxides.

During an ERDA measurement the target is hit by a heavy ion beam, in the present case $^{136}$Xe with 1.4 MeV/u, under a flat angle $\delta$ with respect to the target surface like shown in Fig. 3.1a). After having lost a certain amount of energy along their path $d/\sin\delta$ through the probe material these projectiles collide elastically with the target atoms and eject them in forward direction, i.e. out of the target surface. The kinetic energy $E_r$ of the scattered target

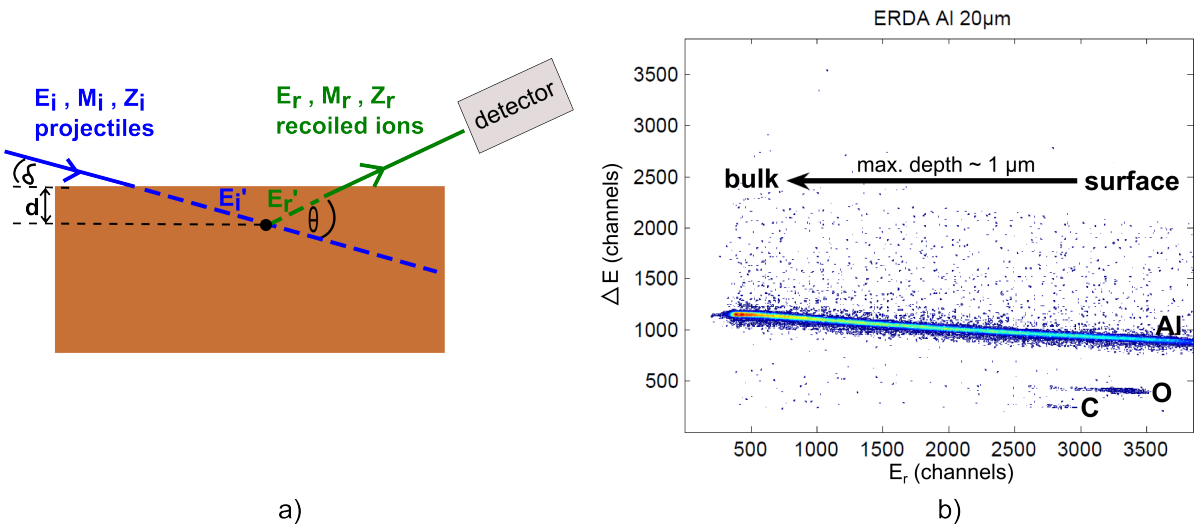


**Figure 3.1:** a) ERDA principle: An ion beam of energy $E_i$, mass $M_i$ and proton number $Z_i$ (blue) penetrates the target, thereby losing the energy $\Delta E_i = E_i - E_i'$, and collides with target atoms of mass $M_r$ and proton number $Z_r$. These are ejected under the scattering angle $\theta$, arriving the detector with a residual energy of $E_r = E_r' - \Delta E_r$ (green). b) ERDA measurement of a 20 µm thick aluminum foil (raw data).

atoms of mass $M_r$ and with the scattering angle $\theta$ is obtained via the elastic scattering theory of classical mechanics using momentum and energy conservation and reads

$$\frac{E_r}{M_r} = \frac{4\cos^2\theta}{\left(1 + M_r/M_i\right)^2}\frac{E_i}{M_i} \approx 4\cos^2\theta\,\frac{E_i}{M_i}\,. \tag{3.1}$$

In this equation, written in units of MeV/nucleon, the quantities $M_i$ and $E_i$ denote the mass and energy of the projectiles and it is assumed that the ejected particles are much lighter than the projectiles, i.e. $M_r/M_i \ll 1$. The recoiled ions then have all nearly the same velocity and, thus, they also have a similar energy loss [131] on their way through the target material since the energy loss depends on the particle velocity.
The differential cross section of an assumed Rutherford scattering process with the proton numbers $Z_i$, $Z_r$ of the projectiles and recoiled ions, respectively, is given by

$$\frac{d\sigma}{d\Omega}\left(E_i,\theta\right) = \left[\frac{Z_i Z_r e^2\left(M_i + M_r\right)}{2M_r E_i}\right]^2 \frac{1}{\cos^3\theta} \approx \frac{Z_i^4 e^4}{4E_i^2}\frac{1}{\cos^3\theta}\,, \tag{3.2}$$

where for the second expression $M_r/M_i \ll 1$ and the approximation $M = 2Z$ was used. In this case, the cross section and, hence, the detection efficiency is not element specific anymore but becomes the same for all recoiled ions [130]. Its very strong dependency on the proton number of the projectiles being proportional to $Z_i^4$ demonstrates the advantage of using heavy ions as projectiles because of the increased counting rate even at low beam currents.

The ejected surface particles are analyzed by a magnetic spectrometer in case of H atoms and an ionization chamber in case of heavier atoms, both combined with a charge coupled device (CCD) detector. This $\Delta E - E$ detector system determines both the energy loss and the remaining energy of the recoiled ions contemporaneously. The measured energy loss $\Delta E$ in the ionization chamber gives information about the proton number $Z_r$ of the recoiled particle while the residual energy, which is recorded in the CCD detector, provides a depth information

| Sample | Atom | $\rho_{ERDA}$ [atoms/cm$^2$] |
|---|---|---|
| Cu | H | $1.91\times10^{16}$ |
| | C | $1.37\times10^{16}$ |
| | O | $1.61\times10^{16}$ |
| Al | H | $1.46\times10^{16}$ |
| | C | $6.94\times10^{15}$ |
| | O | $3.03\times10^{16}$ |

**Table 3.1:** Particle concentration $\rho_{ERDA}$ on the surface of aluminum and copper target foils of 20 µm thickness summed over a measurement depth of $\leq 1$ µm. The ERDA measurements were performed by a high resolution magnetic spectrometer for the analyzation of hydrogen and by an ionization chamber for the analyzation of heavier atoms [1, 132].

of the particle in the target. Figure 3.1b) demonstrates a typical ERDA measurement of a 20 µm thick aluminum foil. Higher residual energies, given here in units of energy channels, belong to particles located near the target surface. This mainly regards the contaminants as carbon and oxygen. The projectiles experience only a minor energy loss since they have to penetrate only a short distance through the target material until the elastic collision with these atoms. Their momentum transfer to the target surface atoms is therefore higher than the momentum transfer to particles located deeper in the target, like the aluminum atoms in this case. Thus, the aluminum atoms get detected with lower residual energies than the target surface atoms. Since a flat irradiation angle $\delta$ enlarges the propagation length of the projectiles into the target it provides a higher depth resolution of the ejected particles.

The ERDA measurements deliver information not only about the composition of the target contaminations but also about the particle concentration on the target surface which is summed over the measurement depth of $\leq 1$ µm. For the analyzed aluminum and copper target the obtained results are shown in Table 3.1 [1]. Very similar results within the same order of magnitude were obtained from the analysis of Pd, Zr, and W target foils [133]. The composition of the aluminum surface shows the predominance of oxygen which stems from the native oxide layer and is more pronounced for aluminum than for copper. The measured carbon fraction of the aluminum surface is only half of the value measured for the copper surface while the hydrogen content is relatively similar for both of the investigated target materials. In general, target surface studies show that the contribution of carbon and hydrogen atoms prevails for noble metals like gold whereas the other metals mainly show a considerable amount of oxygen stemming from their oxide layer.

# 4 Femtosecond-laser desorption

Although high intensity laser experiments take place in interaction chambers with common vacuum conditions at a pressure in the order of $10^{-6}$ mbar, there is still some reduced flow of residual gas present which interact with the chamber walls and all other surfaces inside the interaction chamber. Since the targets used for laser-particle acceleration are usually produced under normal air conditions, gas atoms in the atmosphere will interact with the target surfaces, get deposited on the surface and can also diffuse into the bulk material. This is also the reason why typical TNSA-experiments, in which metals are used as target material, mainly observe a large quantity of accelerated protons and carbon ions instead of ions stemming from the material itself.

The most prominent approaches of getting rid of the adsorbed contaminants on the target surface are ohmic heating and ns-laser ablation. In case of ohmic heating –also known as resistive heating– a current is applied at the target surface. The target material is heated due to moving electrons which collide with ions and thereby transfer energy into kinetic energy of the ions. The amount of generated heat $Q$ has a quadratic dependence on the applied current and is proportional to the electric resistance, i.e. $Q \propto I^2R$. This target heating leads to a substantial rise of the desorption yield and also of diffusion since both the desorption and the diffusion rate increase with temperature.
The removal of surface contaminations by ns-laser ablation occurs also via heat transfer, but as a consequence of irradiating the target surface with laser pulses of nanosecond pulse durations. The laser energy is absorbed by the electrons and instantaneously transferred to the lattice via electron-phonon coupling. The target heating can be described by a heat conduction equation. Since the heat conduction proceeds slowly, only the target surface becomes strongly heated inducing a significant change of the thermophysical properties of the material [46]. Evaporization of the target surface begins and for sufficiently high laser fluences above the so-called *ablation threshold* an ablation plasma is generated [134]. This thermal ablation usually is the dominating mechanism for nanosecond laser irradiation on solids. However, due to the interaction of the long laser pulse with the ablated plasma particles less laser energy is available for the ablation process, hence, the efficiency of laser ablation drops. Furthermore, hot plasma particles can begin to sputter and thereby damage the target.
Both methods of surface particle removal involve heating of the target surface which is always accompanied by thermal stresses, melting and clearly visible structural modifications of the target surface. Molten material remains on the surface, mostly visible in form of molten craters [135], and roughens it.

In this thesis an alternative approach to successively clean the target surface from its contamination was applied. The desorption induced by femtosecond laser pulses allows to remove adsorbed surface particles with causing considerably less damage to the target surface since the interaction of the laser pulse with the target material happens on a time scale, on which thermal effects like electron-phonon coupling do not play a role.

This chapter begins with a general overview of sorption processes on surfaces with a closer look on the kinetics of adsorption and thermal desorption. It continues with the desorption induced by fs-laser pulses following a nonthermal interaction characteristics. Firstly, a phe-

nomenological approach to the fs-laser desorption is given considering the single microscopic processes on their specific time scale. Secondly, a numerical approach combining the benefits of the two-temperature model with those of the molecular dynamics method is introduced which allows to describe the energy transfer from the laser pulse to the desorbed particles theoretically. Numerical simulations within this model enabled to estimate the threshold fluence of the desorption laser, at which a plasma is generated on the target surface of gold, copper and aluminum targets. Subsequently, the experimental setup of laser-induced desorption measurements using the PHELIX laser at GSI Helmholtzzentrum für Schwerionenforschung GmbH as well as the applied laser parameters are discussed, followed by considerations of the readsorption of gas molecules in the meantime of two consecutive laser pulses. The experimental results of the desorption measurements are divided into two parts. The first part refers to total pressure measurements during the laser-induced desorption. These enabled on the one hand to determine the regimes of desorption and plasma formation for the studied materials and on the other hand to estimate the number of adsorbed gas particles contained in the contamination layer. The second part bases on partial pressure measurements of the desorbed gases providing information about the composition of the contamination layer. The chapter concludes with a discussion of the obtained experimental results on fs-laser desorption.

## 4.1 Mechanisms of fs-laser desorption

### 4.1.1 Sorption processes

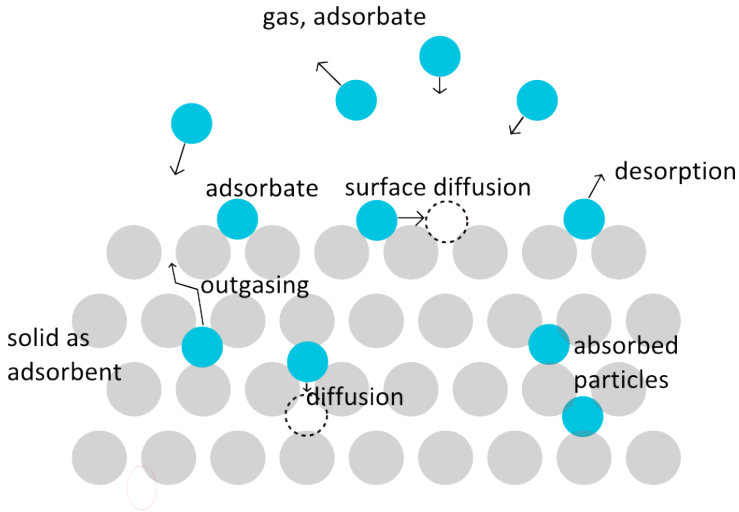


**Figure 4.1:** Overview of sorption processes. The gray circles represent the atoms of the solid. Gas atoms and molecules (blue circles) hit the surface and get adsorbed, diffuse into the solid (get absorbed) or desorb from the surface. Modification of [136].

Several different processes can occur when gas atoms or molecules are interacting with the surface of a solid [136]. This is shown in Fig. 4.1. The surface of a solid acts as a possible *adsorbent* for the gas particles which attach to the surface with a sticking probability of $s = \exp(-E_{\mathrm{act}}/(k_B T)) \leq 1$ or get reflected with the probability $1 - s$. This sticking probability depends both on the temperature $T$ of the gas particles and on the activation energy $E_{\mathrm{act}}$ needed to be exceeded. One distinguishes between two different adsorption mechanisms: The gas particles sticking to the surface, the so-called *adsorbates*, can either experience *dipole forces* or *Van-der-Waals forces*, which is named *physisorption*, or they can be attached to the surface

by *electron exchange forces* known as *chemisorption*. In case of the physisorption, the resulting binding energy or adsorption energy $E_{\mathrm{ad}}$ is already sufficient to get a molecule or gas atom at a distance of about $(0.3 \pm 0.1)\,\mathrm{nm}$ attached to the surface. For the chemisorption a much larger activation energy $E_{\mathrm{act}}$ is necessary in order to dissociate a molecule in atoms occurring at a distance of about $0.15\,\mathrm{nm}$ to the surface. The kinetic energy component of the gas particle normal to the surface therefore has to be larger than $E_{\mathrm{act}}$ in order to overcome the potential barrier for the chemisorption.

Once adsorbed particles can also be removed from the surface which is referred to the concept of *desorption*. The requested desorption energy $E_{\mathrm{des}}$ equals the adsorption energy $E_{\mathrm{ad}}$. For physisorption it is below $0.4\,\mathrm{eV}$ while it is much stronger for chemisorption achieving values between $0.8\,\mathrm{eV}$ and $8\,\mathrm{eV}$. Even higher binding energies can be reached when adsorbates undergo chemical bonds with the surface atoms. The adsorbates can also diffuse into the bulk material which is called *absorption* as the particle is absorbed in the lattice structure of the material.
The removal of absorbed particles from the bulk, known as *outgasing*, takes place on much larger time scales and has to be regarded separately from the desorption process, which describes a surface effect.

### Adsorption kinetics

The maximum surface coverage with one monolayer of adsorbates is obtained when the adsorbates are ordered such that the smallest rectangular cell has an area of $A = 2\sqrt{3}r^2$ with the particle's radius $r$, as it is illustrated in Figure 4.2. Assuming $r = 1.6 \times 10^{-10}\,\mathrm{m}$ for the typical radius of a nitrogen molecule [136], the areal density of a monolayer of adsorbates becomes

$$\rho_{\mathrm{mono}} \equiv \frac{N}{A} = \frac{1}{2\sqrt{3}\left(1.6 \times 10^{-10}\,\mathrm{m}\right)^2} \approx 10^{15}\,\mathrm{cm}^{-2}\,. \tag{4.1}$$

This number serves as a good reference number for the areal density of one monolayer. But it has to be taken into account, that real surfaces with a certain surface roughness have some ripples providing that the coverage area will be larger. The ratio between the real surface coverage and the maximum surface coverage is expressed by the parameter $\theta = \rho/\rho_{mono}$. While the adsorption forces for the consecutive adsorption monolayers decrease or even vanish, the molecular forces between the adsorbates increase and become the main source of the further adsorption of gas particles. These other monolayers are more loosely bound than the first monolayer being directly in contact with the surface of the solid. Therefore, they can be removed more easily, since the desorption energy corresponds roughly to the evaporation heat which is about a factor of four less than the adsorption energy in case of a water molecule [136].

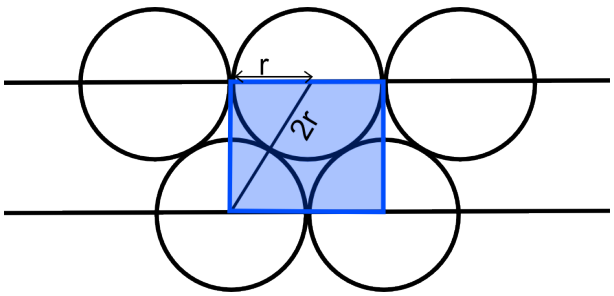


**Figure 4.2:** Smallest rectangular cell on a surface with an area of $A = 2r \cdot \sqrt{3}r = 2\sqrt{3}r^2$ [136].

According to the kinetic gas theory under the assumption of a Maxwell-Boltzmann distribution, the flux of $N$ gas particles of mass $m_p$ incident on the target surface $A$ per time $t$ can be written as

$$j = \frac{N}{At} = \frac{n\overline{v}}{4} = \frac{p}{\sqrt{2\pi m_p k_B T}} = \frac{N_A p}{\sqrt{2\pi M R_m T}}\,. \tag{4.2}$$

Here, $\overline{v} = \sqrt{8k_B T/(\pi m_p)}$ represents the mean velocity according to the Maxwell-Boltzmann distribution. Furthermore, $p$ denotes the gas pressure, $M$ the molar mass of the gas, $R_m$ the molar gas constant, $T$ the gas temperature and $N_A$ the Avogadro constant, respectively. A gas particle hitting the target surface gets adsorbed with the already mentioned sticking probability $s$. Furthermore, the adsorption rate depends on the coverage ratio $\theta$ of the surface defined above. If the target surface is already partly covered with adsorbed gases it will be more difficult for other arriving gas particles to find a free surface position on which they can attach to and, thus, the adsorption rate decreases. From these considerations the resulting adsorption rate $j_{\text{ads}}$ can be estimated to

$$j_{\text{ads}} = (1-\theta)\frac{N_A p}{\sqrt{2\pi M R_m T}} \mathrm{e}^{-E_{\text{act}}/(k_B T)}\,. \tag{4.3}$$

### Desorption kinetics

Due to their thermal energy in the order of few ten meV the adsorbed particles oscillate perpendicular to the target surface with a frequency of $\nu_0 = \nu_0(T_s) \approx 10^{13}\,s^{-1}$ depending on the temperature $T_s$ on the target surface. If their thermal energy becomes larger than the desorption energy $E_{\text{des}}$ during an oscillation away from the target surface, these adsorbates can detach from it. The requirement for this thermal desorption process is only fulfilled by a small number $\Delta\rho = \rho \exp\left(-E_{\text{des}}/(k_B T_s)\right)$ of adsorbates according to the Boltzmann statistics. The rate of thermal desorption then is given by

$$j_{\text{des}} = \frac{d\rho}{dt} = -\nu_0 \cdot \Delta\rho = -\nu_0\, \rho\, \mathrm{e}^{-E_{\text{des}}/(k_B T_s)} \tag{4.4}$$

describing the number of adsorbates with $E_{\text{kin}} > E_{\text{des}}$ multiplied with their oscillation frequency. The averaged time, for which an adsorbed particle stays on the surface before it desorbs, then results in

$$\tau = \tau_0\, \mathrm{e}^{E_{\text{des}}/(k_B T_s)}\,. \tag{4.5}$$

Considering a water molecule, which has a desorption energy of about $E_{\text{des}} \approx 96.5\,\text{kJ/mol} = 1\,\text{eV}$ when attached to an aluminum surface at room temperature $T_s = 300\,\text{K}$, its averaged time of remaining on an aluminum surface yields $\tau \approx 6300\,\text{s} = 1.75\,\text{h}$. For an increased temperature of $T_s = 400\,\text{K}$ the averaged time of surface attachment is reduced to a value of 0.4 s. A rise in temperature increases the thermal desorption substantially. Thus, a so-called bake-out is often used in combination with a pumping system for achieving a lower residual gas pressure.

The desorption kinetics described in this section bases on the thermal motion of gas particles interacting with the once adsorbed particles on the target surface. The desorption occurs without any additional energy transfer from external sources and is in this case in equilibrium with the adsorption. In the performed experiments presented in this thesis, the desorption process is triggered by fs-laser pulses which disturb this equilibrium between adsorption and

desorption in favor of the latter. The underlying microscopic processes of the removal of particles from the target surface are strongly differing from the above discussed thermal desorption kinetics as is shown in the following.

### 4.1.2 Desorption induced by fs-laser pulses

The interaction of ultrashort laser pulses ($\tau_L \ll 1\,\mathrm{ps}$) with metallic, dielectric and semiconductor surfaces has been investigated particularly in the field of femtochemistry since more than two decades. The main interest was to obtain a better insight into the fast dynamics of the nonequilibrium processes of laser energy deposition in the material. But also the resulting microscopic material reactions like ultrafast phase transitions, which are relevant for many applications in medicine, micromachining, material processing etc., should be addressed.

A schematic overview of the microscopic processes of fs-laser desorption and their corresponding time scales is presented in Figure 4.3. When such short laser pulses of sufficient laser fluence interact with the solid, they couple directly to the electronic subsystem via multiphoton excitation. The electrons are immediately released into the conduction band or into the vacuum while the lattice remains cold. On femtosecond time scale, the solid is therefore turned into a highly nonequilibrium state [137] and the excited electrons obey a nonequilibrium distribution function. The excited electrons and the resulting holes left behind in the valence band thermalize quickly by collisions among each other within less than 100 fs. Energy transfer from photoexcited electrons in the substrate to the adsorbed molecules can occur by electrons tunneling through the surface. There, these hot electrons can get attached to the adsorbed molecules and can build transient negative molecular ions before they get inelastically scattered back into unoccupied electron states of the substrate leaving the adsorbate system excited. If the adsorbed molecules gain sufficient energy from the electrons during this transient ion state, they can desorb or exceed the potential barrier to break some chemical bonds [138]. A typical time scale for these processes is some hundreds of femtoseconds.
A part of the photoexcited electrons does not immediately thermalize but travels ballistically into the bulk of the solid [138, 139]. There, these electrons begin to heat the lattice via electron-phonon coupling. The characteristic time scale, on which this energy transfer from

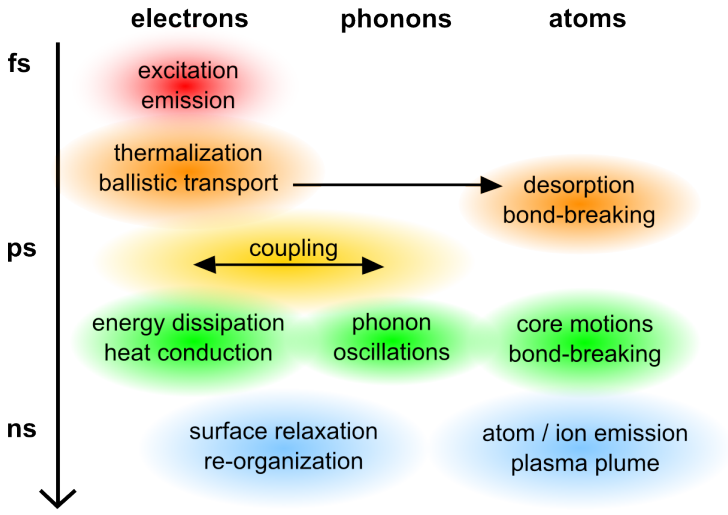


**Figure 4.3:** Overview of the timescale of the microscopic processes during the fs-laser induced desorption process.

the electron system to the phonon system sets in, is commonly named *relaxation time* and takes place on the order of a few picoseconds. A laser-driven shock wave generated at the target front surface travels into the target material and additionally heats the lattice. The lattice heating, which can be regarded as phonon oscillations, causes energy transfer to the adsorbate system finally leading to particle release in form of ablation if the transferred energy exceeds the ablation threshold.
The transient surface defects resulting from the removal of particles begin to self-organize. Surface diffusion starts and the lattice structure reforms on a time scale of some picoseconds to nanoseconds without leaving a significant damage like molten material behind. The process is therefore also known as *nonthermal* melting in the literature because heating of the phonon system comes into play when the lattice is already unstable [137].

### Electron excitation and thermalization

The irradiation of a fs-laser pulse of a wavelength $\lambda_L$ on a metallic surface immediately excites the electrons in the surface region up to the optical penetration depth $l_s = \lambda_L/(4\pi\eta_i)$, where $\eta_i$ denotes the imaginary part of the refractive index [140] of the material. In case of a Ti:sapphire laser ($\lambda_L = 800\,\text{nm}$) the optical penetration depth achieves values between 7.5 nm (Al) and 14.5 nm (Ni). As exemplified in Figure 4.4a), the laser energy absorption by the electrons, originally obeying a Fermi distribution

$$f(E) = \left( e^{\frac{E-E_F}{k_B T_e}} + 1 \right)^{-1} \tag{4.6}$$

with the Fermi energy $E_F$, generates an instantaneous nonthermal electron distribution, in which a part of the electrons has gained the energy $h\nu$ from the absorption of the laser photons. Two different processes towards electron equilibration set in. Like demonstrated in Figure 4.4b), rapid electron thermalization succeeds by collisions between the laser-excited electrons and the electrons near the Fermi level on a femtosecond time scale. The thermalization time of the electrons depends on the available phase space [141, 142] which is defined by the number of available final states for scattering and by the number of present collision partners. The number of final scattering states strongly depends on the specific electronic band structure of the irradiated metal and on the electron excitation [143]. For high electron excess energies $E - E_F$,

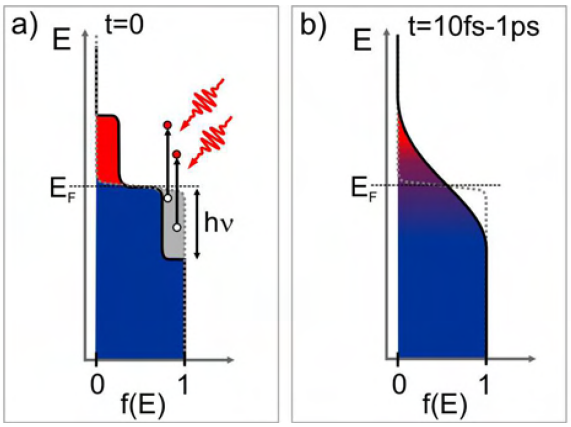


**Figure 4.4:** Thermalization of the electron distribution after excitation by a fs-laser pulse. a) Electron distribution directly after laser excitation. b) Thermalized electron distribution at a higher temperature than the original distribution (dotted line) before laser excitation. The picture was taken from [141].

depicted in red in Figure 4.4b), a large number of final states is available. This enhances the scattering probability and diminishes the lifetime of the excited electron state, thus, thermalization occurs very fast [144]. A decrease of the thermalization time is also obtained for an increasing absorbed laser fluence which creates a higher electron density. A larger amount of electrons is available as potential collision partners leading again to an increased scattering probability. After the thermalization process the electrons are again Fermi-distributed, but at a higher temperature $T_e > T_{ph}$ compared to the lattice.
The second process besides the electron thermalization occurring on the time scale of non-thermalized electrons, i.e. $< 100\,\mathrm{fs}$, represents the ballistic transport of the excited electrons away from the surface into the bulk [138, 139]. The ballistic electrons propagate into the bulk with a velocity $v \approx 10^6\,\mathrm{m/s}$ near to the Fermi velocity $v_F$ [145]. They can reach much deeper regions in the target bulk, in case of gold up to 100 nm [146], in which the optical excitation cannot penetrate. Due to the ballastic electron transport the elecron temperature on the surface decreases.
At larger time scales of a few ps energy transfer both from the ballistically penetrated electrons in the bulk and from the thermalized electrons in the surface region to the lattice takes place in form of electron-phonon coupling. This is the moment at which the successive desorption/ablation physics can be accessed by the so-called two-temperature model (TTM).

### The two-temperature model

A commonly used approach to describe the dynamics of desorption/ablation processes constitutes the two-temperature model (TTM) [147, 148]. It refers to the consideration of a rapidly thermalized hot electron gas of temperature $T_e$ and an initially decoupled cold phonon gas of temperature $T_{ph} < T_e$. The TTM models the temporal evolution of the energy transfer from the electron system to the phonon system. This thermalization process is described by two coupled differential equations in space and time reading

$$c_e(T_e)\frac{\partial T_e(z,t)}{\partial t} = \frac{\partial}{\partial z}\left[\kappa_e(T_e)\frac{\partial T_e(z,t)}{\partial z}\right] - g\,(T_e - T_{ph}) + S(z,t) \tag{4.7a}$$

$$c_{ph}(T_{ph})\frac{\partial T_{ph}(z,t)}{\partial t} = \frac{\partial}{\partial z}\left[\kappa_{ph}(T_{ph})\frac{\partial T_{ph}(z,t)}{\partial z}\right] + g\,(T_e - T_{ph}) \approx g(T_e - T_{ph}), \tag{4.7b}$$

from which the first one accounts for the electron system and the second one addresses the phonon system. The first two expressions of these equations base on Fourier's Law of thermal conduction, which describes the temporal change of internal energy by thermal diffusion due to a temperature gradient. Herein, $c_e$ and $c_{ph}$ denote the heat capacities of the electrons and phonons, respectively, while $\kappa_e$ and $\kappa_{ph}$ represent their thermal conductivities. An additional coupling term $g(T_e - T_{ph})$ between the electron system and the phonon system with the material-dependent coupling strength parameter $g$ takes the energy transfer from the electrons to the lattice into account. The electron-phonon coupling bases on the idea, that the phonons deform the lattice structure locally. The distorted lattice leads to a modified electrostatic potential, which acts back on the electrons moving in that potential such that the electrons get scattered or reflected [146]. Furthermore, the excitation of the electron system by the laser irradiation has to be implemented in the heat flow equation of the electrons. This is done by adding the laser irradiation in form of an external source term $S(z,t)$ to equation (4.7a).
The lateral extension of the laser spot (a few µm) is much larger than the optical penetration depth of the laser light (a few nm), i.e. the lateral temperature gradients become negligible compared to the longitudinal one. This allows to treat the coupled differential equations within an one-dimensional approach with the coordinate $z$ perpendicular to the metal surface.

While for the electron heat capacity in equation (4.7a) the relation $c_e(T_e) = \gamma T_e$ is usually used [149], the phonon heat capacity $c_{ph}$ in equation (4.7b) is often taken from experimental measurements [150].
The thermal conductivity of phonons $\kappa_{ph}$ is much smaller than the one for electrons in metals [149] and can therefore be neglected in equation (4.7b). The electron thermal conductivity $\kappa_e$ shows a strong dependence on the electron and phonon temperature. The electron temperature increases differently for the individual metals due to the laser-induced electron excitation. Noble metals like gold or copper exhibit a strong electron temperature rise upon laser energy absorption but a relatively weak electron-phonon coupling strength in contrast to the group of transitional metals like nickel and aluminum. For these metals the temperature rise is modest but the electron-phonon coupling is quite strong [150]. The thermal diffusion of electrons is therefore higher for noble metals resulting in a larger thermal diffusion length compared to transitional metals.

Under the assumption of a Gaussian temporal profile the source term $S(z,t)$ in equation (4.7a) can be written as

$$S(z,t) = (1-R)\, I(t)\, l_s^{-1}\, \mathrm{e}^{-z/l_s} = (1-R)\, I_0\, l_s^{-1}\, \mathrm{e}^{-z/l_s}\, \mathrm{e}^{-(t-t_0)^2/2\sigma^2} \tag{4.8}$$

and represents the laser energy per time and volume which is absorbed by the electrons in the metal. In this equation, the factor $(1-R)$ with the reflectivity $R$ of the metal accounts for the absorbed part of the incident laser intensity while $I_0$ represents the peak intensity. The standard deviation $\sigma$ of the Gaussian profile is correlated to the laser pulse length by $\tau_L = \Delta_{FWHM} = 2\sigma\sqrt{2\ln(2)}$. The quantity $l_s = \lambda_L/(4\pi\eta_i)$ denotes the optical penetration depth of the laser pulse introduced in the previous section 4.1.2.
The initial energy deposition depth in the metal can strongly be modified when the ballistic electron transport is taken into account [151]. The ballistic electron transport can be included in the TTM by adding the ballistic penetration range $l_b$ to the optical penetration range in equation (4.8), thus substituting $l_s \rightarrow l_s + l_b$.

The set of coupled equations (4.7) can be solved numerically and has proven to be appropriate for the description of laser-induced metal ablation [152, 153]. However, ultrashort laser pulses instantaneously drive the excited electrons out of thermal equilibrium, as described in section 4.1.2. In this case, the introduction of an electron temperature in equation (4.7a) becomes questionable, at least for the first hundreds of femtoseconds, until the electrons have thermalized among each other. A nonthermal description of the electron distribution is provided in [154] by implementing the individual collision integrals of electron-electron, electron-phonon-photon and electron-ion-photon collisions into the Boltzmann equation. The thermalization time of electrons were calculated for Al, Au and Ni showing a strong dependence on the material properties: While nickel thermalizes fast, the thermalization takes longer in case of gold and aluminum. Furthermore, the decrease of the thermalization time with growing absorbed laser fluences (see section 4.1.2) could be validated. The highest analyzed laser fluence was $0.65\,\mathrm{mJ/cm^2}$ which resulted in a thermalization time of about 10 fs for Ni and of about $(2-3)$ fs for Al and Au [154]. This maximum value of the absorbed laser fluence still is roughly one oder of magnitude below the absorbed laser fluences which were applied for the induced desorption process investigated in this thesis. However, following the trend of the curve of Fig. 10 in Ref. [154], shown here in Figure 4.5, this indicates, that the electron thermalization occurs so rapidly, that the concept of an electron temperature can be justified within few fs after the laser-induced electron excitation. Especially for higher laser fluences, the TTM, which assumes a thermal equilibrium condition for the electrons, becomes a very suitable model for

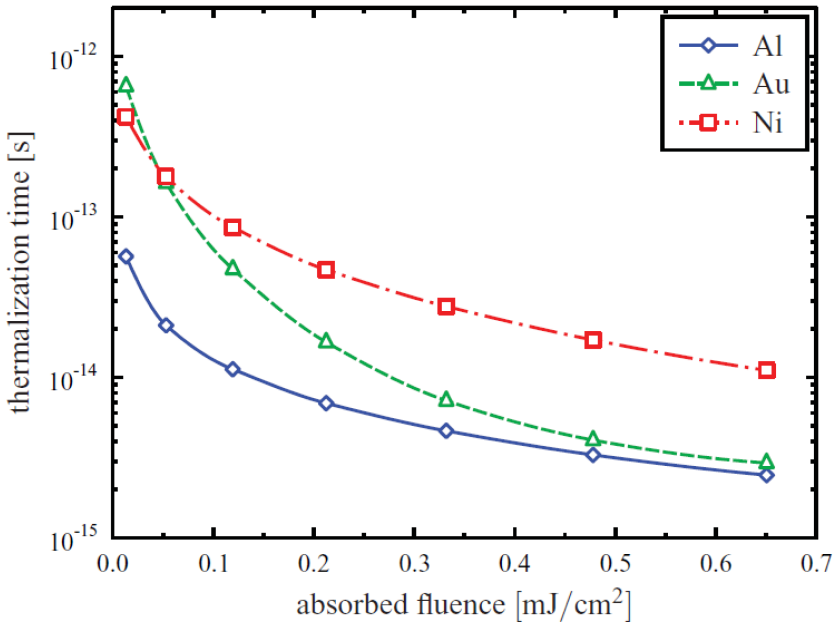


**Figure 4.5:** Electron thermalization time in dependence of the absorbed laser fluence for Al, Au and Ni, taken from [154]. The simulated laser pulse with a wavelength of 800 nm (Ti:sapphire) had a pulse duration of 10 fs.

the description of the energy transfer from the electrons to the lattice.

The TTM provides information about the electron-phonon-coupling as well as the thermal conductivity. But it cannot provide a reliable kinetic description of ultrafast phase transitions under strong nonequlibrium conditions since the corresponding microscopic physics is highly complex and not understood well enough up to now. A promising tool to address the laser-induced desorption/ablation mechanism on a miscroscopic scale is the molecular dynamics (MD) method. It is especially suitable for the analysis of fast nonequilibrium processes because it depends only on the interatomic interaction properties and not on the characteristics of the process itself [151]. It concentrates on the lattice contribution and its interplay with the atoms. However, the electron contribution is not explicitly taken into account.

To overcome the individual limitations of both the TTM and the MD method a combined TTM-MD model was developed. As schematically illustrated in Figure 4.6, the TTM provides an accurate description of the initially heated electron system and its energy transfer to the lattice, i.e. it accounts for the fast particle dynamics in the bulk, while the MD method focuses on the atomic dynamics like melting and ablation on the target surface.
The electron system is still described by equation (4.7a) from the TTM in contrast to the phonon system, whose equation gets substituted by the expression

$$m_j \frac{d^2\mathbf{r}_j}{dt^2} = \mathbf{F}_j + \zeta m_j \mathbf{v}_{j,th} \tag{4.9}$$

with

$$\zeta = \frac{\sum_{k=1}^{n} V_N g(T_{e,k} - T_{ph})}{n \sum_j m_j \mathbf{v}_{j,th}^2}. \tag{4.10}$$

It describes the equation of motion of atoms with mass $m_j$, position $\mathbf{r}_j$ and thermal velocity $\mathbf{v}_{j,th}$. Due to the interatomic interactions the force $\mathbf{F}_j$ acts on atom $j$ and the second term in

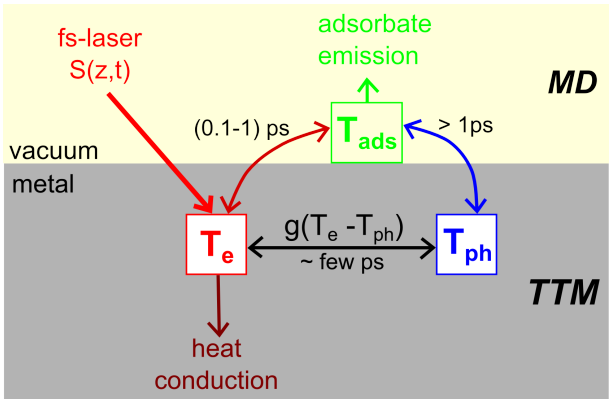


**Figure 4.6:** Schematic overview of the involved processes after fs-laser irradiation with the corresponding time scales. While the TTM accounts for the electron-phonon interactions and the heat conduction of electrons in the bulk, the MD method describes the effects on the atomic motion occurring in the target surface region.

equation (4.9) takes the influence of the electron-phonon coupling on the atoms into account. Herein, the parameter $\zeta$ describes the rate of the energy deposition due to the electron-phonon coupling, considering all the $n$ electrons in a cell volume $V_N$ divided by the thermal kinetic energy of all the atoms in that cell. A detailed derivation of this equation and a more profound introduction into the combined TTM-MD method can be found in [151].

## 4.2 Threshold laser fluence

The irradiation of the target surface with fs-laser pulses should proceed with the lowest arising damage to the target material as possible. The absorbed laser fluence should therefore remain below the critical value of plasma generation, known as the plasma threshold, since plasma formation leads to a substantial modification of the target surface. Due to the occurring phase transitions molten material would roughen the target surface and therefore deteriorate the efficiency of the TNSA. In order to prevent this surface destruction during the fs-laser irradiation, estimates on the threshold fluences were determined by the combined TTM-MD model. The laser source was modeled according to the parameters of the Callisto laser beam providing a pulse duration of 90 fs at a wavelength of 800 nm.

| Sample | $F_{abs}$ [mJ/cm$^2$] | $F_{in}$ [J/cm$^2$] | $I_{in}$ [W/cm$^2$] |
|---|---|---|---|
| Au | 76.5 | 2.550 | $2.83\times10^{13}$ |
| Cu | 25.0 | 0.833 | $9.26\times10^{12}$ |
| Al | 12.0 | 0.092 | $1.03\times10^{12}$ |

**Table 4.1:** Calculated absorbed laser fluences $F_{abs}$ required for cleaning the surfaces of the different materials. The values are chosen to be 10 % below the melting threshold. The corresponding incoming laser fluences are determined by assuming reflectance values of R = 0.87 for aluminum and R = 0.97 for copper and gold. The given incoming laser intensities $I_{in}$ are calculated for the 90 fs Callisto laser beam [1].

In Table 4.1 the numerically computed absorbed laser fluences $F_{\mathrm{abs}}$ for the irradiation of the used target materials gold, copper and aluminum with one single laser pulse are presented. These refer to the values lying 10 % below the melting threshold. The reflection of laser light on the target surface was not taken into account in the simulation. The numerical model regarded only the amount of energy transferred from the laser source to the target material, like it is described in the former section. The corresponding incoming laser fluences $F_{\mathrm{in}}$ in Table 4.1 are obtained via the relation $F_{\mathrm{abs}} = (1-R)\,F_{\mathrm{in}}$. Here, $R$ denotes the reflectance which varies for the different materials from $R = 0.87$ (aluminum) to $R = 0.97$ (copper and gold) at a laser wavelength of 800 nm, when pure metallic surfaces are assumed. The corresponding incoming laser intensities $I_{\mathrm{in}}$ given in Table 4.1 are calculated considering a pulse duration of 90 fs for the Callisto laser beam.

## 4.3 Experimental setup

The detection of the desorbed particles during the fs-laser irradiation constitutes a quite demanding task. The amount of desorbed particles from the laser-irradiated area is very small. Therefore, it necessitates a very low vacuum pressure in the target chamber for measuring the laser-induced desorption yield such, that the latter can be distinguished from the residual gases still present in the target chamber. However, the target chamber pressure in usual TNSA experiments does not fall below $(10^{-6} - 10^{-7})$ mbar due to a plenty of optical components like mounts, lenses and mirrors which greatly enlarge the surface of possible gas adsorption. That pressure value does not suffice to be sensitive to the desorbed particles. Therefore, a separate experiment investigating the desorption characteristics of the laser-induced desorption process on gold, copper and aluminum foils was conducted at GSI Helmholtzzentrum für Schwerionenforschung GmbH using the fs-frontend of the Petawatt High Energy Laser for Heavy Ion eXperiments (PHELIX) laser [155]. This experiment took place in a special ultrahigh vacuum (UHV) target chamber with a residual gas pressure of $2 \times 10^{-10}$ mbar. This low residual gas background enabled to measure the yield of the desorbed particles both with a total pressure gauge head and with a quadrupole mass spectrometer.

The PHELIX laser frontend, operating at a wavelength of $\lambda_L = 1053$ nm, delivered pulses of 420 fs pulse duration with a repetition rate of 10 Hz. The laser pulses were focused onto the target to a spot diameter of 560 µm which refers to its full width at half maximum (FWHM) value considering a Gaussian beam profile. For the investigation of different laser fluences, which irradiated the metal foils, the pulse energies were increased stepwise between 0.06 mJ and 1.0 mJ while the focal spot diameter was held constant throughout the experiment. The laser energy increase was regulated by a waveplate. According to its actual position the waveplate lets the linearly polarized laser light pass to a certain degree and thereby it determines, how much laser energy is transported to the target. The incident laser fluence of the desorption beam achieved values in the range of $F_{\mathrm{in}} = (24 - 406)\,\mathrm{mJ/cm^2}$ corresponding to intensities in the order of $(10^{11} - 10^{12})\,\mathrm{W/cm^2}$.

Figure 4.7(a) illustrates a sketch of the experimental setup while Figure 4.7(b) shows a photograph of the real setup from the laser beamline before the laser enters the target chamber. After having passed a focusing lens with a focal length of 1 m, the laser beam entered the UHV target chamber through a glas flange and irradiated 1 mm thick aluminum, copper or gold targets mounted on a UHV-compatible target ladder. The low pressure value inside the target chamber was reached by using a combined titanium sublimation pump (TSP) and ion pump (IP), in this case a Low Profile 400/320 Ion Pump with angle pole pieces from Physical Electronics [156].

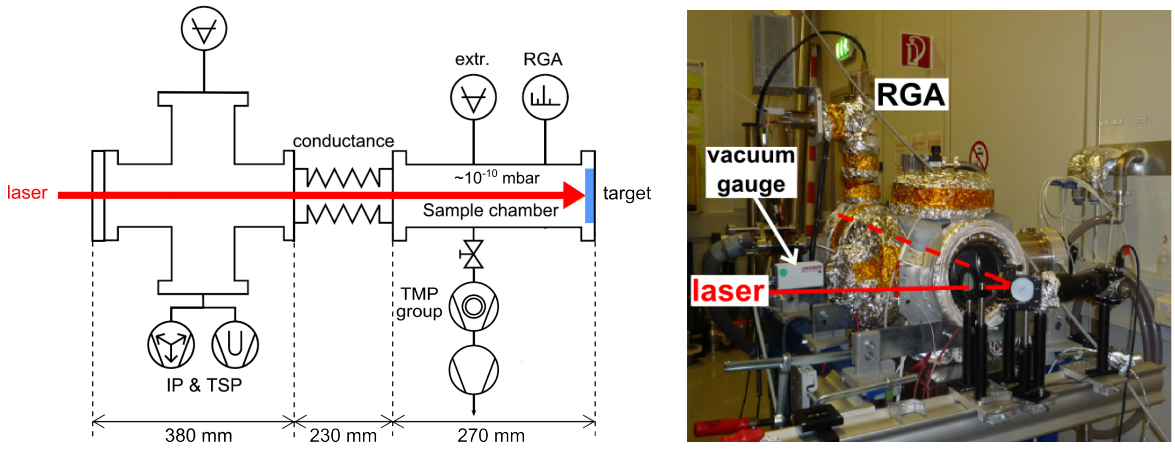


(a) (b)

**Figure 4.7:** (a): Schematic view of experimental setup (not true to scale): The laser beam enters the UHV chamber from the left and is focused onto the target to a spot diameter of 560 µm. (b): Image of the setup from the laser entrance side.

The working principle of the TSP consists of coating the chamber walls of the pump with a titanium film on which colliding reactive gas atoms get absorbed. In the ion pump gas atoms become ionized when entering it and are accelerated to a chemically active cathode by a strong electrical potential. Due to their impact on the cathode they get implanted and can sputter cathode material onto the walls of the pump, comparably to the TSP. Since these UHV pumps need an initial vacuum pressure of already about $10^{-6}$ mbar in order to work properly, a turbo-molecular pump (TMP) was launched in the early pumping phase.
A vacuum gauge of type IONIVAC-Sensor IE 514 from Leybold with a measurement range of $(10^{-4}—10^{-12})$ mbar [157], denoted as extractor (extr.) in Figure 4.7(a), provided the total pressure measurement. The gas molecules entering the vacuum gauge become ionized by electron impact and are accelerated to a collector electrode which is shielded from parasitic background radiation and which measures the ion charge. The ion current on the collector electrode is proportional to the ionization rate which depends on the ionization cross section as well as the particle density. The latter is proportional to the rest gas pressure in the UHV chamber and, thus, an indirect total pressure measurement is performed. In addition to that, the residual gas anaysis (RGA) was performed by a quadrupole mass spectrometer of type Prisma$^{TM}$ QMS 200 from Pfeiffer Vacuum having a mass range of $m/q = (1—100)$ atomic mass units (amu), a lower detection limit of $10^{-14}$ mbar and a mass resolution $\Delta$m smaller than 0.1 amu [158]. Both the total and the partial pressure measuring instruments were flanged to the UHV chamber without having a direct sight onto the target in order to protect them from parasitic radiation emitted during the desorption. Therefore, the desorbed gas molecules experienced many collisions with the chamber walls before they reached the vacuum gauge or the RGA.

## 4.4 Re-adsorption

The desorption pulses irradiated the target with a repetition rate of 10 Hz, i.e. the period of time between the individual pulses was 100 ms. In these 100 ms re-adsorption of residual gases and of the once desorbed particles may occur. Depending on the pressure value in the vacuum chamber the re-adsorption will play a considerable role and has to be taken into account as an effect counteracting the laser-induced desorption. The time until a target surface is covered with one monolayer of adsorbates can be approximated from equation (4.3) in section 4.1.1.

Assuming that the adsorbed gas particles will remain on the target surface, which refers to a sticking probability of $s = 1$, and that at the initial time $t = 0$ the surface is completely uncovered, i.e. $\theta = 0$, the time necessary for the formation of one monolayer of adsorbates is obtained by

$$t_{mono} = \frac{\rho_{mono}}{j} = \frac{\sqrt{2\pi M R_m T}}{N_A p} \times 10^{15}\mathrm{cm}^{-2} = \frac{\sqrt{20\pi M R_m T}}{N_A p[\mathrm{mbar}]} \times 10^{15}\mathrm{s}\,. \tag{4.11}$$

Considering a molecular mass $M \approx 29$ g/mol of the residual gas according to normal air condition and a gas temperature of $T \approx 300\,\mathrm{K}$ in the target chamber, it takes

$$t_{mono} \approx \frac{3.6 \times 10^{-6}}{p[\mathrm{mbar}]}\, s \tag{4.12}$$

until the target surface is covered with one monolayer of residual gas particles at a residual gas pressure $p$ given in mbar. Thus, a pressure below $3.6 \times 10^{-5}$ mbar is necessary in order to prevent the re-establishment of one monolayer of adsorbates within the time interval of two consecutive laser pulses. This pressure value regards the worst case scenario since it would increase if the target surface was already covered with adsorbates to a certain degree or if the sticking probability was less than one.

## 4.5 Total pressure measurements

### 4.5.1 Pressure rise method

From the equation of state of a classical ideal gas it follows, that the particle number $N$ in a closed system of volume $V$ and temperature $T$ is given by

$$N = \frac{p \cdot V}{k_B T} \tag{4.13}$$

with the Boltzmann constant $k_B$. When gas particles get desorbed from a surface in this system, the pressure rises. Since the number of these desorbed particles $N_{\mathrm{des}}$ is proportional to the pressure rise $\Delta p$, it can be determined by

$$N_{\mathrm{des}} = \frac{\Delta p_{\mathrm{des}} \cdot V}{k_B T}\,. \tag{4.14}$$

This equation accounts for the desorption induced by a single laser shot [159, 160]. The pumping speed is considered to be low enough such that the pressure rise can be measured without taking the continuous pumping effect into account.
The application of many laser pulses induces a continuous desorption on a certain time scale. Two concurring processes set in. The laser-induced particle desorption leads to a pressure increase in the target chamber comparable to a vacuum leak while the ion pump provides a removal of residual gases, thus, inducing a pressure decrease. The resulting change of the total particle number in the vacuum chamber with time is obtained from deriving equation (4.13) with respect to time and yields

$$\frac{dN}{dt} = \frac{1}{k_B T}\left(V\frac{dp}{dt} + p\frac{dV}{dt}\right) = \frac{1}{k_B T}\left(V \cdot \frac{dp}{dt} + p \cdot S_{\mathrm{eff}}\right). \tag{4.15}$$

In this equation, the temperature was considered to remain globally constant in the target chamber volume although an increased temperature may locally arise on the target surface due to the laser irradiation. The first term on the right-hand side describes the pressure rise as a result of the laser desorption. The second term accounts for the pumped volume per time, which can be approximated by the effective pumping speed $S_{\text{eff}} = dV/dt$ at a given pressure. It takes into account that pumping is provided through a conductance $L$. This generally involves a resistance to the particle flow and, thus, the pumping speed $S$ decreases resulting in an effective pumping speed $S_{\text{eff}}$ according to

$$S_{\text{eff}} = \left(\frac{1}{S} + \frac{1}{L}\right)^{-1} . \tag{4.16}$$

After an instantaneous strong pressure increase due to the laser-induced desorption the pumping speed counteracts the pressure rise. As soon as the pumping speed exceeds the leak rate of desorbed particles, an equlibrium between the amount of desorbed particles and the number of pumped gas molecules establishes such that equation (4.15) becomes zero and

$$V \cdot \frac{dp}{dt} = -p \cdot S_{\text{eff}} . \tag{4.17}$$

From this equation it follows that the pressure drops exponentially with a time constant of $\tau_p = V/S_{\text{eff}}$ and the peak pressure $p_0$ according to $p(t) = p_0 \exp(-t/\tau_p)$ until it might finally approach its value before the onset of the laser irradiation. This behavior is explained by a continuous decrease of the surface density of contaminants due to desorption which in return leads to a reduced amount of desorbed particles with time. Thus, the pressure decrease during the laser-induced desorption is a clear indication of a surface cleaning process visible in almost all total pressure curves shown in this work.
Related to the number of the desorbed particles, the expression $dN/dt = 0$ signifies that

$$\frac{dN_{\text{des}}}{dt} = -\frac{p \cdot S_{\text{eff}}}{k_B T} . \tag{4.18}$$

Integrated over the period of time of continuous irradiation with laser pulses, the number of desorbed particles can be estimated to

$$N_{\text{des}} = -\frac{S_{\text{eff}}}{k_B T} \int_{t_i}^{t_f} p(t)\,dt = \frac{S_{\text{eff}}}{k_B T} \left| \int_{t_i}^{t_f} p(t)\,dt \right| = \frac{S_{\text{eff}}}{k_B T} \Delta p . \tag{4.19}$$

Here, $t_i$ denotes the starting time and $t_f$ the end time of the laser desorption. If more than one laser irradiation cycle is applied, the total amount of desorbed particles will be obtained by summation of the individual contributions of desorbed particles, i.e.

$$N_{\text{des}} = \sum_j N_{\text{des},j} = \frac{S_{\text{eff}}}{k_B T} \sum_j \left| \int_{t_i^j}^{t_f^j} p(t)\,dt \right| = \frac{S_{\text{eff}}}{k_B T} \sum_j \Delta p_j . \tag{4.20}$$

The estimation of the total number of desorbed particles $N_{\text{des}}$ by the so-called pressure rise method is illustrated in Figure 4.8. A total pressure curve in dependence on time is shown containing two cycles of laser irradiation on gold with a laser fluence of $F_{\text{in}} = 144.1\,\text{mJ/cm}^2$. Each irradiation cycle leads to an immediate pressure increase, followed by the above discussed exponential drop on a time scale of several hundred seconds indicating the target surface cleaning. The total number of the desorbed particles is obtained by the sum of the shaded regions,

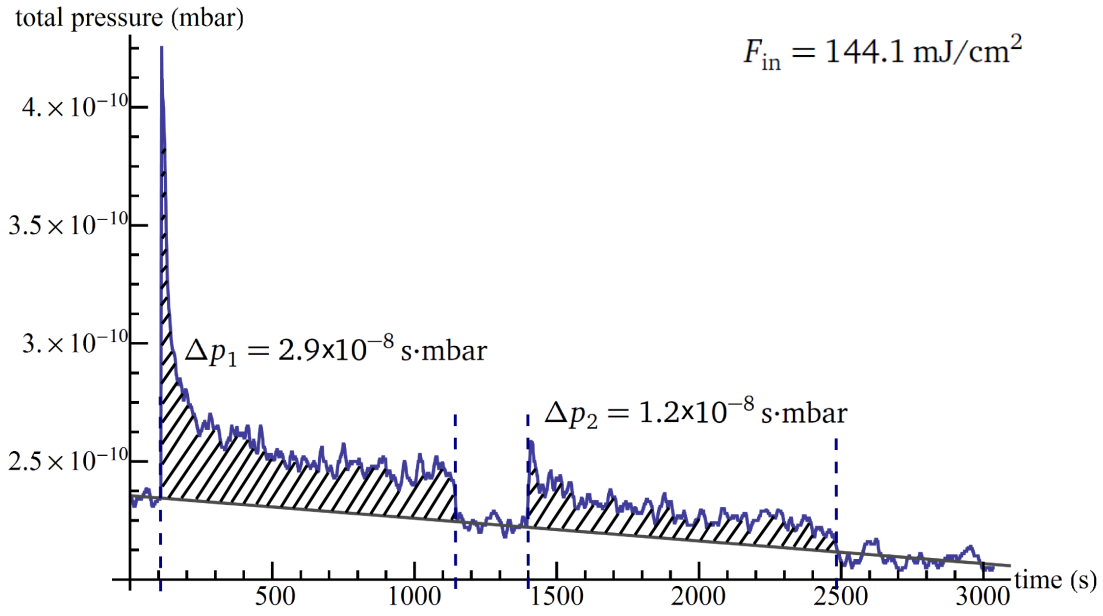


**Figure 4.8:** Time evolution of the total pressure including due to laser irradiation, here on a gold foil with an incoming laser fluence of $F_{in} = 144.1\,mJ/cm^2$. The two irradiation cycles each induce a pressure increase followed by an exponential decay over time indicating a cleaning effect. The pressure increase integrated over the period of laser irradiation, denoted with $\Delta p$, drops from the first to the second irradiation cycle.

denoted with $\Delta p_i$, and multiplying the result with the constant $S_{eff}/(k_B T)$.

The desorbed gas particles normally collide a few times with the chamber walls before entering the vacuum gauge head. Since their sticking probability is larger than zero, the amount of recorded gas particles can only be regarded as an effective desorption yield.
The potential removal of metal atoms of the target material cannot be detected since their sticking probability of remaining attached to the chamber walls after a collision is too high [161]. In contrast, the atoms of the contamination layer reach the vacuum gauge after some collisions with the chamber walls if they build a molecule like $H_2$, $CH_4$, $H_2O$, CO or $CO_2$ and are not chemically bond. These molecules enter the vacuum gauge or the RGA, respectively, where they get ionized either as a molecule or as an atom which became released from its molecular bond as a consequence of dissociation or –in case of $H_2$– even fragmentation.

### 4.5.2 Plasma threshold determination

For an experimental determination of the critical laser fluence, at which a plasma is generated on the target surface, a parameter scan was performed. While the laser pulse duration and the focal spot diameter were held constant throughout the experiment, the pulse energy was successively increased and the amount of desorption pulses was changed.

Irradiating gold and copper targets with an incoming laser fluence below $F_{in} = 105.5\,mJ/cm^2$ did neither lead to any total pressure rise nor did it induce a modification of the partial pressure for the observed masses $m/q = (1-50)$ amu with respect to their background values. Thus, there were no explicit desorption effects visible. Due to the lower reflectance of aluminum with respect to the laser light compared to gold and copper, such negligible desorption effects were observed at lower incoming laser fluences remaining beneath $F_{in} = 22.3\,mJ/cm^2$. The

| | Au, Cu | | Al | |
|---|---|---|---|---|
| | $F_{in}$ [mJ/cm$^2$] | $F_{abs}$ [mJ/cm$^2$] | $F_{in}$ [mJ/cm$^2$] | $F_{abs}$ [mJ/cm$^2$] |
| no desorption | $< 105.5$ | $< 2.1$ | $< 22.3$ | $< 1.1$ |
| desorption | $(105.5 - 292.3)$ | $(2.1 - 5.9)$ | $(22.3 - 105.5)$ | $(1.1 - 5.3)$ |
| plasma formation | 355.3 | 7.1 | 144.1 | 7.2 |

**Table 4.2:** Different regimes of incoming laser fluences $F_{in}$ resulting from the parameter scan study, in which either no desorption effects, visible desorption effects or plasma formation were observed. The absorbed fluences $F_{abs}$ are calculated assuming reflectance values of R = 0.95 for aluminum and R = 0.98 for copper and gold [140].

reflectance of gold and copper at a laser wavelength of $\lambda_L = 1053$ nm results in $R = 0.98$ while its value is reduced to $R = 0.95$ in case of aluminum [140].
Table 4.2 gives an overview of the different observed interaction regimes, i.e. no measurable desorption, visible desorption effects and plasma formation, with their assigned incoming and their corresponding absorbed laser fluences.

Figure 4.9 shows the total pressure rise during the continuous laser irradiation at 10 Hz on a 1 mm thick gold target. In the left image, three irradiation cycles with 1000 s, 2100 s and 500 s, respectively, were applied with an incoming laser fluence of $F_{in} = 243.6$ mJ/cm$^2$. While the first two cycles show an initial pressure rise due to the desorption of surface contaminants, this initial pressure increase did not occur anymore in the third irradiation cycle. Even when the laser irradiation was turned off, the pressure curve did not drop anymore and remained at the same level. This signifies that the surface had been cleaned and there were no more surface contaminants to be removed. Additionally, the laser fluence was still low enough such that plasma formation was no issue. The pressure curve of the first two irradiation cycles shows the common behavior of the pressure decrease due to surface cleaning as it is observed also in case of ion-induced desorption [162, 163], for example. In contrast, the right image of Fig-

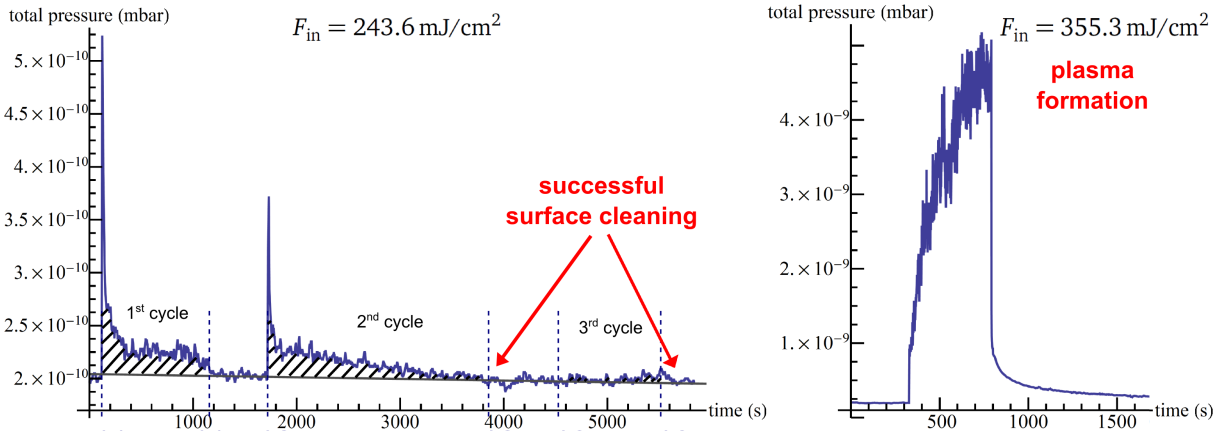


**Figure 4.9:** Time evolution of the total pressure during laser desorption at 10 Hz. At an incoming laser fluence of $F_{in} = 243.6$ mJ/cm$^2$ (left) a complete surface cleaning was achieved at the end of the second irradiation cycle with no pressure rise anymore in the third one. In contrast, plasma formation set in at laser fluence of $F_{in} = 355.3$ mJ/cm$^2$ (right).

ure 4.9 demonstrates that at $F_{in} = 355.3\,mJ/cm^2$, corresponding to an absorbed fluence of $F_{abs} = 7.1\,mJ/cm^2$, the total pressure increase shows a completely different behavior. Instead of decreasing after a short time of laser irradiation, as it was observed in the left image of Figure 4.9, it increases more and more. Plasma formation sets in, which was also recorded by a camera during the experiment, and the absorbed laser fluence sufficed to immediately ionize the contaminants as well as the gold atoms [164].
Similar results were obtained when aluminum and copper foils were irradiated. While for copper the plasma threshold turned out to be in the same laser fluence regime as it was noticed for the gold foil, a lower incoming laser fluence of $F_{in} = 144.1\,mJ/cm^2$ was determined for the onset of plasma formation when the aluminum foil was irradiated. However, according to Table 4.2, the absorbed laser fluence, at which plasma formation was observed for the aluminum target, is nearly identical to the respective ones for gold and copper targets.

The obtained threshold values showed that plasma formation sets in very abruptly as soon as a certain laser fluence is exceeded. The given laser fluence values underlie an error of ±21 %. This error results mainly from the determination of the laser spot diameter and further from the laser energy measurement contributing to ±10 % and ±7 %, respectively.

Figure 4.10 presents some photomicrographs of the irradiated target foils. On the left, the surface modifications of a gold foil after its treatment with the fs-laser desorption are shown. The upper image shows indeed a clear sign of material removal from the target surface, however, with no evidence of molten material on it. The laser fluence has obviously been below the value of the onset of plasma formation, given in Table 4.2. The lower image displays that the material ablation here must have occurred accompanied by plasma formation, since molten material is unambiguously observed. Here, the laser fluence must clearly have exceeded the threshold for plasma formation. The same is valid for the irradiated copper foils, whose photomicrographs are presented in the middle of Figure 4.10. The upper image does not show any molten material on the target surface. In contrast, the lower picture demonstrates that the melting threshold was exceeded by the laser light. In both cases, however, a precise lateral transition between the original copper surface and the region of removed material is noted. The

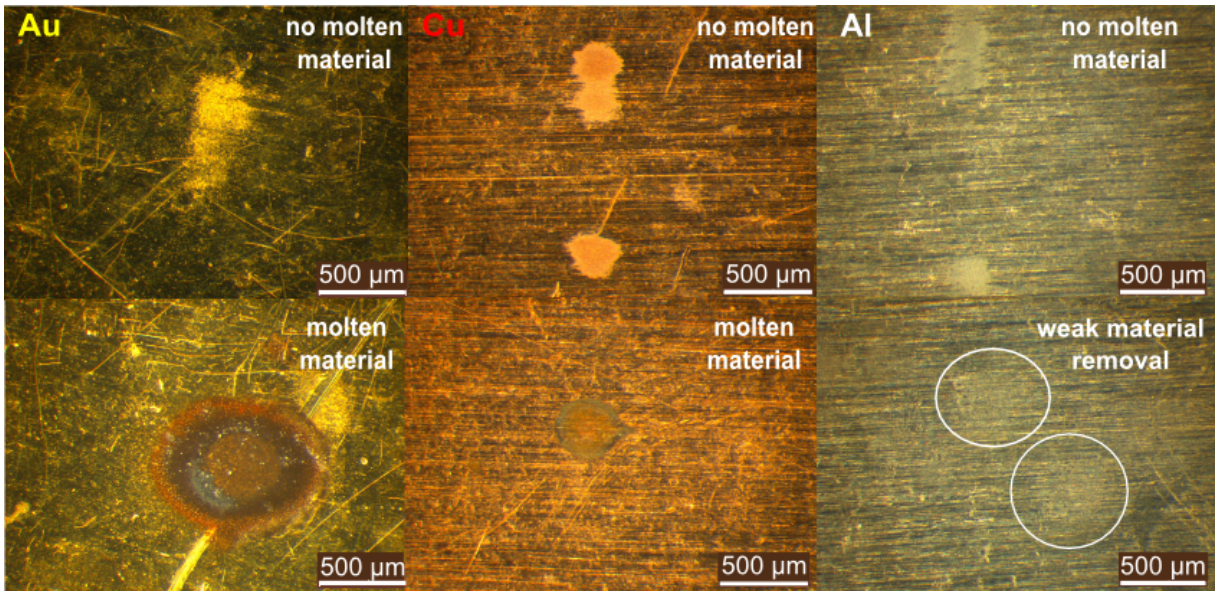


**Figure 4.10:** Photomicrographs of the gold (left), copper (middle) and aluminum (right) foils irradiated with differing laser fluences.

right part of Figure 4.10 illustrates the effects of the fs-laser irradiation on the aluminum target. Here, no obvious melting of the surface material was monitored. While the removal of the surface material is quite evident in the upper image, the lower image exhibits only weak signs of material removal hardly visible on the photomicrograph. These weak surface modifications are surrounded by white ellipses. It can therefore be supposed that the laser fluence remained beneath the value of plasma formation (see Table 4.2).

### Comparison between experiment and theory

The experimentally obtained values of the incoming and absorbed laser fluence, at which a plasma is generated on the target surface, differ from the theoretically obtained values presented in section 4.2. While the experimentally determined threshold value of the absorbed laser fluence for the aluminum target is by a factor of two lower than the theoretically computed threshold value, the difference for the gold target results already in a factor of ten. In general, the same tendency of smaller experimentally obtained threshold fluences than those determined by numerical simulations was already observed in past experiments on ablation studies [165, 166]. The simulated threshold values depend on the chosen model parameters which in the framework of the TTM are e.g. the electron-phonon coupling parameter or the ballistic penetration length and are not sufficiently known. As shown recently in [167], the electron-phonon coupling strength is neither a constant nor a function of the electron and phonon temperatures, like it is assumed in the TTM, but a functional which depends on the electron and phonon energy distributions. It is furthermore affected by the laser fluence as well as its wavelength. Additionally, the TTM approach bases on the description of an already thermalized electron subsystem and does not take into account the transient nonequilibrium distribution of hot electrons directly after laser excitation. This may underestimate the dissipation of the electronic excitation energy by electron diffusion into the bulk, thus leading to higher threshold fluences compared to the experimentally determined values. The conversion of the absorbed laser fluence used in the simulation to an experimental incident laser fluence necessitates the assumption of a reflectivity. Its value was taken from a data base and refers to the calculation within the Fresnel equations. However, the reflectivity depends not only on the material and on the wavelength of the incident light, but may also even change during the desorption [166, 168].
Apart from these rather common explanations the observed discrepancy might also be explained by the following arguments in the present case. Firstly, a laser wavelength of 1053 nm was applied in the desorption experiment in contrast to the wavelength of 800 nm assumed for the numerical model. Although the optical penetration depth $l_s = \lambda_L/(4\pi\eta_i)$ into the target is not affected by a larger laser wavelength $\lambda_L$, since the imaginary refractive index $\eta_i$ also increases with $\lambda_L$ in case of the investigated materials, the photon energy is reduced from 1.55 eV at 800 nm to 1.18 eV at 1053 nm. As discussed in [154, 167], an increased absorption probability of the laser energy was found for decreasing photon energies, and might correspond to an enhanced desorption efficiency for laser pulses with a wavelength of $\lambda_L = 1053$ nm compared to $\lambda_L = 800$ nm. Secondly, the pulse duration of 420 fs was more than a factor of four larger than the 90 fs laser pulse used for calculating the theoretical threshold values. This might also strongly influence the desorption characteristics since the laser energy transfer to the electrons of the target surface is provided on a longer time scale. Thirdly, it has to be taken into account, that the fs-laser pulses irradiated the target surface continuously at 10 Hz repetition rate over a long period of time. Between 5000 and 21000 laser pulses deposited a certain amount of energy into the target material every 100 ms. This long-term laser irradiation might therefore lead to a significant decrease of the threshold values. In contrast, the numerical model for the calculation of the fluence thresholds envisaged only one single laser pulse and not a series of pulses.

When comparing the desorption results presented in this section with laser-induced desorption in the framework of TNSA experiments, it has additionally to be considered, that the desorption experiment here took place in a special UHV chamber, i.e. the re-adsorption between two consecutive laser pulses can be disregarded. The energy of the desorption pulses is not partly transferred to potential re-adsorbed gases on the target surface, but it is transferred completely to the original surface. The resulting higher desorption efficiency therefore leads to a lower threshold fluence compared to the one arising in the framework of TNSA experiments.

### 4.5.3 Contamination layer analysis

For laser fluences in the desorption regime (see Table 4.2) a complete target surface cleaning was provided for all the three investigated materials after maximally three irradiation cycles. This target surface cleaning is defined such, that no influence of the laser irradiation on the total pressure is observed anymore since all the gas adsorbates on the target surface have already been removed. Figure 4.11 illustrates the total pressure curves from the desorption measurements on aluminum at an incoming laser fluence of $F_{\text{in}} = 22.3\,\text{mJ/cm}^2$ (upper image) as well as $F_{\text{in}} = 43.4\,\text{mJ/cm}^2$ (lower image), both indicating a complete cleaning of the target surface comparable to the laser desorption on gold (Figures 4.8 and 4.9, left). The corresponding total pressure curves from the laser desorption on copper are very similar. They are displayed in Figure 4.12, in which a laser fluence of either $F_{\text{in}} = 144.1\,\text{mJ/cm}^2$ (left) or $F_{\text{in}} = 243.6\,\text{mJ/cm}^2$ (right) was applied. The following evaluation of the yield of desorbed particles bases on these six total pressure measurements.
The total number of the desorbed particles could be estimated with the help of the pressure rise method described in section 4.5.1. If the target surface was completely cleaned and no target material was removed, the resulting desorption yield should correspond to the amount of gas particles which composed the contamination layer.

The determination of the total number of desorbed particles by the pressure rise method requires the knowledge of the effective pumping speed $S_{\text{eff}}$ given in equation (4.16).
Generally, the pumping speed $S$ of an ion pump depends both on the species of gas molecules, which should be pumped, and on the actual working pressure. The pumping speed is highest for hydrogen, followed by the further gases contained in the air like carbon dioxide, water vapor, light hydrocarbons, nitrogen and oxygen. Their individual contributions to the total pressure in the target chamber were obtained from the partial pressure measurement. For pressure values up to $10^{-8}\,\text{mbar}$ the pumping speed is nearly constant. Below that value it continuously drops with decreasing pressure reaching roughly 75 % of its original value at $10^{-10}\,\text{mbar}$ according to the manufacturer of the ion pump [156]. At a target chamber pressure of $3 \times 10^{-10}\,\text{mbar}$ the pumping speed resulted in $S = (355 \pm 36)\,\text{l/s}$ for the used Low Profile 400 ion pump from Physical Electronics. Herein, a differential ion pump design was considered[1], which differs from the conventional one by a higher pumping efficiency towards inert gases, but especially by a reduced pumping speed of about one third for the active gases in the air mentioned above.
In order to calculate the conductance $L$ for gas particles flowing through a tube with a diameter of 63 mm and a length of 230 mm, as it was the case for the present experimental setup, the Monte-Carlo simulation program MC_Leitwert developed by Prof. Dr. E. Lux [169] was utilized. Apart from the geometric setup the conductance $L$ depends on the molecular masses of the

[1] Due to the missing serial number the exact type of the ion pump –conventional or differential– could not be reconstructed anymore. The differential type was assumed for the further calculation taking into account the advanced age of the ion pump which reduces its original pumping speed.

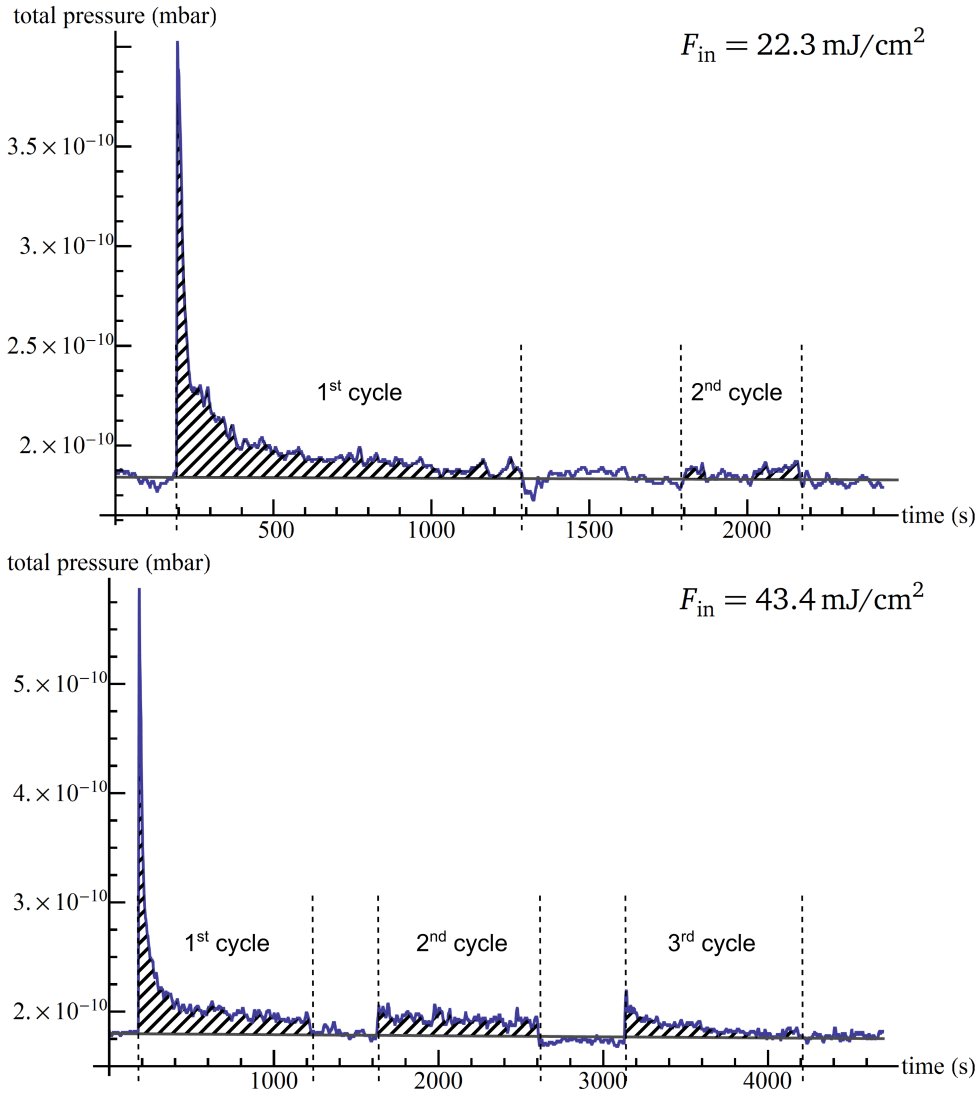


**Figure 4.11:** Total pressure curves from laser desorption on aluminum showing target surface cleaning at an incoming laser fluence of $F_{in} = 22.3\,mJ/cm^2$ (top) and $F_{in} = 43.4\,mJ/cm^2$ (bottom), respectively.

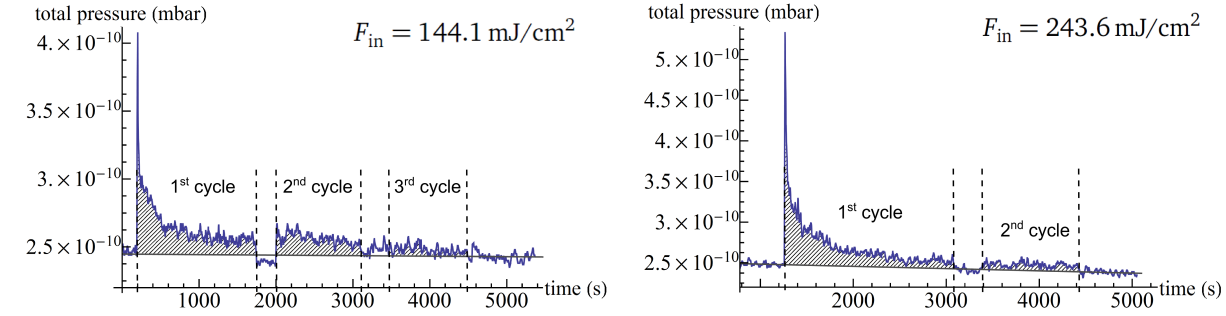


(a) (b)

**Figure 4.12:** Total pressure curves from laser desorption on copper showing target surface cleaning at an incoming laser fluence of (a) $F_{in} = 144.1\,mJ/cm^2$ and (b) $F_{in} = 243.6\,mJ/cm^2$ (b), respectively.

| target | $F_{in}$ ($F_{abs}$) [mJ/cm$^2$] | $\Delta t_j$ [s] | $\Delta p_j$ [$10^{-8}$ s·mbar] | $N_{des}$ [$\times 10^{13}$] | $N_{des}/A$ [$\times 10^{15}$ cm$^{-2}$] |
|---|---|---|---|---|---|
| Au | 144.1 | $\Delta t_1 = 1033$ | $\Delta p_1 = 2.9$ | $9.71 \pm 2.07$ | $39.4 \pm 17.9$ |
| | (2.9) | $\Delta t_2 = 1032$ | $\Delta p_2 = 1.2$ | $4.02 \pm 1.07$ | $16.3 \pm 7.8$ |
| | | $\Delta t = 2065$ | $\Delta p = 4.1$ | $13.73 \pm 2.33$ | $55.7 \pm 19.5$ |
| Au | 243.6 | $\Delta t_1 = 1033$ | $\Delta p_1 = 3.1$ | $10.40 \pm 2.30$ | $42.1 \pm 19.3$ |
| | (4.9) | $\Delta t_2 = 2221$ | $\Delta p_2 = 3.0$ | $10.00 \pm 2.30$ | $40.8 \pm 18.7$ |
| | | $\Delta t = 3254$ | $\Delta p = 6.1$ | $20.40 \pm 3.25$ | $82.9 \pm 26.9$ |
| Cu | 144.1 | $\Delta t_1 = 1549$ | $\Delta p_1 = 3.1$ | $10.40 \pm 2.20$ | $42.1 \pm 19.3$ |
| | (2.9) | $\Delta t_2 = 1085$ | $\Delta p_2 = 1.3$ | $4.35 \pm 1.21$ | $17.7 \pm 8.6$ |
| | | $\Delta t_3 = 1084$ | $\Delta p_3 = 0.5$ | $1.67 \pm 0.91$ | $6.8 \pm 4.6$ |
| | | $\Delta t = 3718$ | $\Delta p = 4.9$ | $16.42 \pm 2.67$ | $66.6 \pm 21.5$ |
| Cu | 243.6 | $\Delta t_1 = 1807$ | $\Delta p_1 = 4.6$ | $15.40 \pm 3.20$ | $62.5 \pm 28.2$ |
| | (4.9) | $\Delta t_2 = 1084$ | $\Delta p_2 = 0.7$ | $2.34 \pm 1.03$ | $9.5 \pm 5.6$ |
| | | $\Delta t = 2891$ | $\Delta p = 5.3$ | $17.74 \pm 3.36$ | $72.0 \pm 28.8$ |
| Al | 22.3 | $\Delta t_1 = 1084$ | $\Delta p_1 = 1.8$ | $6.03 \pm 1.25$ | $24.5 \pm 11.0$ |
| | (1.1) | $\Delta t_2 = 361$ | $\Delta p_2 = 0.1$ | $0.37 \pm 0.34$ | $1.5 \pm 1.5$ |
| | | $\Delta t = 1445$ | $\Delta p = 1.9$ | $6.40 \pm 1.30$ | $26.0 \pm 11.1$ |
| Al | 43.4 | $\Delta t_1 = 1033$ | $\Delta p_1 = 3.4$ | $11.40 \pm 2.50$ | $46.2 \pm 21.1$ |
| | (2.2) | $\Delta t_2 = 1033$ | $\Delta p_2 = 1.5$ | $5.02 \pm 1.43$ | $20.4 \pm 10.0$ |
| | | $\Delta t_3 = 1032$ | $\Delta p_3 = 1.0$ | $3.35 \pm 1.22$ | $13.6 \pm 7.3$ |
| | | $\Delta t = 3098$ | $\Delta p = 5.9$ | $19.77 \pm 3.13$ | $80.2 \pm 24.5$ |

**Table 4.3:** Overview of the obtained pressure rise $\Delta p_j$ for the individual irradiation cycles $j$ of time $\Delta t$ as well as the summed total pressure rise $\Delta p$. The corresponding numbers of the desorbed particles $N_{des}$ as well as their areal density $N_{des}/A$ are given in dependence of the incoming (absorbed) laser fluence $F_{in}$ ($F_{abs}$) of the desorption beam and of the irradiated material.

gas particles flowing through the tube. Considering the most relevant contributions of the individual residual gas molecules, whose fractions result from the partial pressure measurement, a value of $L = (219 \pm 11)$ l/s was obtained. The uncertainty accounts for the determination of the residual gas composition as well as for the deviation between the calculated values and those given in literature.
Altogether, this leads to an effective pumping speed of $S_{eff} = (136 \pm 7)$ l/s in this experiment [170]. A comparison with the value $S^N_{eff} = (80 \pm 5)$ l/s referring to the commonly used $N_2$ equivalent shows that the consideration of the residual gas composition increases the effective pumping speed by almost a factor of two.

The interpolated data points of the total pressure curve were integrated over the periods of laser irradiation and the respective background gas pressure was subtracted. Table 4.3 summarizes the obtained results for the desorption measurements on gold, copper and aluminum targets. Apart from the applied laser fluences the single pressure rises $\Delta p_j$ of each laser irradiation cycle $j$, lasting over a time of $\Delta t_j$, and also the total pressure rise $\Delta p = \sum_j \Delta p_j$ are given.

The respective number of the desorbed gas particles $N_{\mathrm{des}}$ was computed as well as their areal density $N_{\mathrm{des}}/A$. The area, from which particle desorption occurred, was hereby set equal to the laser-irradiated focal spot area which was assumed to be a circle with the focal spot diameter of $(560 \pm 56)\,\mu\mathrm{m}$ (FWHM).

All these measurements listed in Table 4.3 clearly demonstrate, that the yield of desorbed particles drops from the first to the second irradiation cycle, like also from the second to the third one, if present. For instance, as shown in the left diagram of Figure 4.9, the third irradiation cycle on gold could not even be evaluated anymore due to a too low pressure rise. This observation emphasizes the successive character of the cleaning process. Since the re-adsorption of gas molecules between two consecutive laser pulses can be disregarded, the amount of surface contaminants should already has been reduced when the second irradiation cycle begins.

### Fluence dependence of desorption yield

The dependence of the total desorption yield, given in units of the areal density $N_{\mathrm{des}}/A$, on the absorbed laser fluence $F_{\mathrm{abs}}$ is represented in Figure 4.13 by the blue data points and refers to the respective data in Table 4.3. For reasons of comparison, the averaged sum of the atomic areal densities $\overline{\rho}_{ERDA} = (50.4 \pm 2.0) \times 10^{15}$ atoms/cm$^2$ resulting from the ERDA measurements (section 3.1) is included, too, and is marked by the dashed green line. Figure 4.13 demonstrates that the irradiation of the same material, especially in case of gold and aluminum, with a higher laser fluence induces an increased desorption yield. This agrees qualitatively with measurements in the literature indicating a nonlinear rise of the desorption yield with the absorbed fluence [171], but taking into account only single pulses and not a long series of pulses. A potential removal of atoms from the target material cannot contribute to the desorption yield, since these atoms can hardly reach the vacuum gauge, as described in section 4.5.1. But a higher laser fluence leads to a larger energy entry into the target surface. On the one side, an increased electron diffusion of laser-excited electrons into the bulk sets in where the electron energy transfer to the phonons induces heating of the lattice. Diffusion processes from hydrogen on interstitials in the bulk to the surface become enhanced [161]. On the other side, the hot substrate electrons can excite the adsorbate more efficiently by populating higher unoccupied levels of the adsorbate with a higher electron density, followed by relaxing to the electronic ground state. This enables the adsorbate system to accumulate sufficient energy in order to exceed the potential barrier and to decouple from the substrate with a higher rate. Both processes result in an enhanced release of light atoms and, thus, increase the desorption yield. The measured pressure rise is therefore not only caused by the desorption of surface adsorbates but is also accompanied by diffusion of hydrogen from the bulk to the surface followed by their release from the latter.

On a first look, the increase of the desorption yield with the absorbed laser fluence contradicts the assumption that only a cleaning effect of the target surface was involved. According to equation (4.4), replacing the thermal energy $k_B T_s$ by the energy of the laser pulses, it should only take more time for lower laser fluences to clean the target surface due to a decreased desorption rate, but the total amount of surface contaminants, i.e. of desorbed particles, should roughly be the same. This also holds true when taking the large errorbars of the calculated desorption yields into account, as the data points between $F_{\mathrm{abs}} = (2-5)\,\mathrm{mJ/cm^2}$ in Figure 4.13 show. Opposed to that, the aluminum measurement at an absorbed fluence of $F_{\mathrm{abs}} = 1.1\,\mathrm{mJ/cm^2}$ displays a reduced desorption yield although the total pressure curve in Figure 4.11 indicates a complete removal of surface adsorbates. This may be explained as follows. Firstly, the target surface cleaning may not have been completed at the end of the first irradiation cycle, unlike the upper diagram of Figure 4.11 would suggest. Due to the reduced desorption rate

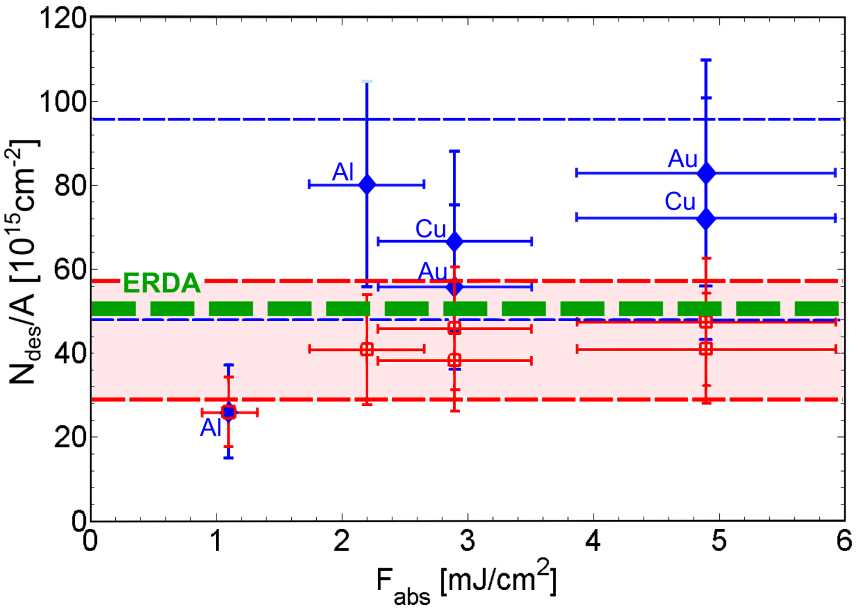


**Figure 4.13:** Total desorption yield in units of the areal density of the desorbed particles $N_{\mathrm{des}}/A$ in dependence on the absorbed laser fluence $F_{\mathrm{abs}}$. The blue data points base on the results in Table 4.3 while the red squares mark the desorption yields modified by a Gaussian correction of the area $A_{\mathrm{des}}$ according to equation (4.21). In addition, the dashed green line represents the averaged sum of the atomic areal densities resulting from the ERDA measurements (section 3.1).

at a lower laser fluence the cleaning process could have proceeded, but the resulting small pressure rise was not measurable anymore. Secondly, the given desorption yields refer to the assumption that the area $A_{\mathrm{des}}$, from which desorption occurred, was equal to the laser spot size at its FWHM, i.e. $A = \pi r_{\mathrm{FWHM}}^2$. Thus, it was considered as a constant value independent of the respective applied laser fluence. However, assuming a radial Gaussian fluence profile $F(r) = F_0 \exp(-2r^2/\sigma^2)$ of the laser pulses with $F_0 = 2F_{\mathrm{in/abs}}$ denoting the peak fluences of the single fluence values presented in this section, the area $A_{\mathrm{des}}$ increases with the applied laser fluence when the laser spot radius $r_{\mathrm{FWHM}}$ is held constant. Supposing that $A_{\mathrm{des}} = \pi r_{\mathrm{des}}^2$, this increase can be estimated by the following relation

$$\frac{A_{\mathrm{des}}}{A} = \frac{r_{\mathrm{des}}^2}{r_{\mathrm{FWHM}}^2} = \frac{\ln\left(F_0/F_{\mathrm{thr}}^{\mathrm{des}}\right)}{\ln 2}, \tag{4.21}$$

where $F_{\mathrm{thr}}^{\mathrm{des}}$ describes the onset of the laser-induced desorption according to Table 4.2. Taking this correction factor into account the calculated desorption yields $N_{\mathrm{des}}/A$, given in Table 4.3 as well as shown in Figure 4.13 by the blue data points, become reduced by a factor of up to two. This is illustrated by the red squares in Figure 4.13, which mark the resulting desorption yields $N_{\mathrm{des}}/A_{\mathrm{des}}$ referring to the area $A_{\mathrm{des}}$ according to equation (4.21). The corrected values of the desorption yields show now a very good agreement with each other, especially what concerns the data points in the fluence regime of $F_{\mathrm{abs}} = (2-5)\,\mathrm{mJ/cm^2}$. A fluence dependence of the desorption yield, as it is observed in the uncorrected blue data points, is almost not visible anymore. This is an indication for a complete target surface cleaning occurring at $F_{\mathrm{abs}} = (2-5)\,\mathrm{mJ/cm^2}$. The arithmetic mean value of the desorption yield in that regime amounts to $(42.7 \pm 3.9) \times 10^{15}\,\mathrm{cm^{-2}}$ and represents a very good estimate on the areal density of the desorbed particles and, thus, of the contamination layer. Furthermore, it agrees very well with the measurements obtained via the ERDA technique described in section 3.1.

A comparison of the obtained areal densities of few $10^{16}$ particles per square centimeter with the areal density of a monolayer $\rho_{\mathrm{mono}}$, as considered in section 4.1.1, shows, that the investigated contamination layers on the single target surfaces must have contained about few ten monolayers of contaminants, i.e. corresponding to a thickness of the contamination layer in the order of a few nm. However, the calculation of the areal densities underlies large errors up to almost ±50 %. While the errors of the temperature measurement and the effective pumping speed contribute only with ±1.5 % and ±5 % to the total error, the main sources of error lie in the determination of the pressure rise $\Delta p$ as well as in the estimation of the area from which the desorption occurred. The uncertainty of the pressure measurement is supposed to be ±25 % and depends on the measuring range as well as the gas species [161]. The output value of the total pressure measurement refers to a $N_2$ equivalent and neglects the dependence of the ionization rate on the gas species. The area, from which the desorption occurred, was first set equal to a circular area irradiated by a laser with a focal spot diameter of $(560 \pm 56)\,\mu\mathrm{m}$ corresponding to its FWHM value. But as already discussed above, the actual surface $A_{\mathrm{des}}$, from which particles are desorbed, differs from that area since it depends on the respective laser fluence as well as on the fluence threshold for desorption. This area can be larger up to a factor of two when assuming a Gaussian fluence profile of a laser pulse having its FWHM well above the desorption threshold fluence $F_{\mathrm{des}}^{\mathrm{thr}}$ which characterizes the onset of the laser-induced desorption. Furthermore, the spatially nonuniform energy distribution across the laser beam profile implicates that each section of the transverse beam profile contributes nonlinearly to the desorption according to its fluence. In contrast, the data given in this section refer to a uniform energy distribution similar to a so-called “flat top” beam profile. Concerning the areal densities $N_{\mathrm{des}}/A$ given in Table 4.3 and in Figure 4.13 by blue data points, an error of ±40 % was therefore assumed for the determination of the area from which desorption occurred. Taking the increase of $A_{\mathrm{des}}$ with the laser fluence according to equation (4.21) into account, the areal density of the contamination layer could be determined with a much better precision yielding an arithmetic mean value of $(42.7 \pm 3.9) \times 10^{15}\,\mathrm{cm}^{-2}$. The error of the individual desorption yields $N_{\mathrm{des}}/A_{\mathrm{des}}$ are also reduced to ±32 % due to a smaller assumed error for $A_{\mathrm{des}}$ of ±20 % arising from the uncertainty of the laser spot diameter.

## 4.6 Partial pressure measurements

The measurement of partial pressure values enables to determine the composition of the desorbed gas and is mainly carried out by mass spectrometers, also known as residual gas analyzers (RGA). These generally consist of the following components: an ion source, a mass analyzer, an ion detector measuring the ion fluxes of the ions divided by their mass-to-charge ratio m/q, the electronics for data acquisition and a computer with a corresponding user software.

The ionization of the atoms and molecules, which should be analyzed, commonly occurs by electron impact ionization. Apart from the emitted electron the reaction products are either an ionized molecule or, as a consequence of dissociation or even fragmentation, an ionized atom or molecule accompanied by a neutral atom or molecule. The generated ions are then extracted by electrodes on a specific potential and are guided into the mass analyzer by slits and apertures, where they are separated according to their mass-to-charge ratio. In case of quadrupole mass spectrometers (QMS), this separation of m/q is done by four parallel electrodes with hyperbolic profiles [172] arranged at an angle of 90° to each other, like it is sketched in Figure 4.14. The opposite electrodes are connected together electrically such that a quadrupole field is generated

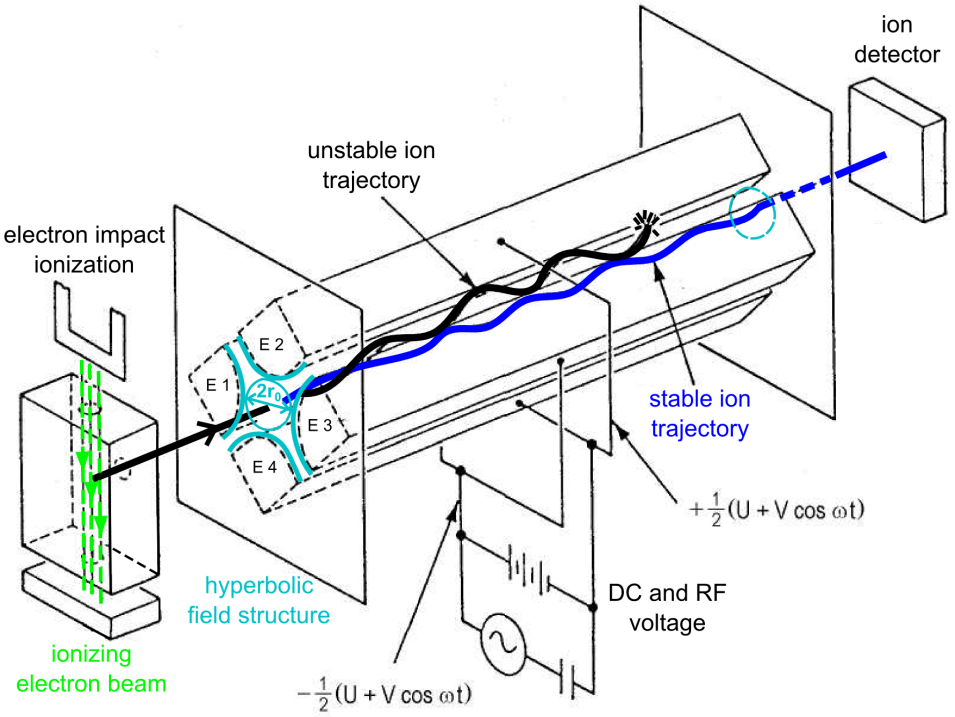


**Figure 4.14:** Schematic view of a quadrupole mass spectrometer with a hyperbolic field structure. Modification of [173].

on the axis of the analyzer. The applied voltage is composed of a direct current (DC) voltage U and a radio frequency (RF) voltage V applied between one pair of the electrodes and the other. These voltages influence the motion of the ions on their way travelling through the electrodes by forcing them to oscillate perpendicular to their propagation direction on sinusoidal curves. Ions with oscillation amplitudes larger than the inscribed radius $r_0$ of the hyperbolic field structure will collide with the electrodes. Only ions of a certain mass-to-charge ratio having an oscillation amplitude less than this radius $r_0$ will be able to travel through the electrodes and to reach the detector for a given ratio of voltages. The ion trajectories are described by the solutions of the so-called Mathieu differential equations [136]. With the help of these equations the stable ion trajectories can be calculated in dependence of the ratio of the applied DC to RF voltages. Successively varying these voltages or the radio frequency it can be scanned through the individual mass-to-charge ratios of the ions obtaining finally an ion spectrum.
In general, the transmission of the ion fluence through the mass spectrometer is determined by its inner radius $r_0$, the length of the electrodes, the applied RF frequency, the ion energy, the injection conditions of the ions into the QMS and by m/q.

An important parameter for quadrupole mass spectroscopy is the working pressure, i.e. the pressure in the target chamber. If it is too high such that the mean free path of the ions travelling through the electrodes is smaller than their distance to the detector, the ions will collide with gas particles on their way to the detector and get lost. Space charge effects can also lead to a screening of the extraction potentials, thus, reducing the measuring sensitivity [174]. Furthermore, the surrounding gas particles leave also a non negligible residual gas signal with the consequence, that the small amount of ions to be analyzed cannot be registrated anymore, since the residual gas background is too high. For a reliable ion analysis the working pressure should at least be a factor of ten lower than the pressure of the ion signal to be measured in order to deliver reasonable results.

Either a Faraday detector or a secondary electron amplifier is employed for the detection of the ions which have been able to pass the quadrupole mass filter. The measurement of these ions by a Faraday detector is the simpler method. After the separation of the ions according to their mass-to-charge ratio they successively reach the Faraday detector, a metal cup, in which the ions hit a collector electrode and their charge is measured. Since the Faraday cup is held on a constant potential, the ion charge gets compensated by an electron current delivered from an ohmic resistance. The resulting drop of the resistance voltage gets amplified and represents a good measure of the ion intensity. However, the readout time is not very fast (about 0.1 s) and the sensitivity, typically $2 \times 10^3$ ions per second [136], is usually not sufficient for the registration of low partial pressures. With the help of secondary electron amplifiers the ions coming from the mass filter hit a first electrode, being on a negative potential, and induce electron emission. These electrons are accelerated to successive electrodes, each on increasing positive potential, and induce a cascade of secondary electron emission. This finally leads to an amplification by a factor of up to $10^7$ [136]. The obtained electron signal is proportional to the incoming ion current and the readout occurs on a time scale of a few ns.

The data processing is performed by the respective user software of the QMS. The software package QuadStar 32-bit was applied in the present case. Apart from the data extraction, the software acts as the control panel, over which the user determines the operating mode and the settings of the measurement. The software implements and controls these settings as well as it transforms the recorded data into an analog mass spectrum. The operating mode used here was the analog scan through the masses ranging from $m/q = (1 - 50)$ amu. The number of measuring points was set to 32 per mass unit and an integration time of 1 s per mass unit was chosen for the measurement of the ion current. Due to the high number of measuring points per mass unit the data acquisition proceeds more slowly, but the arising peaks are registrated with a much higher precision compared to a low number of measuring points.
An example of such an analog mass spectrum with a measurement period of 50 s for one measuring cycle is shown in Figure 4.15 for an aluminum target. The partial pressure is given in

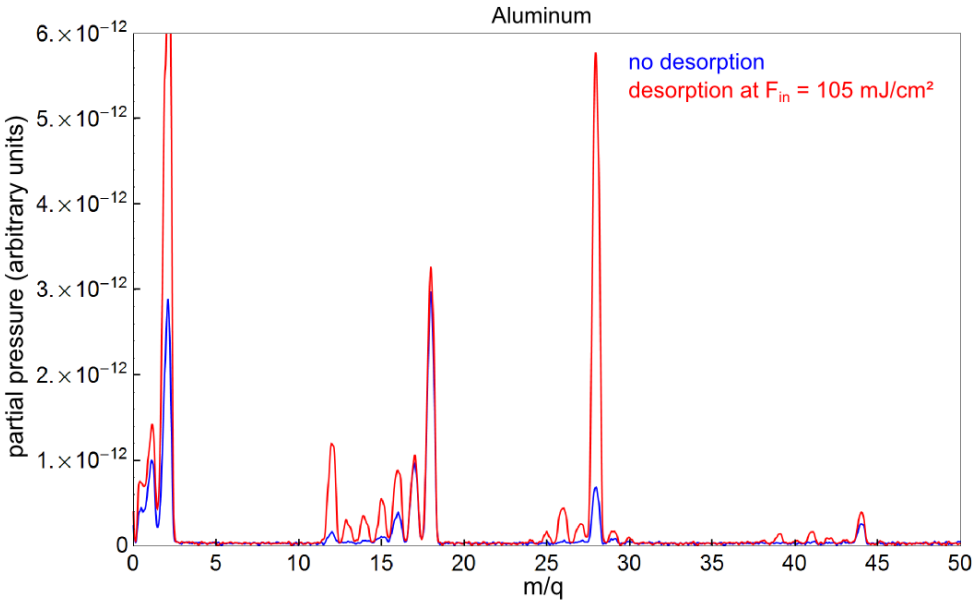


**Figure 4.15:** Analog mass spectrum of an aluminum target showing the measured partial pressure in dependence of the mass-to-charge ratio m/q, for which q = 1 usually. The blue curve presents a background spectrum while the red curve was recorded for the application of fs-laser desorption with an incoming laser fluence of $F_{\text{in}} = 105\,\text{mJ/cm}^2$.

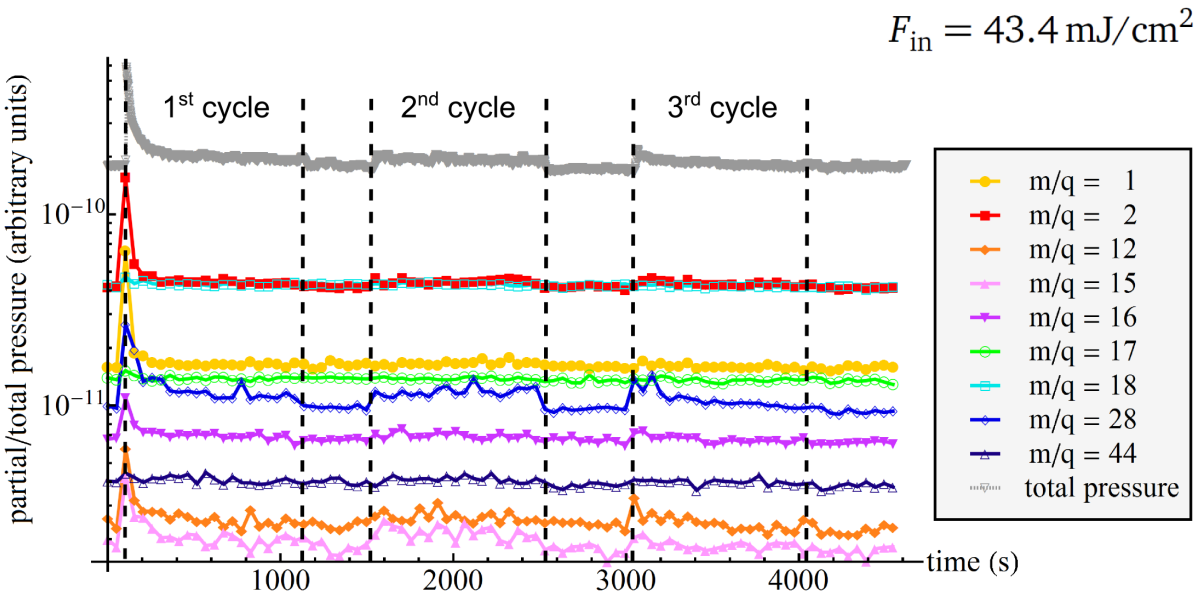


**Figure 4.16:** Logarithmic partial pressure curves for different mass-to-charge ratios m/q resulting from laser desorption on aluminum at an incoming fluence of $F_{in} = 43.4\,mJ/cm^2$.

dependence of the charge-to-mass ratio m/q and is dominated by singly charged gas molecules and atoms, i.e. q = 1. The blue curve describes a background measurement demonstrating that hydrogen (m/q = 1 and 2) and the molecules resulting from the dissociation of water, i.e. $H_2O$ (m/q = 18), OH (m/q = 17) and O (m/q = 16), are the dominating fractions of residual gases in the vacuum chamber, followed by CO (m/q = 28) and $CO_2$ (m/q = 44). Due to the irradiation of the aluminum target with fs-laser pulses of an incoming laser fluence of $F_{in} = 105\,mJ/cm^2$ the resulting red curve shows a strong rise of the partial pressure for CO, hydrogen and carbon (m/q = 12), followed by the light hydrocarbons CH, $CH_2$, $CH_3$ and $CH_4$, like the mass interval m/q = (13 − 16) demonstrates. The release of mainly hydrocarbons due to the laser desorption becomes further evident when looking at the slight rise of the masses in the range of m/q = (25 − 30) marking the group of $C_2H_x$ with $x = 1-6$. Even an increased signal is noted for the masses in the range of m/q = (39 − 44) resulting from the hydrocarbons being formed of three carbon atoms. The peak at m/q = 44, however, describes mainly the contribution of $CO_2$.
These data demonstrate very well that in the presented case the femtosecond laser desorption principally removed adsorbed hydrocarbons from the aluminum surface. The oxide layer was not affected by the laser irradiation which would have had induced a partial pressure increase at m/q = 32 corresponding to $O_2$ as well as a stronger signal for O at m/q = 16. However, both the features are not observable in Figure 4.15.

Figure 4.16 illustrates the temporal evolution of the partial pressures of the relevant mass-to-charge ratios m/q on a logarithmic scale resulting from the laser irradiation of aluminum with an incoming fluence of $F_{in} = 43.4\,mJ/cm^2$. The corresponding total pressure curve, shown in the lower image of Figure 4.11, is included, too, and refers to the last entry listed in Table 4.3. Hydrogen and CO contribute the most to the pressure increase with a respective percentage of (40 ± 10) %. The large fraction of hydrogen mainly results from the desorbed water vapor as well as the hydrocarbons which become dissociated in the RGA, but an enhanced diffusion process of hydrogen from the bulk to the surface due to laser desorption cannot be excluded. The partial pressure of CO, superposed with $C_2H_4$, (m/q = 28), is also significantly enhanced as a consequence of the laser irradiation and still rises in the third irradiation cycle.

This implicates that diffusion processes must have played only a minor role and can be regarded as a concomitant effect. Smaller but still visible contributions arise from carbon (m/q = 12) as well as from hydrocarbons like $CH_3$ (m/q = 15).

## 4.7 Discussion

The obtained results of the desorption measurements have demonstrated, that a successive target surface cleaning up to the complete removal of surface adsorbates could be provided. This occurred when the laser fluence both exceeds the threshold, at which desorption sets in, and remains beneath the threshold for plasma formation. This desorption regime was identified experimentally for the three investigated materials and resulted in an incoming laser fluence of $F_{\text{in}} = (105.5 - 292.3)\,\text{mJ/cm}^2$ for gold and copper as well as $F_{\text{in}} = (22.3 - 105.5)\,\text{mJ/cm}^2$ for aluminum with an uncertainty of ± 21 % in each case. A clear evidence of the complete removal of the contamination layer was obtained which cannot be observed in experiments, in which the desorption is applied prior to the TNSA, since the target chamber pressure in those combined experiments does not fulfill the necessary UHV requirements for being sensitive to desorption measurements. The total pressure rise induced by the laser desorption was converted into the total amount of desorbed particles and allowed to give an estimate on their areal densities. These areal densities of desorbed particles lie in the regime of $(2.6 - 8.3) \times 10^{16}\,\text{cm}^{-2}$ with an error of up to ±50 %. Considering the increase of the area, from which desorption occurs, with the applied laser fluence under the assumption of a radial Gaussian beam profile of the laser pulse, the areal density of the contamination layer could be estimated very precisely to $(4.27 \pm 1.28) \times 10^{16}\,\text{cm}^{-2}$. Moreover, the resulting desorption yields in the fluence regime of $F_{\text{abs}} = (2 - 5)\,\text{mJ/cm}^2$ agreed very well with each other. The partial pressure measurements revealed that the dominant molecular contribution to the contamination layer results from hydrogen and carbonoxide, each amounting to a fraction of $(40 \pm 10)$ %, followed by light hydrocarbons. The large content of hydrogen results mainly from the dissociation of water molecules and light hydrocarbons occurring during the electron impact ionization in the RGA. However, a minor fraction may also be ascribed to enhanced diffusion processes triggered by the long-term laser irradiation.
It should be emphasized at this point, that the obtained areal densities agree very well with the sum of the atomic areal densities obtained from the ERDA measurements in section 3.1. Taking furthermore the determined molecular contributions into account, the corresponding molecular areal densities deviate maximally by a factor of two from the ERDA data.

# 5 Influence of fs-laser desorption on TNSA

The laser-ion acceleration by the TNSA mechanism has gained a lot of interest in the field of particle acceleration physics. These laser-generated ion beams have an initial beam quality at their generation exceeding the beam quality of ions produced by conventional acceleration techniques. This regards especially their transverse emittance [11] and their high particle number in the ion pulse [10, 12]. But as mentioned in section 2.5, two major inconveniences have to be overcome concerning the transport and handling of these laser-generated ion beams. In addition to the evolving beam divergence the ions exhibit an exponential energy spectrum while for most of the applications a monoenergetic ion spectrum is needed. The modification of the ion energy spectrum therefore represented one of the most investigated issues in the field of the TNSA in the last decade. One option of obtaining a quasi-monoenergetic ion spectrum is the usage of magnetic devices as miniature quadrupoles [175] or solenoids [14, 176], which focus ions of a fixed energy on the beam axis while ions with lower or higher energies are defocused or overfocused.
A special target surface treatment was studied in previous experiments which could indicate a resulting quasi-monoenergetic ion beam feature [48, 177]. The group of Hegelich *et al.* removed surface contaminations by resistive heating [48]. At a temperature of the target of 600 K dehydrogenization set in but carbon atoms were still present on the target surface. An increase to about 1100 K provoked a phase transition of carbon into a monolayer of graphite (graphene) and the TNSA ion spectrum showed a quasi-monoenergetic feature of $C^{5+}$ ions with an energy of 3 MeV and an energy spread of 17%. A disadvantage of this method clearly is, that the formation of graphene could not be controlled, since the intermediate states between a full contamination layer on top of the target foil and a completely cleaned target surface were not available by this cleaning method [1]. The group of Schwoerer *et al.* [177] made use of the ns-laser ablation to remove contaminants from a special target design with small dots of hydrogenrich polymethyl methacrylate on the target rear surface. The limited lateral dot size should be smaller than the scale of inhomogeneity of the accelerating electron sheath so that the protons from the dots were assumed to experience the same potential. A quasi-monoenergetic energy spectrum peaked at 1.2 MeV was stated. However, the data was only recorded in a relatively small energy interval.

In this work, a different approach to modify the TNSA ion spectrum was made basing on the irradiation of the target surface with fs-laser pulses. In contrast to resistive heating or ns-laser ablation, the technique of fs-laser desorption enables to remove adsorbed gas contaminants successively, i.e. the intermediate states between the original contamination layer on the target surface and a completely cleaned target surface can be addressed. Opposed to the ns-laser ablation, the fs-laser desorption is a nonthermal surface process, hence, only a reduced heat diffusion [178] sets in when the laser pulse has already passed. The target surface structure becomes much less affected than in case of volumetric processes like resistive heating and ns-laser ablation.

Two experimental campaigns on influencing the TNSA ion spectra by fs-laser desorption were performed at the Callisto laser. The first part of this chapter therefore begins with a description of this laser system in section 5.1. In the following section 5.2 the basic experimental setup of TNSA experiments is introduced schematically before it is presented in detail for both

campaigns. The applied detection methods of the laser-accelerated ions are presented in section 5.3. Besides radiochromic films the main ion diagnostics was a Thomson parabola equipped with either a microchannel plate or an image plate. The first part of the experimental results concentrates on short-term laser desorption and is presented in section 5.4. Gold, copper and aluminum foils were irradiated with up to 165 desorption pulses arriving at the target surface with a repetition rate of 10 Hz. Numerical simulations studying the effect of the contamination layer thickness as well as its composition on the laser-ion acceleration could confirm the experimental findings qualitatively. The second part of the experimental results, section 5.5, focuses on the experimental results obtained by the application of fs-laser desorption over a long period of time. Here, up to 27000 desorption pulses irradiated the target rear surface before the TNSA was initiated. The chapter concludes with a discussion of the results obtained either by short-term or by long-term fs-laser desorption and of their principal differences, given in section 5.6.

## 5.1 The Callisto laser

In the framework of this thesis, the experimental campaigns for studying the effects of the fs-laser desorption as target surface cleaning technique on the TNSA were performed at the Jupiter Laser Facility (JLF) of the Lawrence Livermore National Laboratory (LLNL) in California using the Callisto laser system. The JLF is an open research facility of petawatt (PW)-class lasers for high energy density (HED) science and provides five different laser systems. One of these is the Janus laser, a Nd:glass laser of $\lambda_L = 1.053\,\mu m$, in which the lasing medium consists of a silicate glass which becomes doped by triply ionized neodymium ($Nd^{3+}$). Janus provides two independent long pulse beams, each of $\tau_L \approx (1-20)\,ns$ and a pulse energy of 1 kJ for the $1\omega$ component, called East and West beam, respectively. The Janus East beam is delivered to the Callisto laser system with a maximum repetition rate of 2 shots per hour[1].
Callisto, in earlier years named JanUSP [179] due to its ultra-short-pulse (USP) characteristics while being pumped by a Janus beam, is a Ti:sapphire laser, i.e. working at a wavelength of $\lambda_L = 800\,nm$, being capable of ultrahigh intensities up to $10^{21}\,W/cm^2$ with an intensity contrast of the 1 ns ASE pedestal to the main pulse of $10^7 - 10^8$. It delivers ultrashort laser pulses below 100 fs pulse duration leading to a maximum pulse power of 200 TW at a pulse energy of up to 12 J [180]. This makes the laser system very attractive for investigating physical processes in the HED regime on very short time scales. Its main field of application therefore is devoted to studies on relativistic laser-plasma interaction physics like the laser absorption in the ultra-relativistic regime [98] and the laser wakefield acceleration [181], but it was also used as a fast source for diagnostics development.

An overview of the Callisto laser beamline including the relevant laser parameters is presented in Figure 5.1. The femtosecond frontend is a Spectra-Physics$^{TM}$ Tsunami Ti:sapphire oscillator [183] and generates low energetic short pulses in the nJ regime with pulse durations of 100 fs. These pulses become temporally stretched to pulse lengths of few ns by passing a diffraction grating stretcher which delays the shorter wavelengths more than the longer ones. Afterwards the pulses become amplified in several stages, first by a regenerative amplifier followed by a bow-tie configured five-pass amplifier. Each amplifier uses Ti:sapphire crystals which are pumped by Nd:YAG lasers, i.e. a lasing medium in which the host crystal of the yttrium aluminium garnet (YAG) is doped with $Nd^{3+}$. The resulting pulses have an energy of 200 mJ and a repetition rate of 10 Hz. The main amplifier consists of two Ti:sapphire disks which are pumped by the frequency-doubled ($\lambda = 527\,nm$) Janus East beam of few 100 J, which is transported to

[1] The information about the specific parameters of the five presented laser systems were taken from the JLF-Website `https://jlf.llnl.gov`.

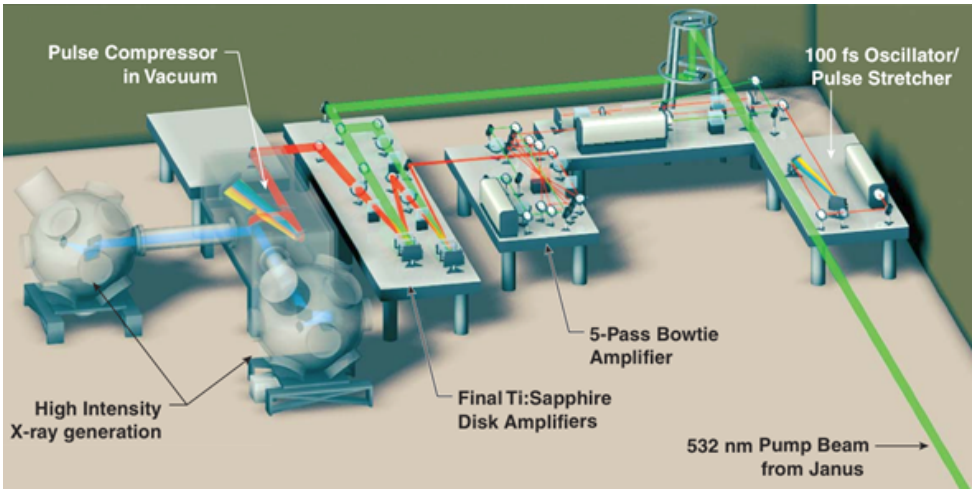


**Figure 5.1:** Setup sketch of the Callisto laser. Low energetic laser pulses of 100 fs pulse duration are generated in the fs-oscillator, become temporally stretched to some ns and amplified in several stages until passing the main amplifier being pumped by the $2\omega$-Janus East beam. In the compressor the laser pulse gets re-compressed and is then transported to the target chamber. Modified picture from [182].

the Callisto beamline in a vacuum tube. Having gained their maximum energy the laser pulses leave the last amplifier chain with a repetition rate of 10 Hz. They are guided into a compressor where they have to pass a dielectric grating under vacuum which confines the pulse in time to less than 100 fs. The process of stretching the laser pulse prior to its amplification and finally re-compressing it afterwards is named *chirped pulse amplification (CPA)* [2] and represents nowadays the standard technology of producing ultrashort laser pulses of high intensity.
With a pulse energy of up to 12 J the CPA beam is guided under vacuum into the target chamber in which the pressure is typically as low as $10^{-5} - 10^{-6}$ mbar. There, the laser pulse is then focused onto the target by an $f/3$ off-axis parabola. The spatial position of both the smallest spot size and of the most regular spatial shape is defined as the target chamber center and determines the position of the target. In the TNSA experiments performed in the framework of this thesis the obtained focal spot diameter was between 12 µm and 15 µm and a laser intensity of $I = (2.2 - 7.0) \times 10^{19}\,\mathrm{W/cm^2}$ was achieved.
Prior to the arrival of the CPA beam, the target was irradiated by low energetic fs-laser pulses of $(0.5 - 2.0)$ mJ inducing the desorption of surface contaminants. These desorption pulses were delivered from the same femtosecond frontend as the CPA beam with a repetition rate of 10 Hz. They initially propagated through the same laser beamline as the CPA beam, but without being amplified, and were then transported in air to the target chamber. There, the desorption beam became either split into two equally energetic beams and was focused onto the target front and rear surface or it was directly focused onto the target rear surface under oblique incidence angles with an incident fluence $F_{\mathrm{in}}$ between $0.2\,\mathrm{J/cm^2}$ and $1.3\,\mathrm{J/cm^2}$. The detailed laser parameters for both the performed experimental campaigns are given in the following section describing the respective experimental setup.

## 5.2 Experimental setup

The experimental setup of laser-ion acceleration experiments applying the fs-laser desorption in order to remove surface adsorbates as shown in Figure 5.2 is quite common. As displayed on the left, the target rear surface on the right of the depicted target is irradiated by a variable

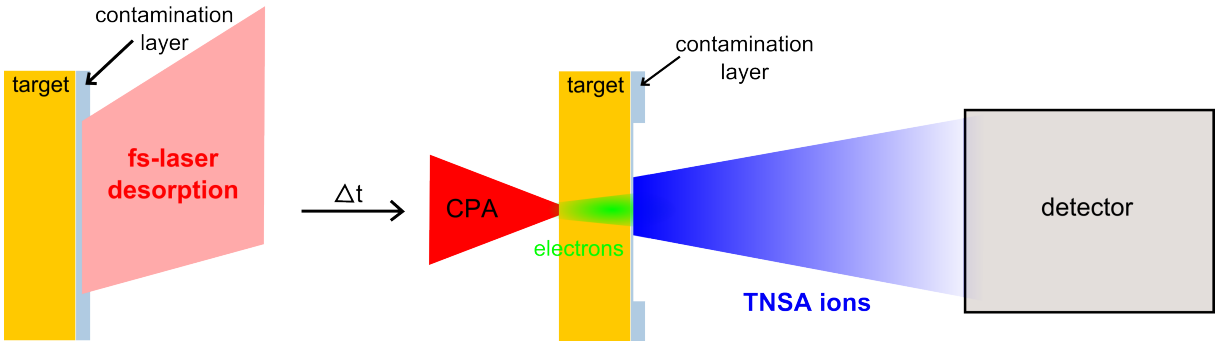


**Figure 5.2:** Sketch of the commonly used setup for influencing the TNSA by fs-laser desorption. The desorption laser irradiates the target rear surface providing a successive removal of the contamination layer (left picture) before the CPA laser beam triggers the TNSA and the accelerated ions get detected (right picture).

number of low energetic fs-laser pulses of up to few mJ inducing the successive desorption of surface contaminations. As the right picture illustrates, shortly after the last desorption pulse the high energetic CPA laser beam arrives at the target front side and initiates the TNSA from the modified target rear surface. The accelerated ions expand in a plasma plume and become recorded in an appropriate ion detector.

The two experimental campaigns dedicated to the usage of fs-laser desorption in order to influence the TNSA were both executed at the Jupiter Laser Facility using the Callisto laser. The detailed setup of both the experiments will be discussed in the following.

For the first experimental campaign Figure 5.3 shows an image of the setup inside the target chamber demonstrating the beamlines of the desorption pulses (green) as well as the CPA beamline (red). The corresponding top view of the experimental setup is sketched in Figure 5.4. The CPA beam with a pulse duration of 90 fs provided pulse energies up to 11 J. It was focused onto the target by the $f/3$ off-axis parabola to a focal spot diameter of 15 µm at an

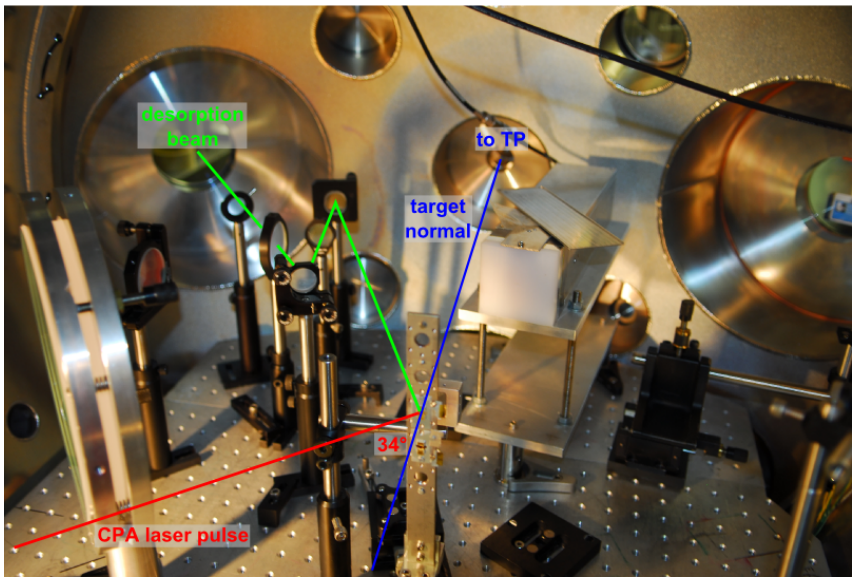


**Figure 5.3:** Experimental setup: The CPA laser pulse (red) is focused onto the target by an off-axis parabola under 34° to the target normal (blue) while the desorption beam (green) is focused onto the target rear side under 27° to the target normal.

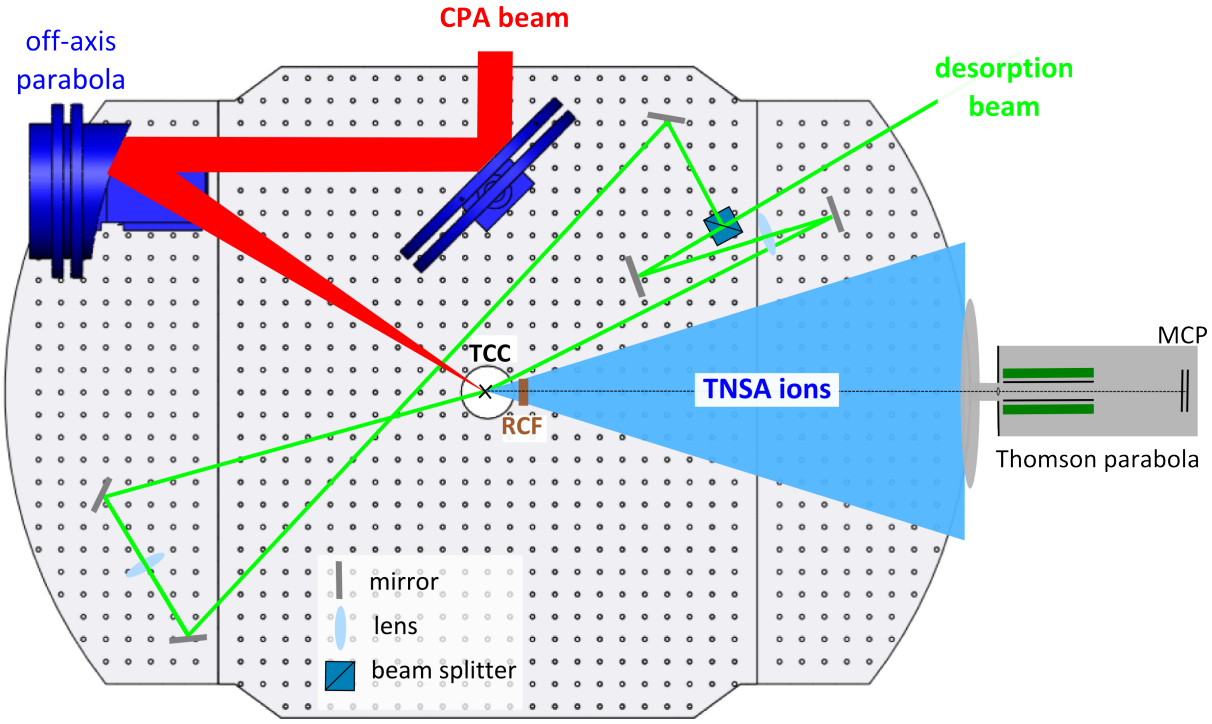


**Figure 5.4:** Experimental setup (top view): The desorption beam (green) is split into two beamlets of equal energy irradiating either the target front and rear surface at the target chamber center (TCC) under incidence angles of 16° and 27°, respectively, or only the target rear surface. The CPA beam (red) inducing the TNSA is focused onto the target by an $f/3$ off-axis parabola under 34° with respect to the target normal. The TNSA ions are recorded both by a Thomson Parabola flanged to the target chamber and a part of them is recorded on a RCF stack.

incidence angle of 34° leading to a maximum laser intensity of $6.9 \times 10^{19}\,\mathrm{W/cm^2}$.
For the successive removal of surface contaminants laser desorption pulses of energies between $1-2\,\mathrm{mJ}$ irradiated thin metal foils of gold, copper (both $10\,\mu\mathrm{m}$) and aluminum ($11\,\mu\mathrm{m}$) shortly before the CPA beam initiated the TNSA process. Throughout the experiment the following parameters of the laser desorption pulses were varied: The focal spot diameter of the desorption beam at its FWHM was either $450\,\mu\mathrm{m}$ or $800\,\mu\mathrm{m}$, resulting in incident laser fluences of $F_{\mathrm{in}} = (0.2-1.3)\,\mathrm{J/cm^2}$ and intensities of $I_{\mathrm{des}} = 10^{12}-10^{13}\,\mathrm{W/cm^2}$. The number of applied desorption pulses varied between 1 and 165. For some shots the desorption beam was split into two equally energetic beamlets directed onto the target front and rear side with incidence angles of 16° and 27°, respectively. The additional front side irradiation was applied in order to suppress proton acceleration from the target front side.
The CPA beam arrived at the cleaned target rear surface with a time delay of 100 ms after the last desorption pulse and triggered the TNSA mechanism. The TNSA ions were recorded by a Thomson parabola equipped with a microchannel plate as ion detector. Additionally, a RCF stack as an independent diagnostics was placed 35 mm behind the target and 5 mm beneath the beam axis recording about one third of the ion signal. The RCF stack consisted of a $11.5\,\mu\mathrm{m}$ thick Al foil for shielding, followed by five to six MD-V2-55 films.

For the second experimental campaign the respective top view of the setup is shown in Figure 5.5. As in the first campaign, the CPA beam (red), this time of 80 fs pulse duration, was focused onto the target with a focal spot diameter of $12\,\mu\mathrm{m}$ and under 28° to the target nor-

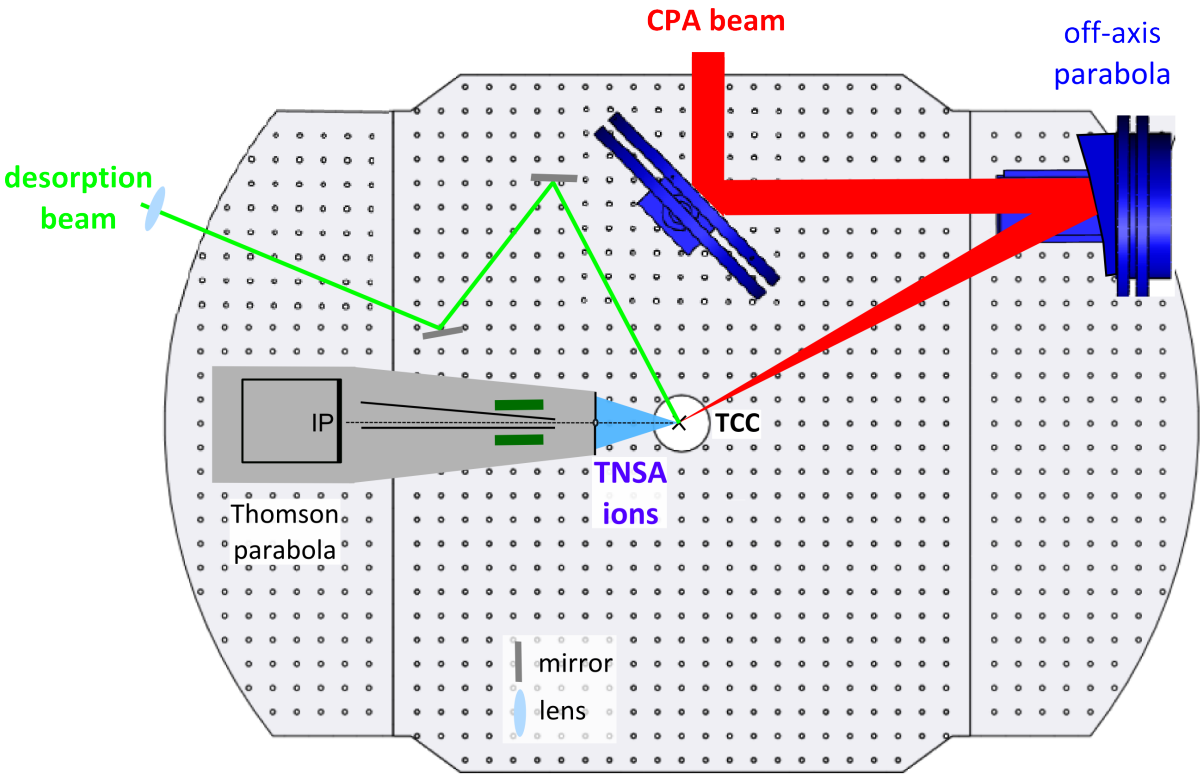


**Figure 5.5:** Experimental setup (top view): The desorption beam (green) irradiates the target rear surface under an incidence angle of 28° while the CPA beam (red) inducing the TNSA is focused by an $f/3$ off-axis parabola onto the target under 28° with respect to the target normal. The TNSA ions enter the Thomson Parabola at a distance of approximately 92 mm from the target and get detected on an IP.

mal. The pulse energies reached values up to 7 J, but could only be determined with a large error of up to 2 J due to an inaccurate energy calibration. The resulting laser intensity was $(1-7)\times 10^{19}\,\mathrm{W/cm^2}$.
A special target design consisting of 5 µm thick gold foils covered on one surface with a nickel layer of a thickness between 10 nm and 40 nm was used, which should enable to analyze how deep the TNSA electric field penetrates into the target material. The desorption pulses (green) with a pulse duration of 250 fs were directed on the target rear side, i.e. the nickel coated surface, under an incidence angle of 28° with a repetition rate of 10 Hz. Their focal spot diameter was $(400\pm 80)$ µm (FWHM) and their pulse energy of 0.6 mJ was not varied throughout the experiment. This led to an incident laser fluence of $F_{\mathrm{in}} = (0.5\pm 0.2)\,\mathrm{J/cm^2}$ and a corresponding intensity of $I_{\mathrm{des}} = (2.0\pm 0.9)\times 10^{12}\,\mathrm{W/cm^2}$. This time, the irradiation with the desorption pulses took place over a long period of time ranging between 15 minutes and 45 minutes. The irradiation time represented the only variation parameter during this experiment.
The CPA beam arrived 100 ms after the last desorption pulse and initiated the TNSA of ions. These were recorded by a Thomson parabola which used image plates as ion detectors.

## 5.3 Ion detection

The characteristics of laser-accelerated ion beams differs substantially from the properties of ion beams generated by standard particle accelerators. Laser-produced ion beams are marked by an initially enormeously compressed ion bunch in time, i.e leading to a very high particle intensity,

which then expands in a plasma cloud. In most cases, this ion bunch is rather a succession of various ion species with decreasing charge-to-mass ratio than an ion bunch of one single ion species. Furthermore, a large amount of gamma-rays and X-rays, followed by hot electrons, stemming from the laser-plasma interaction precede that propagating ion bunch, which itself is accompanied by surrounding plasma particles. The diagnostics of laser-generated ions therefore requires a sophisticated detection system which is capable of providing on the one hand information about a whole set of ion parameters like the ion species, the spatial beam profile and the energy spectrum, and on the other hand capable of neglecting the created electromagnetic noise of gamma rays, X-rays and electrons. For this purpose a combination of different detection methods is usually employed which is nearly insensitive to the created high electromagnetic noise. In order to resolve the spatial ion beam profile, film detectors often come into play, which deliver a good picture of the transversal beam profile. The standard film detectors used in laser-ion acceleration experiments are the so-called radiochromic films (RCF), which change their color to blue when being bombarded by ionizing radiation. Allocated in a stack, they can also provide information about the ion energy spectrum. Since RCFs are sensitive to ionizing radiation in general, they can neither distinguish between different ion species nor between the ion signal and the electron signal. However, the optical imprint of ions differs from that of electrons and heavier ions are already stopped in the first film layers while light ions propagate further into the film stack. Apart from RCF the Thomson Parabola (TP) Spectrometer constitutes another common and convenient diagnostics of laser-generated ions. It delivers information of the individual ion energy spectra of different charge-to-mass ratios by deflecting the incoming ions in a parallel electric and magnetic field according to their charge-to-mass ratio. The deflected ions are then registrated on a film plate like a microchannel plate (MCP) or an image plate (IP). Since the TP cannot registrate a spatial beam profile, it is often used in combination with RCFs.

### 5.3.1 Radiochromic Films

The application of radiochromic films has become a well-established method for the detection of ionizing radiation and comes principally into play in the field of medicine. Here, the dosimetry of radiation [184] is of great importance what concerns either the radiation therapy or the quality control of technical products. RCFs have also found their way into the research field of laser-ion acceleration due to their ability of providing information about both the spatial ion beam profile and the ion energy spectrum.
For the experimental campaign RCFs from Gafchromic [185] of type MD-V2-55[2] were used. These dosimetry films consist of two active layers, each of a thickness of 17.5 µm, which are coated on transparent 96 µm thick polyester. The side of the two active layers is laminated together with a two-side adhesive tape. This tape is composed of roughly 32 µm thick adhesive layers which surround a 25 µm thick clear, transparent polyester base [186]. The active layer is a radiation sensitive monomer which polymerizes upon ionizing radiation. The dosimetry film immediately changes its color from originally transparent to blue since the polymerization changes the absorption spectrum of the film. The darker the blue color is, the higher was the dose of the absorbed ionizing radiation, i.e. the deposited energy per mass. In the following 24 hours the blue color still darkens slightly but after approximately two weeks it remains constant. The polymerization process was studied by McLaughlin *et* al. [187] with a focus on the microchemical time evolution.
The MD films are appropriate for moderate doses, as the abbreviation expresses, with a sensitiv-

[2] http://www.elimpex.com/new/products/radiation_therapy/Gafchromic/content/GAFCHROMIC%20MD-V2-55.pdf

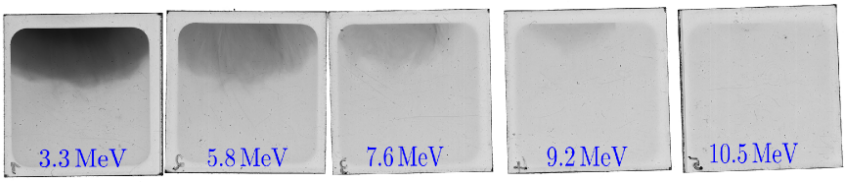


**Figure 5.6:** RCF signal of accelerated protons from a reference shot (shot 1, see section 5.4.1). The energy on each film represents the summed energy loss of protons having penetrated the stack until being stopped in the respective RCF.

ity range of $(1-100)$ Gray according to the manufacturer. They were used for the experimental campaigns since the proton energies were not supposed to be very high due to the applied laser parameters and due to the influence of the fs-laser desorption.

The readout of the RCFs occurs by a calibrated [84] flatbed scanner, Microtek ArtixScan 1800f, which measures the color components of the irradiated films and converts the raw data into optical density (OD)[3]. The maximum OD which can be resolved is about 2.5. Beyond that value saturation effects make a quantitative readout impossible. In order to convert the optical density values of each film into the deposited energy of the protons a calibration of the RCFs is needed. This calibration was performed at the proton accelerator of the Helmholtz-Zentrum Dresden-Rossendorf (HZDR) using monoenergetic proton beams of known beam current which irradiated the RCFs [84, 105].

The dosimetry films react to any kind of ionizing radiation. Since protons have a higher stopping power than electrons or X-rays, the RCFs show a higher sensitivity to them. While electrons deposit a much lower energy on the films than ions and, thus, induce only a change of color into light blue, the different ion species cannot be distinguished. But the calculation of the stopping range of heavier ions shows, that these should already be stopped in the first layers. Protons of high energy propagate deeper into the RCF stack experiencing an energy dependent energy loss in the individual RCFs until they are finally stopped. Thus, the signal visible on the following layers corresponds to protons superposed by X-rays, gamma-rays and a low electron background. The registration of the complete proton spectrum is obtained by using a stack of many RCFs ordered one after another such, that in the ideal case a proton signal is visible on every film except for the last one. This guarantees that all the protons get stopped in the RCFs and no information about high energetic protons is lost.

The reconstruction of the proton beam is performed by the so-called RCF Imaging Spectroscopy (RIS) [114]. With the help of a MATLAB code, developed by M. Schollmeier, K. Harres and F. Nürnberg, protons of a certain kinetic energy in a given energy interval $[E_{\mathrm{min}}, E_{\mathrm{max}}]$ propagating through a given RCF stack configuration are tracked and their energy loss is calculated by considering the Stopping and Range of Ions in Matter (SRIM) [188] energy loss data. A certain proton energy can be attributed to each active layer in the RCF stack. This energy corresponds to the summed energy loss of a proton along its way through the RCFs until being stopped in that specific active layer. Figure 5.6 shows the recorded proton signal on the single RCFs with the corresponding energies a proton needs in order to be stopped in each of them. These data were obtained from a reference shot, i.e. without laser desorption, on a 10 µm thick gold foil.

The advantages of using RCFs for the laser-accelerated ion detection range from a very good

[3] The optical density represents the logarithmic ratio of the incident intensity $I_0$ to the transmitted intensity $I_{\mathrm{trans}}$ through a material at a wavelength $\lambda$ and yields $\mathrm{OD}_\lambda = \log_{10}\left(I_0/I_{\mathrm{trans}}\right)$.

spatial resolution on micrometer scale due to a grain size of ($2\,\mu m \times 2\,\mu m$) of the radiosensitive layer material [84], over the recording of the complete proton spectrum to a relatively simple detection procedure. No technical equipment is needed for the measurement. A rough estimate on the maximum ion energy can directly be made with the help of the described tracking code and the data analysis does not require an extensive film processing. But there are also some disadvantages of using RCFs. In usual laser-ion acceleration experiments the protons can gain energies of several ten MeV. This requires a stack containing a lot of RCFs such that the complete energy spectrum of protons can be recorded. Since the RCFs are very expensive and not reusable, their high consumption causes substantial experimental costs. Furthermore, high proton fluxes lead to an optical density which exceeds the limit of saturation of the dosimetry films and can even destroy them. In case of high intensity laser-ion acceleration experiments, it may therefore be impossible to read out the first RCFs of the stack. Thus, a part of the information about the proton spectrum, namely the low energetic part, is missing.
An option to minimize these mentioned disadvantages constitutes the combination of the RIS with the Nuclear Activation Imaging Spectroscopy (NAIS) [189]. In this technique copper foils of various thicknesses, usually between $50\,\mu m$ and $200\,\mu m$, are alternatingly placed between two RCFs. The protons which are stopped in the copper foils activate them by inducing nuclear reactions. An autoradiography method using image plates (IPs) is applied in order to obtain the photon yield. The latter can then be calculated back to the number of stopped protons by the given half-life of the activated isotope and by considering the energy-dependent single cross sections of the nuclear reactions. The imaging of high energies and high fluxes of protons using the NAIS method is of great benefit since the copper foils do not experience saturation effects. Moreover, they are economic and reusable after few days which reduces the costs for the proton detection to a large extent.

### 5.3.2 Thomson Parabola Spectrometer

The main diagnostics for the detection of TNSA-ions in this thesis constitutes the Thomson Parabola (TP) Spectrometer. In contrast to the ion detection by RCFs, a spatial information of the ion beam profile cannot be obtained with a TP and only a small solid angle element of the ion beam can be registrated. But the TP can distinguish different ion species and with the knowledge of the solid angle element the individual energy spectra of ions with different charge-to-mass ratio $q/m$ are provided. Especially this separation of the ion signal into the various charge states is of crucial importance for the experiments involving the application of fs-laser desorption prior to the TNSA.

A Thomson Parabola is a mass spectrometer named after its inventor J. J. Thomson in which static electric and magnetic fields are arranged in parallel and perpendicular to the ion propagation direction. Its functional principle is illustrated in Figure 5.7. Charged particles entering the TP experience the Lorentz force $\mathbf{F}_L = q(\mathbf{E} + \mathbf{v} \times \mathbf{B})$ and are deflected by the electric and magnetic field according to their charge-to-mass ratio $q/m$. Their resulting trajectory describes a parabola trace. Assuming ideal homogeneous electric and magnetic fields without the appearance of field gradients at the edges, the transversal deflection of nonrelativistic charged particles travelling in z-direction yields

$$x = \frac{qElD}{2E_{\text{kin}}}, \qquad y = \frac{qBlD}{\sqrt{2mE_{\text{kin}}}} \tag{5.1}$$

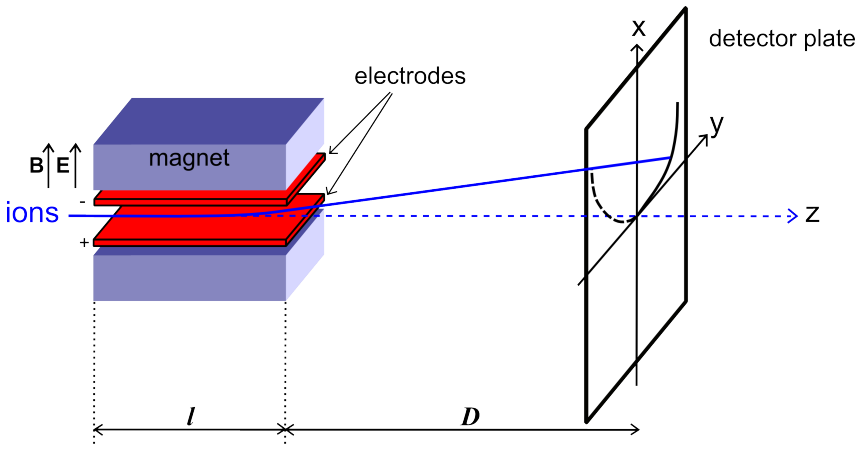


**Figure 5.7:** Mass spectroscopy of ions according to the parabola method of J. J. Thomson. Ions propagating through an electric and magnetic field arranged in parallel experience both a deflection parallel to the electric and perpendicular to the magnetic field according to their energy leaving a parabola trace on the detector plate.

which can be combined to a quadratic equation according to

$$y^2 = \frac{q}{m}\frac{B^2 l D}{E}x\,. \tag{5.2}$$

Here, the electric and magnetic field of strength $E$ and $B$, respectively, are assumed to be in z-direction. The parameter $l$ denotes the length of the electric and magnetic fields while the distance from the exit of the fields to the detector plane is expressed by $D$. The ion's charge state, mass and kinetic energy are expressed by $q$, $m$ and $E_{\text{kin}}$, respectively. Ions with higher kinetic energies are less deflected than those with lower kinetic energies. The quadratic equation (5.2) demonstrates the parabolic deflection characteristic of the ions in dependence of their charge-to-mass ratio $q/m$, i.e. each ion species with a fixed $q/m$ leaves an own parabola trace behind. The individual parabola traces are recorded by a two-dimensional plate detector. Commonly in use are microchannel plates, solid state nuclear track detectors like CR39 or image plates.

### First campaign: Thomson parabola with a microchannel plate

During the first experimental campaign (May 2010) the detection of the accelerated ions was performed by a TP [190] placed under 0° with respect to the target normal at a distance of approximately 1 m from the target. The TP was housed in a separate vacuum chamber, having an independent pumping system in order to protect the detector from target debris, and was flanged to a window of the Callisto target chamber. The TP was equipped with a microchannel plate (MCP) [191] in order to render an online measurement possible. An electric field of 1 MV/m was generated over a length of $l = 100\,\text{mm}$ by two polished copper electrodes of the dimensions $(100 \times 30)\,\text{mm}^2$ having a distance of 20 mm to each other. The magnetic field was generated by an electromagnet over the same field length and achieved a maximum value of 306 mT. In order to minimize the development of heat, the electromagnet was only switched on about ten seconds before the high energy laser shot and switched of directly after the shot. The use of an electromagnet permits to select the energy interval of the ions which should be detected. This adaptability facilitates the operation at different laser systems.
At a distance of $D = 100\,\text{mm}$ behind the end of the electric and magnetic field the ion detection was done by a MCP with an active area of $(90 \times 70)\,\text{mm}^2$. A MCP of a chevron configuration was used actually consisting of two MCPs with slightly angled channels rotated by 180° to

each other. The result is a higher obtainable gain at a certain voltage compared to ordinary MCPs, in the applied case reaching a gain of $10^6 - 10^7$. The electrons, which are generated by the ion impact on the channel walls and become amplified, were collected on a phosphor screen. The resulting image of the individual parabola traces was recorded by a Pixelfly-charge-coupled device (CCD) camera. This method allowed to measure the ion energy spectra online while most of the other detection techniques require an exchange of the detection plates for their data readout. For example, the data analysis of solid state nuclear track detectors as CR-39 [192] made of a polymer is very complicated and it takes several hours to obtain the ion energy spectra for each species. Since the MCP is also sensitive to gamma- and X-rays, the entrance of the TP was furnished with a pinhole having a diameter of 300 μm in order to shield it from the high radiation background and to prevent it from being saturated by a too intense ion signal. Therefore, the number of the recorded ions is limited to a very small fraction of the total ion beam.

### Second campaign: Thomson parabola with an image plate

For the second experimental campaign a different TP [193] was used which was constructed after the design of a TP [194] developed at the Central Laser Facility. The magnetic field is generated by two permanent magnets with a dimension of $(50 \times 50)\,\mathrm{mm}^2$ and reaches a field strength of about 0.6 T for a distance of 20 mm between the poles. Opposed to the conventional TP Spectrometer design having parallel electrodes, the electric field is now generated by a pair of tilted copper electrodes extended over a length of 200 mm, whose separation of the plates is 2 mm at the entrance of the spectrometer and 25 mm at its exit, like shown in Figure 5.5. This construction provides a much higher electric field at the entrance than at the exit such, that it achieves a similar dispersion of protons and carbon ions as the magnetic field. Parallel electrodes over a length of the magnetic field would lead to an insufficent dispersion while the application of longer parallel electrodes would cause ion losses due to collisions with the copper electrodes [194]. With this setup ions of energies between 0.7 MeV and 16 MeV per nucleon could be detected when having passed the pinhole of 300 μm in diameter at the entrance of the TP. The deflected ions were recorded on an image plate approximately 50 mm behind the exit of the electrodes. The IP was mounted on a motorized rotatable drum on which four IPs can be placed in total. In principle, this design enables to execute four high energy laser shots before the vacuum chamber has to be opened for changing the IPs.

Like in case of RCFs, IPs are mostly applied in the field of medicine for X-ray imaging. More and more they have been substituting photographic X-ray films in material research and in molecular biology and found also application as a X-ray diagnostic in the physics of laser-plasma interaction [195]. An IP contains photostimulable phosphors in form of crystals of barium fluorohalide phosphor doped with europium atoms ($BaFBr:Eu^{2+}$) which can store the energy of X-rays, but which are also sensitive to charged particles like electrons and ions. The incident particles excite the phoshor crystals to a metastable state by creating electron-hole pairs whose number is proportional to the absorbed irradiation dose. The electrons get captured in lattice defects acting as electron traps, so-called color centers, which arise in the adjacencies of the particle impact. The europium atoms hinder the holes to move and, thus, to recombine [196]. This state of stored energy in electron-hole pairs is conserved until the color centers are stimulated by the irradiation of red laser light. It excites the trapped electrons which emit blue light when decaying to their ground state. This stimulation occurs during the readout of the IP in a special scanner, in this case of type Fuji Film FLA-7000. The scanner records the emitted radiation which is then converted into a digital image mapping the absorbed particle radiation. Since this readout process does not happen spontaneously but is triggered externally by the laser irradi-

ation, the process is called *photostimulated luminiscence (PSL)*, which corresponds also to the unit of the scanner output signal.
The linear relation between the PSL value and the absorbed particle intensity together with the spatial registration of the energy-dependent ion deflection permit a reliable information about the ion energy spectra. Since the stored information in the IP is read out by red light, which is also present in the daylight, the IPs have to be handled in the dark after having absorbed the particle irradiation until its evaluation procedure. Furthermore, it has to be taken into account that the excited metastable states decay over time with a half life in the order of one hour [197, 198]. Therefore, it was not made use of the four possible IP positions in the rotatable drum, but the IPs were already changed after two laser shots during the experiment.

### Data extraction and energy resolution

The recorded parabola traces of the individual ion species on both the MCP and the IP were analyzed with the help of a tracking code. For both types of the TP the magnetic field distribution was measured while the electric field distribution was simulated by CST EM Studio [199]. For the given electric and magnetic field distribution the code tracks ions of different predetermined energies with a definite charge-to-mass ratio on their way through the TP to the detector plate. The energy dispersion relation is obtained by fitting the tracking points to the corresponding recorded parabola trace and has to be determined separately for each ion species. In order to receive the ion energy spectra the single ion traces of the recorded images of the camera have to be evaluated concerning their brightness on the phosphor screen or the IP, respectively. In case of the MCP, the brightness is correlated to the amount of generated secondary electrons which scales with the number of ions impinging on the MCP. In case of the IP, the brightness corresponds to the amount of photons emitted during the readout of the IP via the photostimulated luminiscence. After the determination of the energy dispersion relation as well as the analysis of the recorded ion trace concerning its brightness an ion energy spectrum either in units of MCP counts or PSL, is obtained. The conversion into real particle numbers can be pursued by a calibration with RCFs for protons and with CR39 for ions [133, 190]. Since the proton signals covered only one third of their spatial beam profile and the proton signals were observed at most to the fifth RCF layer, a thorough calibration with RCFs could not be performed. Therefore, the presented experimental results refer to MCP counts.

The deflection of protons, carbon ions and oxygen ions of different charge states and energies by the given electric and magnetic field distributions was calculated and fitted to the experimentally obtained parabola traces. The best fit to the experimental data was given by the dispersion relation

$$E(x) = \frac{P_1}{x} + \frac{P_2}{x^2} \tag{5.3}$$

with the ion energy $E(x)$ and the deflection $x$ as well as the fit parameters $P_1$ and $P_2$. These had to be determined individually for each charge-to-mass ratio and for both the electric and the magnetic field. Figure 5.8 shows the resulting dispersion relations of protons. The left image, 5.8(a), shows the proton energy as a function of the deflection in the magnetic field while the right image, 5.8(b), shows the corresponding dependence in the electric field. The blue squares result from the tracking code while the curve illustrates the fit to these data points with the fit parameters $P_1^M = 3.88\,\mathrm{MeV\,mm}$ and $P_2^M = 1822.3\,\mathrm{MeV\,mm^2}$ for the magnetic field as well as $P_1^E = 10.98\,\mathrm{MeV\,mm}$ and $P_2^E = 12.09\,\mathrm{MeV\,mm^2}$ for the electric field.

In general, the energy resolution of a TP is influenced by several quantities. The dominant

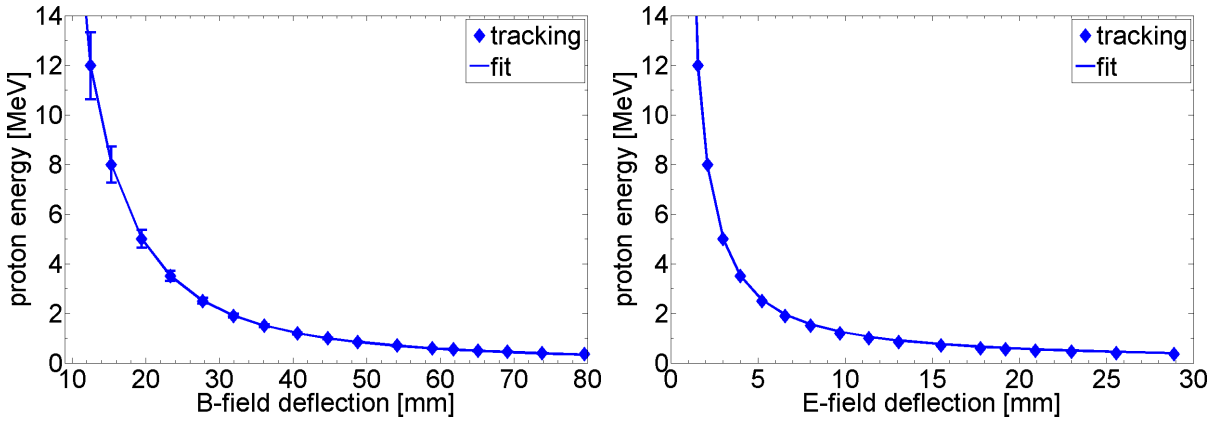


(a) (b)

**Figure 5.8:** Dispersion relations of protons in the magnetic (a) and electric (b) fields. The error bars in (a) were calculated according to equation 5.4.

contribution comes from the size of the pinhole at the entrance of the TP which was 300 µm for both of the experimental campaigns. A smaller pinhole size leads to a spatially smaller ion signal on the detector plate and, thus, to a better energy resolution. But apart from a better shielding against gamma rays and target debris it implicates also a decreased number of ions entering the TP. The ion beam entering the pinhole broadens on its way to the detection plate. This broadening is determined by the geometry of the setup, i.e. the length of electric and magnetic fields $l$ and the drift length $D$, as well as by the beam dynamics, e.g. screening or Coulomb repulsion. The spatial resolution of the detection plate plays also a substantial role.
In case of a MCP, the spatial resolution is determined by the size of the channels and their distance to each other, which is 18 µm [190] for the used MCP. Furthermore, energetic ions may induce electron emission in more than one channel. Due to the chosen two-staged MCP design the electrons broaden between the exit from one channel to the entrance of the second one as well as between the exit of the second one and the phosphor screen. All these effects deteriorate the energy resolution since they result in a broadening of the ion signal.
The spatial resolution of an IP depends decisively on the various scattering processes of the incoming red laser light and the emitted blue fluorescence light in the active layer. The level of excitation and extinction of the color centers by external light and the scanner characteristics, e.g. pixel size, laser spot size and scan velocity, play also a role. Since the luminosity of the stimulated color centers decays within 0.7 µs [196], the photomultiplier may also record the light emitted by the previously excited pixels and not only the emitted light of the presently excited one.

The spatial resolution $\Delta x$ denotes the distance at which two ion signals can just be distinguished from each other and are registrated on the phosphor screen as two separate impacts. The measured signals had a FWHM of 14 camera pixels which corresponded to a length of $\Delta x \approx 0.72$ mm on the phosphor screen.
The energy resolution $\Delta E$ of the TP is correlated to the spatial resolution via the dispersion relation given in equation (5.3) and results in

$$\Delta E = \frac{dE}{dx}\Delta x\,. \tag{5.4}$$

Inserting the derivative of the dispersion relation into equation (5.4) the energy resolution of protons with an energy of 12 MeV results in $\Delta E_{12\,\mathrm{MeV}} = \pm 1.36$ MeV while for protons with 5 MeV a value of $\Delta E_{5\,\mathrm{MeV}} = \pm 0.36$ MeV is obtained.

## 5.4 Short-term laser desorption

The first experimental campaign at the Callisto laser with its setup described in section 5.3.2 considered the irradiation of gold, copper and aluminium targets with a number of fs-laser pulses between one and 165. Thus, the desorption took place on a short time scale of a few seconds. The experimental goal focused on the stepwise cleaning of the target surface by increasing the amount and the intensity of the desorption pulses. The successive decrease of the contamination layer should offer a possibility of modifying the TNSA ion spectrum in a controlled manner.

### 5.4.1 Gold foils

In this subsection the impact of fs-laser desorption on the TNSA from 10 µm thick gold foils is discussed. Figure 5.9 a) shows a Thomson parabola spectrum of a reference shot, labeled in the following as shot 1, in which the CPA beam hit the target and induced the TNSA without any prior laser desorption. It is evident that the most intense ion trace results from the protons. These were accelerated to a maximum energy of 12 MeV like Figure 5.10 demonstrates, in which the proton energy spectra from all the shots mentioned in this section are displayed. The corresponding proton imprint on RCFs contains only the lower third of the complete signal, as shown in Figure 5.6, and therefore recorded less protons of higher energies since these are emitted with smaller divergence angles than protons of lower energies [114, 200]. While a weak signal was still observed on the fifth RCF, which is allocated to a proton energy of 10.5 MeV, the successive film corresponding to an energy of 11.7 MeV did not show a proton signal anymore. Considering the limited proton beam imprint on the RCFs the recorded proton cut-off energy is comparable to the Thomson parabola data. Regarding the heavier ions, $C^{4+}$ was favorably produced and accelerated. This is due to the higher charge-to-mass ratio than $C^{+}$, $C^{2+}$ and $C^{3+}$, therefore experiencing a higher electrostatic force, but the lower ionization potential compared to $C^{5+}$. In addition to carbon ions, traces of oxygen ions with lower particle intensities were observed. Gold ions could not be accelerated in this reference shot indicating that the contamination layer obviously must have been too thick. The contaminants –here in form of protons, carbon and oxygen ions– screen the TNSA field from the target atoms and prevent the latter from getting field-ionized and from getting accelerated. The maximum proton and carbon ion energies for this reference shot and the corresponding shot parameters are listed in Table 5.1. Figure 5.11 displays the obtained ion spectra of $C^{4+}$ and $C^{3+}$ corresponding to the listed shots.

The application of laser desorption changes the TNSA ion spectra strongly. This is shown in the Thomson parabola spectra, Figures 5.9 b), c) and d), for different laser shot parameters. The respective shot parameters and their influence on the ion acceleration are given in detail in Table 5.1. Like shot 2 in Figure 5.9 b) shows, at a moderate number of desorption pulses with an absorbed laser fluence of $F_{\mathrm{abs}} \simeq 13.2\,\mathrm{mJ/cm^2}$, the proton acceleration was hardly affected by the laser desorption. The comparison of the resulting proton spectrum of shot 2 with the reference shot, shot 1, demonstrates a decrease of the particle signal at the high energy end of the spectrum which, however, may also be a consequence of a reduced CPA laser energy. In contrast, the particle spectra of carbon and oxygen ions got strongly modified: Compared to shot 1, carbon and oxygen ions with low charge states, i.e. $C^{+}$, $C^{2+}$, $O^{+}$, $O^{2+}$, $O^{3+}$, completely disappeared and the maximum energy as well as the total amount of the accelerated $C^{3+}$-ions decreased substantially. But the $C^{4+}$-ions gained a maximum kinetic energy which was twice as much as in shot 1. An enhanced signal intensity in the $C^{4+}$-ion trace was noticed for particle energies between 0.18 MeV/u and 0.38 MeV/u, indicated by the red ellipse in Figure 5.9 b). It

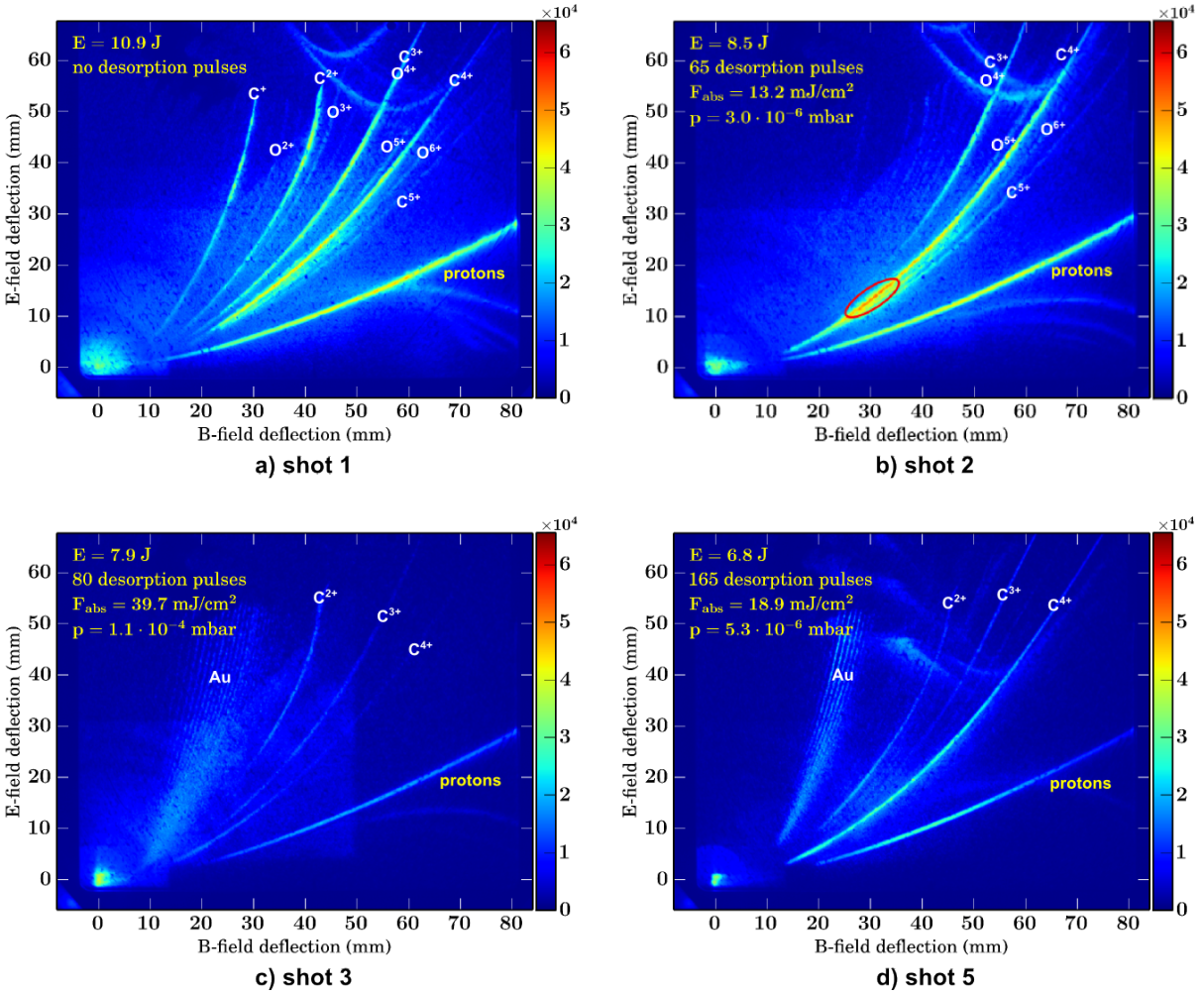


**Figure 5.9:** Thomson parabola spectra of shots on 10 µm thick Au-foils with different desorption pulse configurations and target chamber pressures. The signal intensity scale in MCP counts is given on the right. In a) a reference shot without any desorption pulses is shown. Besides an intense proton signal carbon ions up to charge state 5+ and oxygen ions are present. In b) at a laser fluence of the desorption beam of $F_{abs} = 13.2\,mJ/cm^2$, ions with low charge states vanish completely while $C^{4+}$ has a higher maximum energy and shows an enhanced signal between 0.18 MeV/u and 0.35 MeV/u marked by the red ellipse. Increasing the fluence to $F_{abs} = 39.7\,mJ/cm^2$, like in c), or the number of desorption pulses to 165 at $F_{abs} = 18.9\,mJ/cm^2$, like in d), the proton signal and their maximum energy clearly decrease as compared to a) and gold ions are accelerated.

becomes also visible in the energy spectrum of $C^{4+}$ in Figure 5.11, red curve.

These features change even more for an increased desorption process with an absorbed laser fluence $F_{abs} \geq 18.9\,mJ/cm^2$ and with more desorption pulses. Like both the Thomson parabola spectra of shot 3 and shot 5, Figures 5.9 c) and d), and the proton spectra in Figure 5.10 demonstrate, the proton signal intensity on the MCP decreased by about one order of magnitude compared to shot 1. A substantial reduction of the proton maximum energy by at least a factor of two was noted, too. Less but higher energetic desorption pulses like in shot 3 were more effective for getting rid of the hydrogen contamination than more desorption pulses with lower pulse energy as in shot 5.
The influence of the enhanced desorption process on the carbon ions differs for their individual charge states. Like Figure 5.11 shows, for $C^{3+}$ a similar behavior as for the protons is recorded.

| shot no. | # desorp. pulses | $F_{abs}$ [mJ/cm$^2$] | $E_{des}$ [mJ] | $E_{CPA}$ [J] | $p$ [mbar] | ions | $E_{kin}^{max}$ [MeV/u] | $\Delta\Phi_{ion}$ [MV] |
|---|---|---|---|---|---|---|---|---|
| shot 1 (reference shot) | 0 | | | 10.9 | | p | 12.00±1.50 | 12.00±1.50 |
| | | | | | | $C^{5+}$ | 0.38±0.04 | 0.90±0.10 |
| | | | | | | $C^{4+}$ | 0.58±0.08 | 1.75±0.25 |
| | | | | | | $C^{3+}$ | 0.35±0.04 | 1.40±0.17 |
| | | | | | | $C^{2+}$ | 0.21±0.02 | 1.25±0.10 |
| | | | | | | $C^{+}$ | 0.13±0.01 | 1.50±0.10 |
| shot 2 | 65 (rear side) | 13.2 | 2.1 | 8.5 | $3\times10^{-6}$ | p | 12.00±1.50 | 12.00±1.50 |
| | | | | | | $C^{5+}$ | 0.45±0.02 | 1.10±0.04 |
| | | | | | | $C^{4+}$ | 1.17±0.08 | 3.50±0.25 |
| | | | | | | $C^{3+}$ | 0.15±0.03 | 0.60±0.10 |
| shot 3 | 80 (rear side) | 39.7 | 2.3 | 7.9 | $1.1\times10^{-4}$ | p | 3.40±0.40 | 3.40±0.40 |
| | | | | | | $C^{4+}$ | 0.96±0.08 | 2.88±0.25 |
| | | | | | | $C^{3+}$ | 0.18±0.03 | 0.70±0.10 |
| | | | | | | $C^{2+}$ | 0.06±0.01 | 0.35±0.06 |
| shot 4 | 100 (rear and front side) | 18.9 | 1.0 | 5.6 | $3.1\times10^{-5}$ | p | 3.20±0.30 | 3.20±0.30 |
| | | | | | | $C^{4+}$ | 0.67±0.08 | 2.00±0.25 |
| | | | | | | $C^{3+}$ | 0.12±0.02 | 0.47±0.07 |
| shot 5 | 165 (rear and front side) | 18.9 | 1.0 | 6.8 | $5.3\times10^{-6}$ | p | 4.50±0.50 | 4.50±0.50 |
| | | | | | | $C^{4+}$ | 1.10±0.13 | 3.30±0.39 |
| | | | | | | $C^{3+}$ | 0.17±0.01 | 0.68±0.05 |
| | | | | | | $C^{2+}$ | 0.13±0.01 | 0.80±0.06 |

**Table 5.1:** Overview of all important parameters of the discussed laser desorption shots and of the reference shot (no cleaning) on 10 µm Au foils. The quantities listed here are the absorbed laser fluence $F_{abs}$ and the energy $E_{des}$ of the desorption pulses, the laser energy $E_{CPA}$ of the main pulse and the target chamber pressure $p$. Included are also the analysed results from the Thomson parabola ion traces regarding the maximum ion kinetic energies $E_i^{max}$ and a calculated estimate for the maximum potential difference $\Delta\Phi_{ion} = E_i^{max}/Ze$ the fastest ions should have experienced by the quasistatic electric field [1].

Both the particle intensity and the maximum energy of $C^{3+}$ drop compared to shot 1.
Exactly the opposite is observed for $C^{4+}$. The maximum energy of $C^{4+}$ is shifted to higher energies and an increased particle intensity in the higher energetic region is noted in comparison to shot 1. Like Figure 5.11 illustrates, the total particle intensity of $C^{4+}$, however, was strongly affected by the respective cleaning performance. With increasing fluence of the desorption laser beam (shot 3) and/or low CPA pulse energy (shot 4) the $C^{4+}$-ion flux diminished, especially for energies below 0.5 MeV/u. The opposite happened for lower fluences of the desorption laser beam and/or higher CPA pulse energy (shot 5 and shot 2) showing an increased particle intensity in that region.
The parabola traces of the carbon ions with low charge states, i.e. $C^{+}$ and $C^{2+}$, vanished almost completely on the MCP as a consequence of the laser desorption.

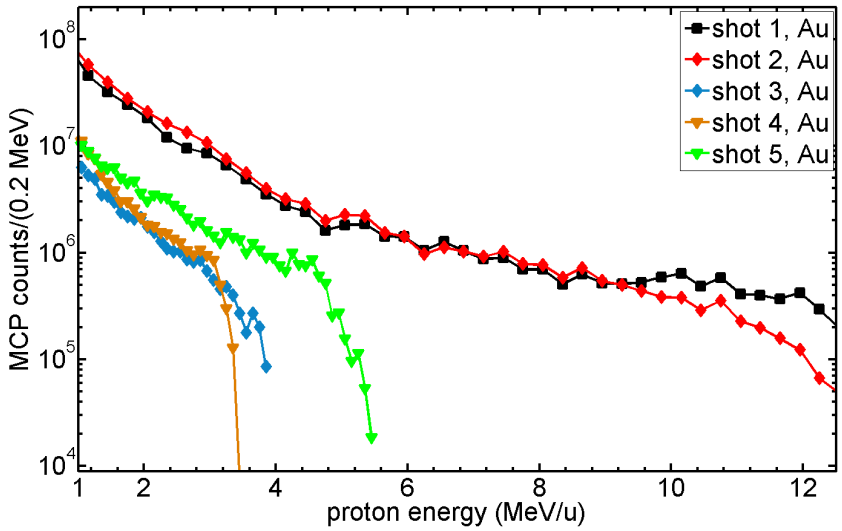


**Figure 5.10:** Comparison of proton spectra resulting from shots on gold foils. The shot details are given in Table 5.1. The proton intensity definitely decreased for shots with preceding desorption pulses of $F_{abs} \geq 18.9\,W/cm^2$.

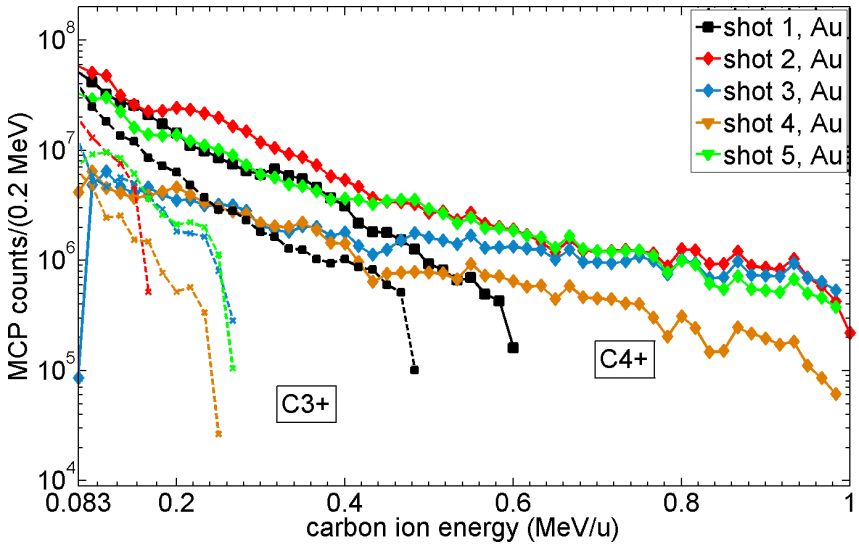


**Figure 5.11:** Comparison of all $C^{4+}$ (solid curves) and $C^{3+}$ (dashed curves) spectra obtained from the discussed shots on Au foils, see Table 5.1. While the maximum energy of $C^{4+}$ increases when laser desorption is applied, it decreases in case of $C^{3+}$ compared to the reference shot (shot 1).

For each shot listed in Table 5.1, Figure 5.12 illustrates the fraction of the individual carbon ion charge states to the total carbon ion yield, integrated in energy. The fraction of accelerated $C^{4+}$-ions relatively increases due to the laser desorption while the relative amount of the carbon ions with charge states lower than 4+ decreases or even is zero. This feature was most distinctive in shot 2 with an intermediate fluence of the desorption laser. The slight deviation of shot 3 from this trend is probably explainable by the very low general carbon ion signal in this shot. The ratio of the total carbon ion yield, i.e. summed over all charge states, of the shots with applied laser desorption to the reference shot is indicated by the black stars in Figure 5.12. They mark the general reduction of accelerated carbon ions in the shots of preceded laser desorption with $F_{abs} \geq 18.9\,mJ/cm^2$ (shots 3, 4, 5), indicating that the carbon density on the target surface was diminished by the desorption.

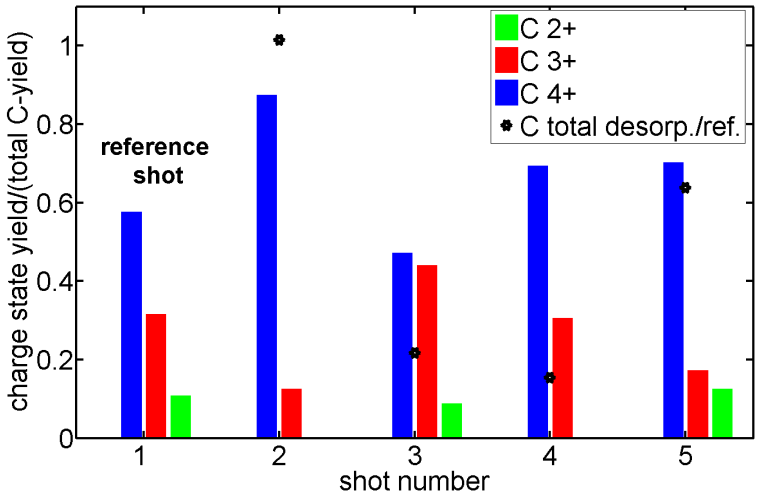


**Figure 5.12:** Fraction of the $C^{4+}$-, $C^{3+}$- and $C^{2+}$-ion yields to the total carbon ion yield of each shot (see Table 5.1), integrated from 0.083 MeV/u to 1 MeV/u. The black stars show the total carbon ion yield ratio of the individual shots with desorption to the reference shot (shot 1) [1].

Apart from the discussed modifications in the proton and carbon ion spectra, the intensified cleaning process led also to the acceleration of gold ions. Their charge states are ranging from $Au^{3+}$ to $Au^{20+}$ in shot 3 and from $Au^{8+}$ to $Au^{15+}$ in shot 5 [1].

Although the integrated laser fluence absorbed by the gold foils was the same, certain differences were observed when comparing the irradiation of both target surfaces at a laser fluence of $F_{abs} = 18.9\,mJ/cm^2$ with 165 desorption pulses (shot 5) to the irradiation of only the target rear surface at $F_{abs} = 39.7\,mJ/cm^2$ with 80 desorption pulses (shot 3). Irradiating only the target rear surface (shot 3) showed the following features: Firstly, the MCP registered a considerably smaller proton signal, in particular for proton energies above 3 MeV/u, like Figure 5.10 shows. Secondly, as demonstrated in Figure 5.11, a reduced $C^{4+}$ signal was recorded, especially for ion energies below 0.5 MeV/u. Furthermore, Figure 5.12 demonstrates that the relative total amount of accelerated carbon ions was a factor of two smaller in shot 3 compared to shot 5. And thirdly, a larger number of parabola traces resulting from gold ions were registered which, however, exhibited a slightly lower particle intensity. Additionally, the target chamber pressure was more than one order of magnitude larger than in shot 5, which corresponds to an increased readsorption rate of residual gas molecules by a factor of at least ten between the individual desorption pulses according to equation 4.12. This faster readsorption on the target surface would suggest an enhanced acceleration of adsorbate ions like protons and carbon ions, but the opposite was the case.
All these observations imply that the target surface had to be cleaned more efficiently from its contaminants, i.e. the contamination layer became thinner, when less desorption pulses at a higher laser fluence irradiated the target rear surface. Due to the thinner contamination layer the electric field could penetrate deeper into the gold foil. Therefore, a broader range of charge states was recorded for gold ions compared to shot 5. Additionally, as more and more desorption pulses continue to irradiate the target surface, a net heat transfer to the target surface leading to hydrogen diffusion cannot be disregarded anymore, like already discussed in section 4.5.3.

### 5.4.2 Copper foils

Laser desorption of copper foil targets confirms the results obtained from gold foils. As the Thomson parabola spectrum in Figure 5.13 demonstrates, the irradiation of both target surfaces with 100 desorption pulses of $F_{abs} = 18.9\,mJ/cm^2$ led to the complete absence of carbon and oxygen ions with low charge states and to reduced signals of those with higher charge states. Even the intense signals of $C^{4+}$ ions disappeared. Like already observed for shots on gold foils, the maximum energy of protons decreased to half of its value and their intensity was reduced by one order of magnitude compared to shot 1 (see Figure 5.16 in section 5.4.4). An abundant spectrum of copper lines was evident on the Thomson parabola which was not present in shots without laser desorption. The various Cu-ion traces ranged from $Cu^{2+}$ up to $Cu^{14+}$. On a closer look, the two copper isotopes $^{63}Cu$ and $^{65}Cu$ could even be discerned. These results show that several monolayers of contaminants have been removed from the target surface and the TNSA field was sufficiently high to accelerate copper ions [1].

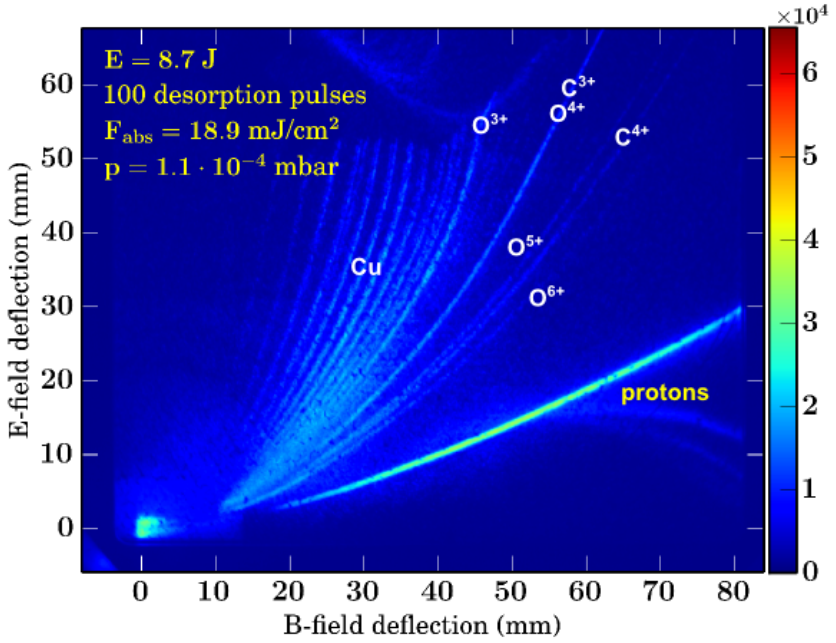


**Figure 5.13:** Thomson parabola spectrum of a shot on a 10 µm thick Cu foil with a CPA pulse energy of 8.7 J, preceded by 100 desorption pulses irradiating both target surfaces.

### 5.4.3 Aluminum foils

Very dominant effects of the fs-laser desorption were observed when using 11 µm thin aluminum targets. The Thomson parabola spectrum in Figure 5.14 shows that numerous intense oxygen and aluminum ion traces of various charge states were recorded. The high oxidation potential of aluminum in comparison to gold or copper leads to the formation of aluminum oxide ($Al_2O_3$) on the target surface. Therefore, oxygen constitutes the predominant surface contamination as the ERDA run in section 3.1 confirms. Besides the oxygen ions, abundant aluminum ion traces were visible which reach from $Al^+$ to $Al^{10+}$ while the proton signal shows the common feature of a decrease in both intensity and maximum energy (see Figure 5.16 in the following section). Figure 5.15 demonstrates the ion energy spectra of almost all oxygen ions and most of the aluminum ions illustrating that they are continuously accelerated to higher

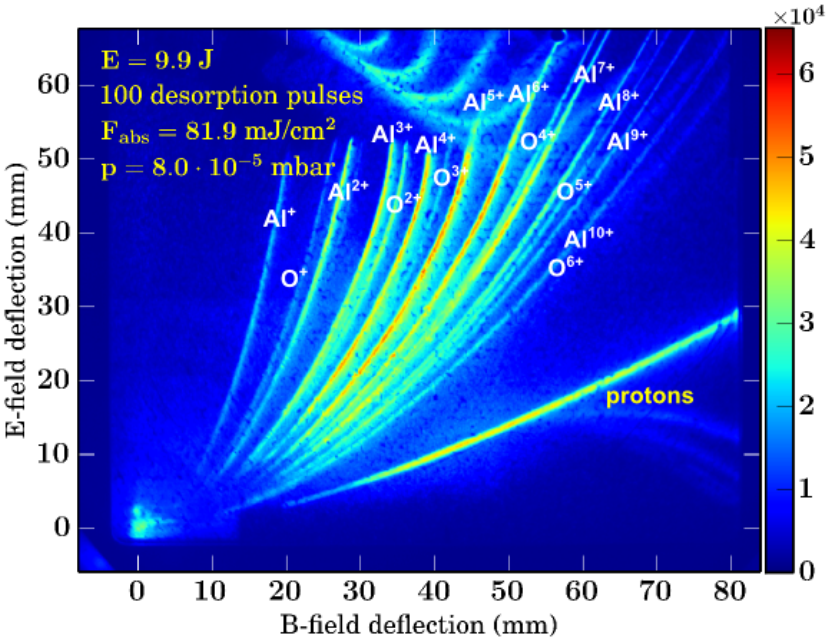


**Figure 5.14:** Thomson parabola spectrum of a shot on a 11 µm thick Al foil with a CPA pulse energy of 9.9 J preceded by 100 desorption pulses irradiating both target surfaces.

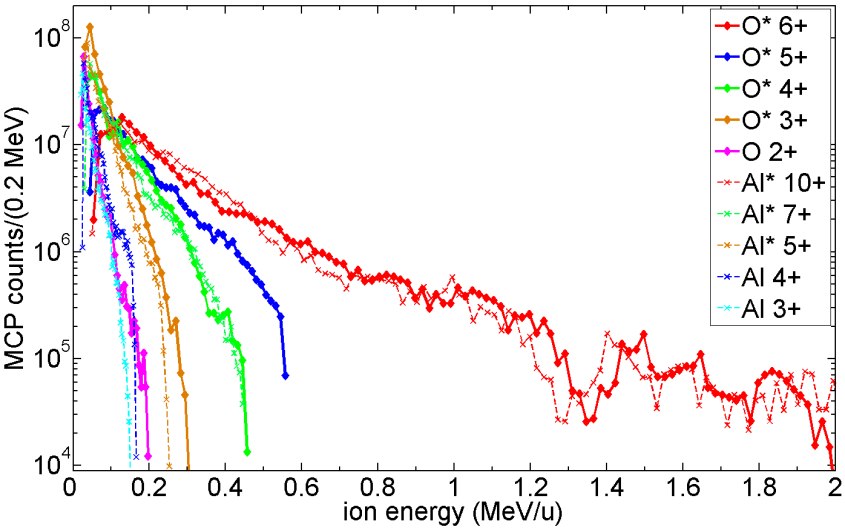


**Figure 5.15:** Comparison of the accelerated oxygen and aluminum ions obtained from a shot on a 11 µm thick Al foil. The ion traces of $O^{2+}$, $Al^{3+}$ and $Al^{4+}$ could be analyzed individually while the other ion traces could only be analyzed as a summed particle signal due to superpositions. $O^{6+}$ superposed with $Al^{10+}$ were the ions exposed to the highest electric field potential with an acceleration of up to 1.94 MeV/u.

maximum energies with increasing charge states. The electron binding energies of oxygen in the K shell are more than 10 times higher than in the L shell. Therefore, $O^{7+}$ and $O^{8+}$ could not be accelerated with the applied CPA pulse energies. The same argument is valid for aluminum ions. Higher charge states than $Al^{11+}$ leaving a too weak trace to be analyzed on the phosphor screen were also not available for the TNSA. Because of a very similar charge-to-mass ratio we got superpositions of aluminum ion traces of charge state $Al^{5+}$ and higher with oxygen ion traces of charge state $O^{3+}$ and higher. This renders a careful analysis of their single particle intensities difficult and led to overestimated particle signals. Those ion traces affected by super-

positions remain nevertheless comparable to each other and the maximum energy of the ions with a fixed charge-to-mass ratio could be determined as well. They fit in the common picture of the laser desorption results that the acceleration of ions from the target material considerably benefits from the reduced hydrogen content on the target surface [1].

### 5.4.4 Comparison of target materials

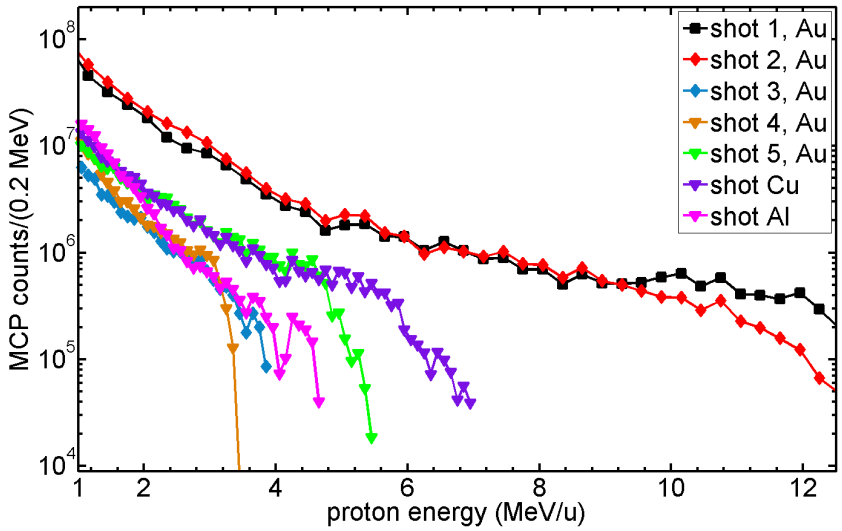


**Figure 5.16:** Comparison of all proton spectra discussed in the text. A definite decrease in proton intensity was noted for shots with preceding desorption pulses of $F_{abs} \geq 18.9\,W/cm^2$.

The application of fs-laser desorption prior to the TNSA led to the following common observations for the three investigated target materials gold, copper and aluminum. The target surface could be cleaned efficiently from the adsorbed gas contaminants. Especially the hydrogen content on the target surface was reduced considerably which becomes evident when comparing the resulting proton energy spectra with the reference shot (shot 1). This comparison is presented in Figure 5.16, which, in addition to Figure 5.10, contains also the recorded proton energy spectra from the discussed shots on a copper as well as an aluminum foil. Apart from shot 2 (see section 5.4.1) all the proton energy spectra resulting from the TNSA with preceded laser desorption show both a strongly reduced proton cutoff energy and a clearly decreased particle intensity of about one order of magnitude compared to the reference shot. The diminished contamination layer thickness provided a deeper penetration of the electric field into the respective target material. Like the Thomson parabola spectra presented in the last sections illustrate, atoms of the target material were ionized and metal ions of various charge states were accelerated in case of all the three chosen target materials. Due to the more pronounced oxide layer on aluminum compared to gold and copper the measurements of the TNSA from aluminum foils additionally showed a broad range of oxygen ions with charge states up to $O^{6+}$.

### 5.4.5 Numerical results

The experimental measurements have demonstrated that the proton cut-off energies decrease as the absorbed fluence of the desorption laser beam and the number of the desorption pulses increase. For example, the maximum proton energy of an uncleaned target surface resulted

in 12 MeV. In contrast, during the shot on an aluminum surface, from which the contaminants were removed by 100 desorption pulses at an absorbed fluence of 81.9 mJ/cm$^2$, protons were accelerated only to a maximum energy of 4.6 MeV.
Figure 5.17 shows the different measured proton cut-off energies, which are marked by the blue squares, in dependence of the CPA laser pulse energy. They correspond to differing applied laser fluences and to a different number of desorption pulses and are labeled according to the used target material as well as to the respective shot number in case of gold foils as described in section 5.4.1. These experimental values are compared to the theoretical values of the proton cut-off energies, which are indicated by the black circles and obtained from the isothermal plasma expansion model introduced by Mora [40] and discussed in section 2.5.1. The ion acceleration time was set to $\tau_{\mathrm{acc}} = 1.3\,\tau_L \approx 120$ fs with the laser pulse duration $\tau_L = 90$ fs.
This comparison demonstrates that the decrease of the experimentally measured proton cut-off energies cannot fully be explained by a reduced CPA laser pulse energy. For example, the experimental data point at 5.6 J laser energy lies 37 % below the value evaluated from Mora's plasma expansion model. Almost all the shots with preceded laser desorption demonstrate the same trend of strongly falling below the theoretical values of Mora's plasma expansion model. Only shot 2 (Table 5.1) at 8.5 J laser energy deviates from this trend. Here, the moderate laser desorption induced only a minor removal of adsorbates. However, this caused a more efficient proton acceleration since the remaining protons in the contamination layer experienced a higher electric field due to reduced screening effects. On the contrary, the two reference shots, symboled by a blue circle around the data point, could reproduce these theoretical values very well. Herein, the shot labeled with Au* marks a shot on a gold foil preceded by one single desorption pulse which, however, did not alter the resulting ion spectra to any observable extent. Thus, this shot can be regarded as a reference shot. It becomes evident, that the fs-laser desorption has induced a cleaning effect from the target rear surface, which implies both a reduced total number of accelerated protons and a decreased cut-off energy of protons, as Figure 5.16 shows.

The influence of the contamination layer on the carbon ion acceleration was simulated by R. Nuter and J. Rolle using an advanced version of the two-dimensional (2D) PIC code named *Calder* [201] incorporating the field ionization model. Two different approaches to model the laser-induced carbon ion acceleration were chosen. In both cases the target was considered as

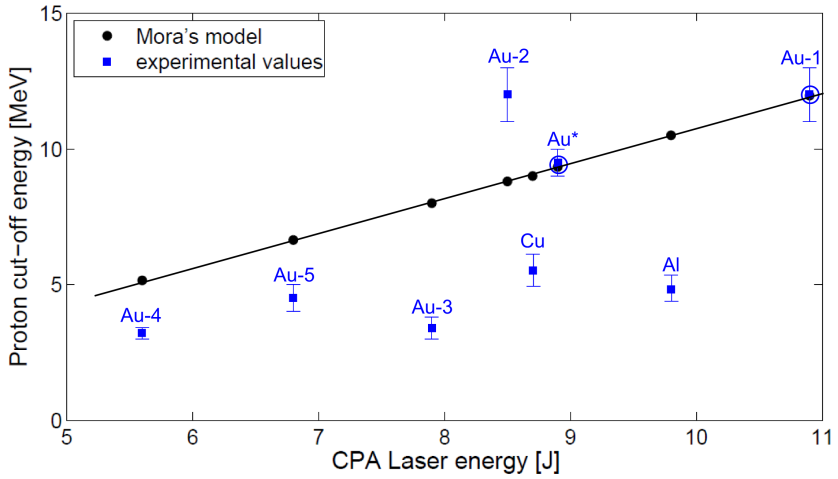


**Figure 5.17:** Proton cut-off energies in dependence of the CPA laser pulse intensity obtained from the experiment (blue squares) and from Mora's plasma expansion model [40] (black circles). Additional blue circles around the data points denote the shots without induced fs-laser desorption.

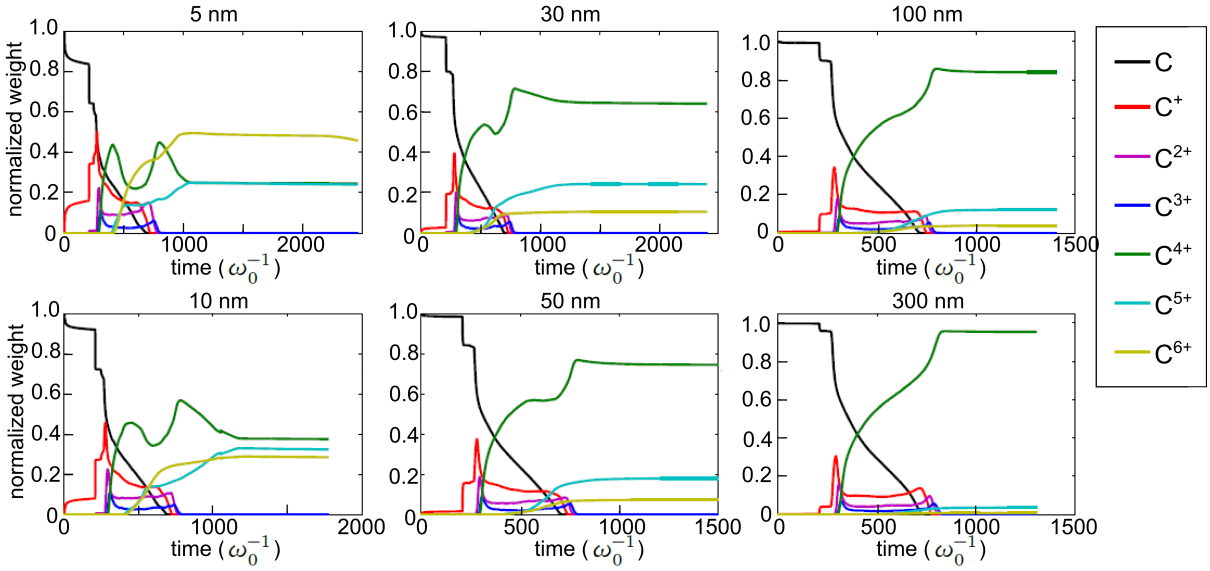


**Figure 5.18:** Simulated carbon ion population over time in units of the inverse laser frequency $\omega_0^{-1}$ for different contamination layer thicknesses.

a three layer plasma composed of a 10 nm proton layer on the target front surface, followed by 500 nm $Au^+$ and concluded by a mixture of hydrogen and carbon atoms on the target rear surface. Due to numerical constraints a simulation of a 10 µm thick target foil was not possible. The performed simulations therefore focused on the study of a qualitative agreement with the experimental data. The mesh sizes were chosen to be $\Delta x = 5$ nm and $\Delta y = 10$ nm and the temporal resolution was $\Delta t = 0.011$ fs. This ensured a numerical heating, i.e. the nonphysical increase of kinetic energy[4] violating the energy conservation due to the discretization of the physical model [202], of less than 5 % of the laser energy [201]. The simulated CPA beam had a pulse duration of 90 fs, a focal spot diameter of 15 µm and a laser intensity of $4.5 \times 10^{19}$ W/cm$^2$. The laser irradiated the target under 34° incidence angle, thus, reproducing the experimental conditions.

In the first numeric approach, the thickness of the hydrocarbon layer was varied while the areal density as well as the ratio of hydrogen to carbon ions, taken from the ERDA measurements of copper (section 3.1), was held constant. Figure 5.18 shows the temporal evolution of the resulting relative carbon ion fractions for the different contamination layer thicknesses of 5 nm, 10 nm, 30 nm, 50 nm, 100 nm and 300 nm, respectively. The total carbon ion yield is normalized to one and the time scale is given in units of the inverse laser frequency $\omega_0^{-1} = 0.42$ fs. The black curve shows the decrease of the carbon content on the target surface with time due to the carbon ion acceleration. In the very first stage of the laser-matter interaction carbon ions of low charge states are preferentially accelerated. In all the six simulations $C^+$ shows the strongest contribution in this early phase. As time proceeds, the electric sheath field on the target rear side gradually increases and more and more carbon ions of higher charge states become accelerated. $C^{4+}$ rises while the carbon ions of lower charge states than $C^{4+}$ drop. The onset of the acceleration of $C^{6+}$ leads to a decrease of the $C^{4+}$-fraction and also slightly of $C^{5+}$. When the electric sheath field reaches its maximum value at about $750/\omega_0$, the contribution of the low charge states, i.e. $C^+$, $C^{2+}$ and $C^{3+}$, drops to zero. As a consequence, the fraction of $C^{4+}$ rises again as it occurs also for $C^{5+}$ and $C^{6+}$. The dominating fraction of carbon ions con-

[4] Nonphysical fluctuations in the electric field result from the charge assignment of the simulated particles to the adjacent grid points.

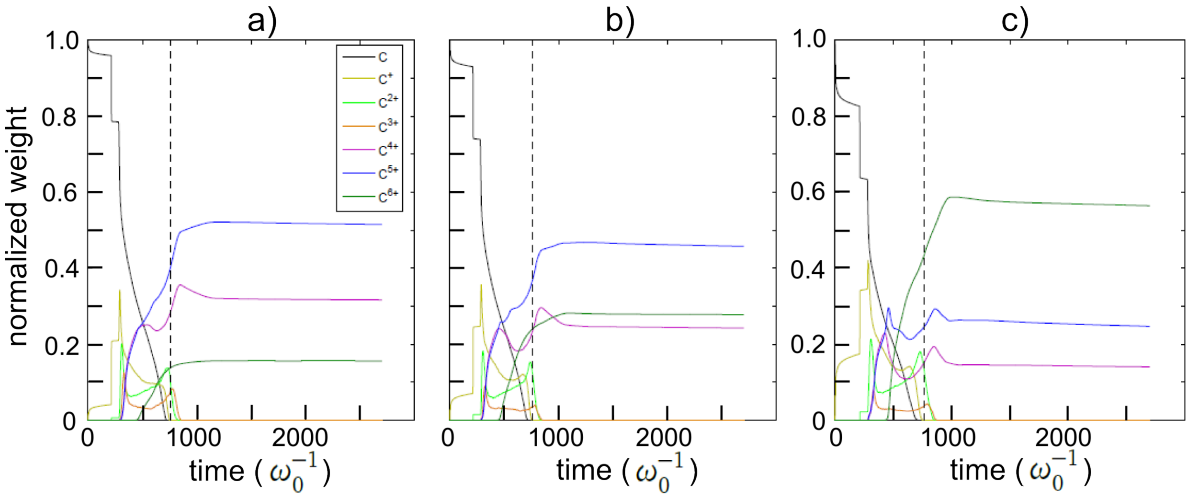


**Figure 5.19:** Simulated carbon ion population over time in units of the inverse laser frequency $\omega_0^{-1}$ for a hydrogen to carbon atom ratio of 0.21 and three different areal densities listed in Table 5.2. The dashed line represents the time at which the electron energy is maximal.

sists of $C^{4+}$ and the contribution of $C^{5+}$ and $C^{6+}$ continuously decreases for contamination layer thicknesses of 10 nm and larger. This feature reveals the decrease of the electrostatic field seen by the carbon ions as the thickness of the contamination layer is increased. This is qualitatively in consistence with the measured data in subsections 5.4.1 to 5.4.4. However, a contribution of $C^{5+}$ was merely visible in the data and $C^{6+}$ could not be accelerated at all requiring that the electric sheath field was larger than 7 TV/m which obviously could not be achieved.

In the second numeric approach, a constant thickness of 10 nm was assumed for the hydrocarbon layer. The ratio of hydrogen to carbon atoms was reduced to a value of 0.21 in order to take into account that the laser desorption modifies the composition of the contamination layer. The three different considered areal densities of hydrogen and carbon atoms on the rear surface are given in Table 5.2. Figure 5.19 shows the resulting temporal evolution of the laser-accelerated carbon ions. A similar picture as for the first simulation scenario arises. In all the three considered cases, the lowest carbon ion charge states, i.e. $C^{+}$, $C^{2+}$, $C^{3+}$, are rapidly created at the early acceleration phase when the electric field is still continuously rising. As the areal density is decreased, thus, going from a) over b) to c) in Figure 5.19, the $C^{6+}$ population is increased while the fraction of $C^{4+}$, and also even of $C^{5+}$, is reduced. Whereas in case a) the fraction of $C^{6+}$ results in 15 %, its contribution is already risen to about 60 % in case c). The carbon ions experience a higher electric field since this is less shielded by hydrogen atoms due to their reduced areal density.

As already mentioned above, $C^{6+}$ was not observed in the experiment. But the obtained simulation results are qualitatively in agreement with the experimental data presented in the previous

| Sample | a) | b) | c) |
|---|---|---|---|
| H | $1.5\times10^{16}\,\mathrm{cm}^{-2}$ | $7.5\times10^{15}\,\mathrm{cm}^{-2}$ | $1.9\times10^{15}\,\mathrm{cm}^{-2}$ |
| C | $7.0\times10^{16}\,\mathrm{cm}^{-2}$ | $3.5\times10^{16}\,\mathrm{cm}^{-2}$ | $8.7\times10^{15}\,\mathrm{cm}^{-2}$ |

**Table 5.2:** Areal densities of hydrogen and carbon atoms used for the second simulated scenario.

subsections showing an increase of the carbon ion charge state as the target is better cleaned. A quantitative agreement could not be obtained because the simulated target is 20 times thinner than the experimentally used one.

## 5.5 Long-term laser desorption

In a second experimental campaign at the Callisto laser with the experimental setup given in Figure 5.5, the study of influencing TNSA ions by laser-induced desorption was continued, but with the additional goal of analyzing how deep the TNSA electric field penetrates into the target material. Therefore, a special target design was constructed consisting of a 5 µm thick gold foil coated with nickel of the thicknesses 10 nm, 20 nm, 30 nm, 40 nm and 50 nm, respectively, on one surface, which was dedicated to be the target rear surface. These nickel layers were created by sputter deposition[5] in an argon atmosphere, performed at the target laboratory of GSI Helmholtzzentrum für Schwerionenforschung GmbH.

The fs-laser desorption working at an incoming fluence of $F_{\text{in}} = (0.5 \pm 0.1)$ J/cm$^2$ should in this campaign provide a complete cleaning of the target rear surface from any contamination. The target surface coated with nickel was therefore irradiated over a period of time between 15 minutes and 45 minutes, comparable to the desorption experiment described in section 4.3. During the TNSA the location of the atoms in the target determines, to what extent the accelerating field potential is experienced by them. Thus, their position determines their degree of ionization and their subsequent acceleration. The effective potential difference in the quasistatic electric field can be calculated from the maximum ion energies. Together with the knowledge of the particle position a rough estimate of the TNSA field can be obtained. The depth information should thereby be provided by the usage of the thin nickel layers of known thicknesses. For example, if gold ions were recorded in case of the TNSA from a gold foil coated with a 10 nm thick nickel layer and, assuming similar laser parameters, no accelerated gold ions were observed for the usage of a nickel layer with a thickness of 20 nm, one could conclude that the electric field strength at a depth of 20 nm was no longer sufficient for the ionization of gold atoms and for their subsequent acceleration.

Unfortunately, the whole experimental campaign suffered from severe laser problems which made a thorough and reliable data acquisition as well as data analysis impossible. Only data for targets with a 10 nm and a 20 nm thick nickel layer on top of the gold foil exist. For most of the shots a proton trace with a maximum energy of about 3 MeV averaged over all shots could be obtained. For few shots an additional ion trace of $C^{4+}$, and in three shots even slightly of $C^{3+}$, was visible on the IP.
In spite of the laser problems a general observation was made for the long-term laser desorption. A relative comparison of some shot results obtained at similar CPA laser energies demonstrated, that the ion acceleration of protons and $C^{4+}$ was enhanced for shots with an increased period of time of laser desorption. This is illustrated in Figure 5.20. The left image, a), presents the ion traces of a shot without laser desorption as they were recorded on an IP. The ion signal is the weakest one compared to the other two images, which display shots with applied laser desorption for a period of time of 35 minutes in b) and 45 minutes in c). The Thomson parabola trace of protons in a) is similar to the proton trace in b). In both cases a maximum proton energy

[5] In this process, a DC voltage is applied between a target consisting of the coating material and a substrate, which should be coated. Positive argon ions from the generated argon plasma are accelerated to the target of the coating material and knock out atoms. These move away from the target and deposit on the substrate, on which they build a thin film.

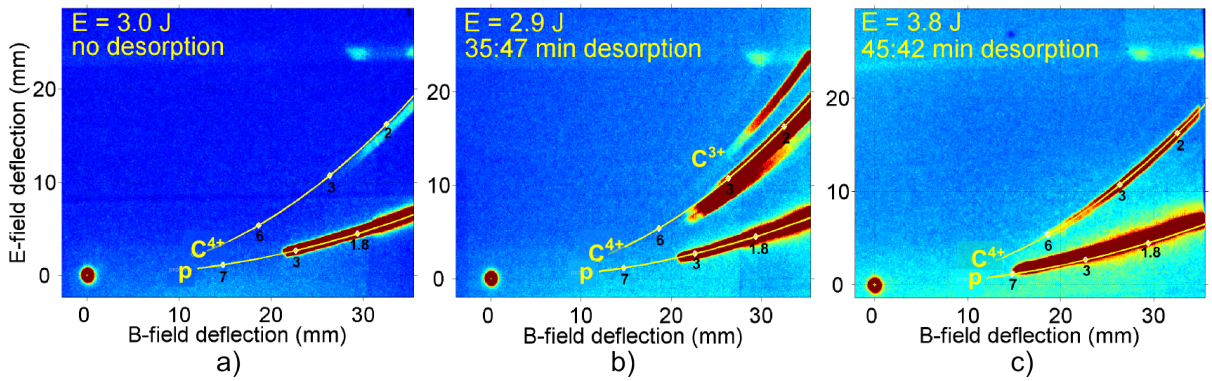


**Figure 5.20:** Ion traces of protons (p) and $C^{4+}$ as well as $C^{3+}$ recorded on an IP which result from shots on 5 µm thick gold foils coated with a 10 nm thick nickel layer. In a) a proton trace but almost no carbon ions were recorded (no laser desorption) while, in addition to the proton trace, a strong $C^{4+}$ as well as a $C^{3+}$ signal was visible in b) (laser desorption for 35 minutes) and in c) even a higher cut-off energy was recorded for $C^{4+}$ (laser desorption for 45 minutes). The numbers at the marked positions of the fitted parabola trace (yellow line) denote the respective ion energies in MeV.

of slightly above 3 MeV was recorded. But the carbon ion signal in b) is significantly enhanced when the target rear surface was irradiated with desorption pulses. The maximum ion energy of $C^{4+}$ increased almost by a factor of two from 2.4 MeV in a) to 4.2 MeV in b). Not only the $C^{4+}$ ion signal is strongly increased, but also a clear signal of $C^{3+}$ ions is visible. As demonstrated in c), raising the irradiation time of laser desorption while letting all other laser parameters of the desorption beam unmodified results in a definite increase of the maximum energies of both protons and $C^{4+}$ ions to almost 7 MeV and 6 MeV, respectively. This behavior contradicts to the experimental results of short-term laser desorption described in the previous section 5.4.

## 5.6 Discussion

### 5.6.1 Short-term laser desorption

The surface structure on the target rear side which acts as the ion source determines the characteristic of the TNSA. Ions with highest charge-to-mass ratio and with an exceedable ionization potential are preferably generated and accelerated. At the beginning of the acceleration process, the TNSA electric field energy is therefore transferred into the acceleration of protons, followed by $C^{5+}$ and $C^{4+}$ according to their density distribution on the target rear side. The electric field becomes screened for atoms which are located deeper in the target foil. As illustrated in Figure 5.21, left sketch, these atoms experience a lower electric field which, however, is strong enough to further ionize them to lower charge states and to accelerate these ions. In case of TNSA without laser desorption, like the presented reference shot in section 5.4.1, the acceleration of $C^{+}$, $C^{2+}$, $O^{+}$, $O^{2+}$ and $O^{3+}$ is therefore observed. Gold, copper or aluminum ions are not accelerated since they experience a too low electric field.

The desorption pulses modify the target surface structure by successively removing the adsorbed contaminants. The comparison of shot 3 to shot 5 on gold foils illustrates that higher fluences of the desorption pulses were more effective than a higher number of pulses. Apart from the re-adsorption of contaminants between the individual laser pulses, a net heat transfer to the target surface sets in as more and more desorption pulses continue to irradiate the target.

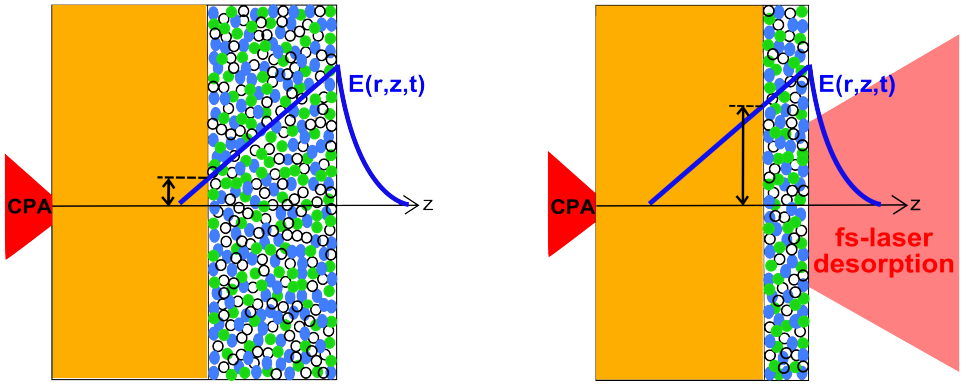


**Figure 5.21:** CHO contamination layer on the target surface (not true to scale) and the TNSA field E(r,z,t) reaching into the foil. Without desorption (left) the electric field gets strongly screened by the contaminants. Due to the thinner contamination layer in case of fs-laser desorption (right), metal atoms from the target foil experience a sufficiently strong electric field to get field-ionized and accelerated.

The efficiency of desorbing contaminants drops and a saturation effect sets in between 150 and 200 desorption pulses. Although these two circumstances decelerate the desorption process, the net effect results in a stepwise decrease of the contamination layer thickness when remaining below that saturation limit. Like sketched in the right image of Figure 5.21, the thinner contamination layer leads to less screening effects of the TNSA electric field by contaminants. Due to the reduced proton density on the target rear side a larger accelerating field is available for ionizing carbon and oxygen atoms to higher charge states and for accelerating them to higher energies. This was the case for $C^{4+}$ in the presented shot results on gold foils with preceding laser desorption. At a moderate fluence of the desorption laser beam and an intermediate number of pulses the contamination layer decreases modestly and screening effects still play a major role. Like it was observed in shot 2, Figure 5.9 b), the remaining field potential did not suffice to ionize gold atoms but an enhanced acceleration of $C^{4+}$ occurred. The observed reduction or even absence of the carbon and oxygen ions with low charge states results from the fact that the residual field potential still suffices for the ionization of carbon to higher charge states, in the present case $C^{4+}$, and for their acceleration to higher energies. With increasing fluence of the desorption laser beam the contamination layer gets thinner and thinner and screening effects by contaminants become less important for the TNSA of metal ions. When there is no carbon and oxygen left anymore on the target surface and the remaining field potential is still sufficiently high, it ionizes gold and copper atoms and accelerates these ions. Their maximum charge state is determined by the strength of the remaining electric field potential. Those gold ions are recorded in shot 3 and shot 5, Figures 5.9 c) and d), and the respective copper ions in Figure 5.13. In case of aluminum foils, both strong aluminum and oxygen ions are found (Figure 5.14). This is due to the thicker oxide layer on aluminum than on copper or gold foils.

In the presented shot on aluminum in subsection 5.4.3 the superposed ion species $O^{6+}$ and $Al^{10+}$ experienced an acceleration up to $E_{\mathrm{kin}}^{\mathrm{max}} = (1.94 \pm 0.12)\,\mathrm{MeV/u}$. Such maximum kinetic energy can be reached by these ions, assuming a passed potential difference in a quasistatic electric sheath of

$$\Delta\Phi = \frac{E_{\mathrm{kin}}^{\mathrm{max}} \times A}{eZ} = \frac{E_{\mathrm{kin}}^{\mathrm{max}}}{e(q/m)} = (5.17 \pm 0.27)\,\mathrm{MV}, \tag{5.5}$$

where $E_{\mathrm{kin}}^{\mathrm{max}}$ is given in units of MeV/u, $A$ is the ion's mass number and $Z$ its charge state. It is the highest field potential experienced by ions in that shot and exceeds also the field potential

experienced by protons, which is $\Delta\Phi = (4.6 \pm 0.2)$ MV. This indicates that the registrated protons have to originate from hydrogen stored in the bulk on interstitials of the atomic lattice and not from a hydrogen layer accumulated on the target rear surface.

Earlier experiments on heavy ion induced desorption [203] have shown that hydrogen diffuses from the bulk to the surface and therefore could not be removed completely. Thus, the ion induced desorption is mainly a surface effect. Similar observations were made in case of the fs-laser desorption. The adsorbed gases on the target surface could be removed quite well, which is illustrated by the acceleration of aluminum ions of several charge states, but also by a number of gold and copper ion traces in the respective discussed shots. But neither the oxide layer on top of copper and aluminum foils as well as some carbon remnants on gold foils nor the hydrogen stored in the bulk of these materials could be removed completely. This led to the acceleration of oxygen and carbon ions as well as of protons.

In ns- to ps-laser ablation [133] carbon and oxygen ions with low charge states ($C^+$, $C^{2+}$, $O^+$, $O^{2+}$) are still present, which is due to a still thick enough contamination layer or due to the longer laser pulse interacting with the ablated material. Cleaning techniques as resistive heating [48] dehydrogenize the target completely with the consequence that no protons were observed at all. In contrast, the data presented here show, that a stepwise increase of the fluence of the desorption laser provides a consecutive decrease of the contamination layer. Thus, this new cleaning technique allows to scan through the contamination layer investigating different stages of the cleaning process. No other cleaning technique could provide this possibility, so far.

### 5.6.2 Long-term laser desorption

The irradiation of the target surface with fs-laser pulses over a long period of time, like described in section 5.5, involves several thousands of desorption pulses. The saturation limit is exceeded by far and the net heat transfer to the target surface is significantly growing. This net heat transfer is the result of the small amount of heat entry into the target surface occurring on a ps- to ns-timescale after the laser pulse which, however, accumulates over the long period of irradiation to a considerable extent. Although the incident laser fluence was slightly lower compared to the short-term laser desorption, the absorbed laser fluence has been much larger. The nickel layer coated on gold provides a lower reflection of the laser light and, thus, the absorbed laser fluence might even have exceeded the threshold of plasma generation on the nickel surface. Once all the contaminants are removed, the still ongoing pulsed laser irradiation will lead to the removal of target material. The highly excited substrate electrons cannot transfer their energy to the adsorbate anymore since it has already been removed. So their energy is dissipated by electron diffusion into the bulk. There, the lattice heats up due to electron-phonon coupling. The phonon oscillations transfer energy to the surface atoms in form of vibrational energy and may lead to bond-breaking if the accumulated energy transfer exceeds the potential barrier. This obviously happened for the shot results presented in section 5.5, which clearly contradict to the observations presented in section 5.4.

Figure 5.22 illustrates a surface analysis of a gold foil coated with a 20 nm thick nickel layer after its irradiation by fs-laser pulses. The photomicrographs already indicate definitely that the long-term laser desorption induced not only a removal of surface contaminants but also a removal of nickel atoms. While the non-irradiated region on the left side of the large photomicrograph in the middle exhibits the original nickel layer surface, the surrounded region on its right side shows the uncoated gold foil. The presented X-ray spectra in Figure 5.22 were

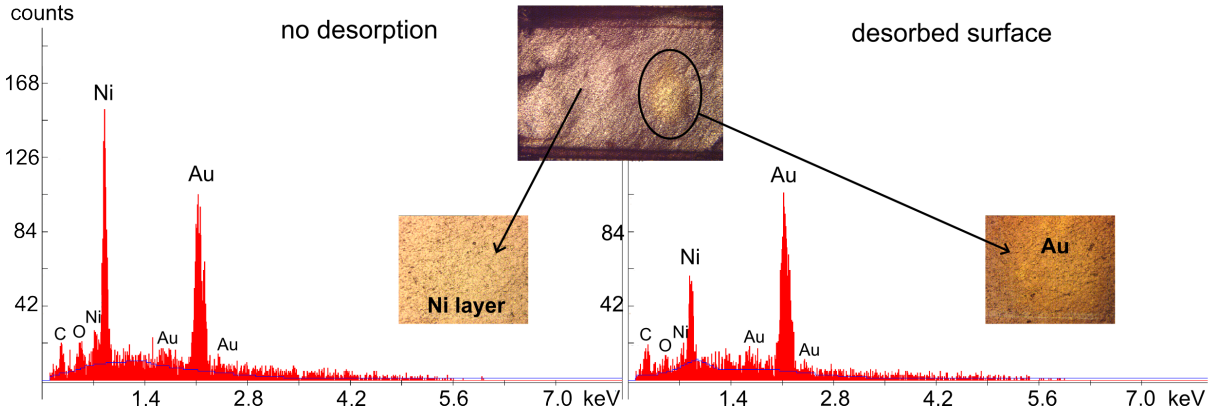


**Figure 5.22:** Energy dispersive X-ray analysis (EDX) of a gold foil coated with a 20 nm thick nickel layer of the untreated target surface (left) and of the desorbed surface (right).

obtained by an energy dispersive X-ray analysis (EDX). It was performed with a scanning electron microscope, which imaged the target foil by scanning it with a focused electron beam of 6 keV corresponding to a penetration depth of 65 nm [204]. The left image shows the obtained X-ray spectrum of the untreated target surface. The dominating peak at an X-ray energy of about 0.86 keV [110] stems from the electronic transitions involving the L-shell [205] of a nickel atom, noted as Ni-L line, for which an atomic fraction of 44 % was measured. The second peak at an energy of 2.12 keV belongs to the Au-M line, i.e. electronic transitions to the M-shell of a gold atom, and has a relative atomic fraction of 35 %. The remaining 21 % consisted of characteristic X-rays from O-K at an energy of 0.52 keV and from C-K at 0.28 keV, thus, both involving electronic transitions to the K-shell of oxygen and carbon, respectively. This clear dominance of nickel on the target surface could not be reproduced in the right X-ray spectrum referring to the analysis of the desorbed surface region. Here, the atomic yield of the Ni-L line decreased to 25 % while the fraction of the Au-M line rose to 46 %. The fraction of the C-K line also increased and obtained a value of 22 %. The remaining 7 % belonged to the O-K line.

The EDX data confirm that the long-term irradiation with fs-laser pulses removed not only the adsorbed contaminants on the target surface but also surface material belonging to the target. This might have led to an implantation of contaminants into the target material since nickel has the property to be a good catalyst for hydrogenation reactions [206]. This would explain the enhanced proton signal seen in Figure 5.20 c). A further plausible explanation for the increased proton and carbon ion energies compared to the shot without applied laser desorption could be the exposure of a contamination layer which was buried between the gold foil and the nickel coating. The gold foils were exposed to normal air conditions and were not treated specially before the sputtering process, under which surface adsorption processes occur (section 4.1.1). The long-term laser desorption may have laid this buried contamination layer open due to the continuous removal of nickel atoms. When the CPA laser pulse finally initiated the TNSA, these contaminants were exposed to the TNSA electric field and experienced a considerably reduced shielding or even no shielding at all. They could therefore be ionized and accelerated efficiently while the electric field was not sufficient to ionize gold atoms and accelerate these.

# 6 Conclusion and Outlook

The present thesis focused on the influence on laser-accelerated ions of femtosecond-laser desorption. It could be demonstrated that the irradiation of metallic target surfaces with ultrashort laser pulses of moderate fluences enabled to clean the target surface successively by removing their surface contaminants. Since the subsequent laser-ion acceleration occurred from a modified target surface structure with a clearly reduced content of contaminants, the resulting ion spectra were significantly influenced by the laser-induced desorption. In the frame of separate desorption measurements the relevant laser fluence regime, in which the desorption takes place, was determined and a characterization of the contamination layer regarding its thickness as well as its composition could be provided.

In the framework of this thesis three experiments were conducted. One experiment based on laser-induced desorption measurements in an ultrahigh vacuum chamber in order to analyze the yield of desorbed particles and was performed at the Petawatt High Energy Laser for Heavy Ion eXperiments (PHELIX) at GSI Helmholtzzentrum für Schwerionenforschung GmbH. The two main experiments with the focus on the laser-driven ion acceleration were performed at the Jupiter Laser Facility of the Lawrence Livermore National Laboratory using the short-pulse high-intensity laser Callisto.

The long-term irradiation of metal foils with femtosecond laser pulses at a repetition rate of 10 Hz enabled to remove the surface adsorbates step by step until the target surface was cleaned. The threshold value of the incoming laser fluence, at which a plasma was generated at the irradiated surface, could be determined experimentally as well as a lower limit under which no desorption was observed. These limits characterize the regime of the laser fluence being relevant for the desorption and resulted in $F_{\text{in}} = (105.5 - 292.3)\,\text{mJ/cm}^2$ for gold and copper as well as $F_{\text{in}} = (22.3 - 105.5)\,\text{mJ/cm}^2$ for aluminum, each with an uncertainty of 21 %. A good agreement of the desorption yield was found for the laser irradiation of the three investigated materials in case of an applied absorbed laser fluence between $2\,\text{mJ/cm}^2$ and $5\,\text{mJ/cm}^2$. The desorption measurements in this fluence regime showed a similar total number of desorbed particles in the order of $10^{13}$, which in terms of the corresponding areal densities amounts to $(5.6 - 8.3) \times 10^{16}$ particles per square centimeter with an underlying uncertainty of 40 % to 50 %. The large error bars mainly stem from the determination of the area from which the atoms were desorbed. Considering a radial Gaussian intensity profile of the desorption pulses the estimate on this area could be improved and an averaged areal density of $(4.27 \pm 1.28) \times 10^{16}$ particles per square centimeter was determined. This value represents a reliable estimate on the typical thickness of contamination layers on metal targets lying in the regime of few nanometers. Diffusion processes of hydrogen from the bulk to the surface have to be regarded as a concomitant effect to the desorption of surface adsorbates, but they play only a minor role, as the partial pressure measurements revealed. The dominant molecular contribution to the desorbed gases results from carbonoxide apart from hydrogen, each amounting to a fraction of $(40 \pm 10)$ %. The large fraction of carbonoxide allows to conclude that the hydrogen content stems predominantly from the dissociation of light hydrocarbons and the contribution of diffusion should rather be a minor one. The resulting atomic areal densities for hydrogen, carbon and oxygen agree very well with the data received from the elastic recoil detection analysis, with which the composition of the contamination layer was investigated, deviating at most

by a factor of two.
Both the obtained values of the areal density of the desorbed gas molecules having formed the contamination layer and their molecular composition represent very fundamental information for the TNSA. The received results on the quantitative and qualitative characterization of the contamination layer can be used as input parameters for numerical simulations. Thus, they improve the modeling of the TNSA substantially.

The application of femtosecond-laser desorption within the scope of the laser-ion acceleration experiments illustrated its strong impact on the ion spectra. Especially in the first experimental campaign the contamination layer on top of the target surface could successively be reduced and the intermediate states between the original contamination layer and a clean target surface were addressed. This resulted in a drop of the number of laser-accelerated protons and carbon ions by up to one order of magnitude and in the appearance of laser-accelerated ions from the target material –in the present case gold, copper and aluminum– since the shielding of the electric field by contaminants had been reduced. Furthermore, the thinner contamination layer led to a redistribution of the observed ion charge states such that ions with low charge states, especially 1+ and 2+, disappeared whereas ions with higher charge states were accelerated more efficiently. The detailed experimental results were published in [1].
In the second experimental campaign, the fs-laser irradiation of the target rear surface was performed over a long period of time, i.e. several minutes. This long-term irradiation desorbed not only the surface contaminants but removed also target atoms from the surface. The most probable explanation involves an increased value of the absorbed laser fluence since the reflectivity of laser light irradiating nickel coated gold foils is about 30 % lower than in case of irradiating pure gold foils. This induces an enhanced energy transfer to the target surface. The desorption yield increases as well as the net heat transfer to the target material, which accumulates over the long period of laser irradiation and subsequently activates reactions leading to the release of surface material. The effect on the subsequent laser-ion acceleration was a more efficient acceleration of protons and carbon ions. These were presumably accelerated from a contamination layer which was buried between the gold foil and the nickel coating and was laid open during the surface cleaning procedure.

## Outlook

The experimental campaigns showed that the physical processes involved in laser ablation and desorption are very complex since they depend on several parameters involving mainly the laser and target properties but also the ambient conditions. Although numerical simulations can provide a helpful estimate on the absorbed laser fluences necessary for the desorption process, their calculation underlies some given uncertainties, like the choice of the model-dependent parameters as the electron-phonon coupling strength or the neglection of the initially nonthermal electron distribution. Furthermore, the conversion of numerically determined absorbed laser fluences into experimentally measurable incident laser fluences requires the knowledge of the reflectivity of the irradiated material. During the laser irradiation its value may vary from those given in the literature [166, 168].
In order to determine the characteristics of the successive target cleaning by femtosecond-laser pulses in detail more extensive parameter studies have to be performed. These regard on the one hand the target properties. The measured desorption yield demonstrates a clear dependence on the target material which is, for example, due to differing electron thermalization times, heat conductivities or the above mentioned reflectance of the laser light. The ability of storing hydrogen in the atomic lattice is also material-dependent and plays a role for diffusion

processes being a concomitant effect during the laser desorption. On the other hand, the dependence of the desorption yield on the laser fluence could be investigated by varying the laser spot size contrary to its pulse energy, followed by an analysis of the target surface with e.g. force measurements with the atomic force microscope. A further aspect represents the dependence of the desorption yield on the laser wavelength as well as on the repetition rate of the desorption pulses. All these proposals, however, require measurements in ultrahigh vacuum conditions and cannot be done routinely during conventional laser-ion acceleration experiments.
An opportunity would be an experimental setup which allows for the application of both femtosecond laser irradiation on the target surface and a subsequent irradiation of this laser-treated area by heavy ions with energies of few MeV per nucleon, which probe the sample surface after the laser-induced desorption in the framework of an elastic recoil detection analysis. Such a combined experiment is worldwide only possible at the Z6 target chamber of GSI Helmholtzzentrum für Schwerionenforschung GmbH, where both a laser beam line and an ion beam line are available. Since the target surface becomes also cleaned by the probing ion beam, the ion beam should permanently irradiate a different part of the surface from which the desorption occurred. This could be realized by a slowly rotating target holder.
With the help of thermo-cameras [207] measuring the infrared radiation the target surface temperature can be monitored with a resolution of few ten mK [208]. This allows to study a possible heat contribution to the laser-induced desorption process and, thus, gives an indication of hydrogen diffusion on long term runs. Since UHV conditions are not necessary within this temperature measurement, it could be applied also during experiments with subsequent TNSA.

The usage of previously characterized multilayer targets consisting of a very smooth metal substrate, which becomes covered by few ultrathin layers of different materials, represents an alternative way to femtosecond-laser desorption in order to provide a depth information of the electric field distribution. Such a mapping of the spatial electric field distribution reaching into the target will deliver fundamental information about the establishment of the electric field potential during the laser-ion acceleration by the Target Normal Sheath Acceleration mechanism. However, the construction of such a multilayer target is extremely challenging. It requires a very smooth metal foil of thicknesses between 5 µm and 10 µm having a surface roughness considerably below 20 nm. The material of the coating has to be selected carefully such that only a minimal diffusion between the adjoined materials sets in. Furthermore, the whole target manufacturing process should take place under vacuum conditions of $10^{-6}$ mbar and below in order to prevent the implantation of contaminations by adsorption of gas molecules in the air.
An alternative approach beyond the sputtering process constitutes the thin film processing by evaporation, which is conducted in much lower vacuum pressures, leading to a reduced amount of incorporated residual gas in the film. Due to the lower impact energy of the particles on the target surface compared to ion sputtering this technique provides a more defined interface between the target material and the coating. Even further, dedicated layers without contamination could be fabricated by ion implantation.

The measurement of the maximum energies of ions accelerated from layers of different materials at known depth with respect to the target rear surface allows to estimate the accelerating electric field potential at that specific depth. With the help of both the complete nondestructive removal of the contamination layer by the femtosecond-laser desorption and the information about the spatial electric field distribution a controlled Target Normal Sheath Acceleration of ions of a distinct charge state with a well-defined energy spectrum will be possible in the future.

# Bibliography


[1] G. Hoffmeister, C. Bellei, K. Harres, D. Ivanov, D. Kraus, A. Pelka, B. Rethfeld, G. Schaumann, and M. Roth. Influence of fs-laser desorption on target normal sheath accelerated ions. *Phys. Rev. ST Accel. Beams*, 16:041304, 2013.

[2] D. Strickland and G. Mourou. Compression of amplified chirped optical pulses. *Opt. Commun.*, 56(3):219 – 221, 1985.

[3] D. Umstadter. Review of physics and applications of relativistic plasmas driven by ultra-intense lasers. *Phys. Plasmas*, 8:1774–1785, 2001.

[4] W. P. Leemans, B. Nagler, A. J. Gonsalves, Cs. Tóth, K. Nakamura, C. G. R. Geddes, E. Esarey, C. B. Schroeder, and S. M. Hooker. GeV electron beams from a centimetre-scale accelerator. *Nature Physics*, 2:696–699, 2006.

[5] C. G. R. Geddes, Cs. Toth, J. van Tilborg, E. Esarey, C. B. Schroeder, D. Bruhwiler, C. Nieter, J. Cary, and W. P. Leemans. High-quality electron beams from a laser wakefield accelerator using plasma-channel guiding. *Nature*, 431:538–541, 2004.

[6] S. P. D. Mangles, C. D. Murphy, Z. Najmudin, A. G. R. Thomas, J. L. Collier, A. E. Dangor, E. J. Divall, P. S. Foster, J. G. Gallacher, C. J. Hooker, D. A. Jaroszynski, A. J. Langley, W. B. Mori, P. A. Norreys, F. S. Tsung, R. Viskup, B. R. Walton, and K. Krushelnick. Monoenergetic beams of relativistic electrons from intense laser-plasma interactions. *Nature*, 431:535–538, 2004.

[7] K. Krushelnick, E. L. Clark, Z. Najmudin, M. Salvati, M. I. K. Santala, M. Tatarakis, A. E. Dangor, V. Malka, D. Neely, R. Allott, and C. Danson. Multi-MeV Ion Production from High-Intensity Laser Interactions with Underdense Plasmas. *Phys. Rev. Lett.*, 83:737–740, 1999.

[8] E. L. Clark, K. Krushelnick, J. R. Davies, M. Zepf, M. Tatarakis, F. N. Beg, A. Machacek, P. A. Norreys, M. I. K. Santala, I. Watts, and A. E. Dangor. Measurements of energetic proton transport through magnetized plasma from intense laser interactions with solids. *Phys. Rev. Lett.*, 84:670–673, 2000.

[9] A. Maksimchuk, S. Gu, K. Flippo, D. Umstadter, and V. Yu. Bychenkov. Forward ion acceleration in thin films driven by a high-intensity laser. *Phys. Rev. Lett.*, 84:4108–4111, 2000.

[10] R. A. Snavely, M. H. Key, S. P. Hatchett, T. E. Cowan, M. Roth, T. W. Phillips, M. A. Stoyer, E. A. Henry, T. C. Sangster, M. S. Singh, S. C. Wilks, A. MacKinnon, A. Offenberger, D. M. Pennington, K. Yasuike, A. B. Langdon, B. F. Lasinski, J. Johnson, M. D. Perry, and E. M. Campbell. Intense high-energy proton beams from petawatt-laser irradiation of solids. *Phys. Rev. Lett.*, 85:2945–2948, 2000.

[11] T. E. Cowan, J. Fuchs, H. Ruhl, A. Kemp, P. Audebert, M. Roth, R. Stephens, I. Barton, A. Blažević, E. Brambrink, J. Cobble, J. Fernández, J.-C. Gauthier, M. Geißel, M. Hegelich, J. Kaae, S. Karsch, G. P. Le Sage, S. Letzring, M. Manclossi, S. Meyroneinc, A. Newkirk, H. Pépin, and N. Renard-LeGalloudec. Ultralow Emittance, Multi-MeV Proton Beams from a Laser Virtual-Cathode Plasma Accelerator. *Phys. Rev. Lett.*, 92:204801, 2004.

[12] S. P. Hatchett, C. G. Brown, T. E. Cowan, E. A. Henry, J. S. Johnson, M. H. Key, J. A. Koch, A. B. Langdon, B. F. Lasinski, R. W. Lee, A. J. Mackinnon, D. M. Pennington, M. D. Perry, T. W. Phillips, M. Roth, T. C. Sangster, M. S. Singh, R. A. Snavely, M. A. Stoyer, S. C. Wilks, and K. Yasuike. Electron, photon, and ion beams from the relativistic interaction of petawatt laser pulses with solid targets. *Phys. Plasmas*, 7:2076, 2000.

[13] M. Zepf, E. L. Clark, K. Krushelnick, F. N. Beg, C. Escoda, A. E. Dangor, M. I. K. Santala, M. Tatarakis, I. F. Watts, P. A. Norreys, R. J. Clarke, J. R. Davies, M. A. Sinclair, R. D. Edwards, T. J. Goldsack, I. Spencer, and K. W. D. Ledingham. Fast particle generation and energy transport in laser-solid interactions. *Phys. Plasmas*, 8:2323–2330, 2001.

[14] S. Busold, D. Schumacher, O. Deppert, C. Brabetz, S. Frydrych, F. Kroll, M. Joost, H. Al-Omari, A. Blažević, B. Zielbauer, I. Hofmann, V. Bagnoud, T. E. Cowan, and M. Roth. Focusing and transport of high-intensity multi-MeV proton bunches from a compact laser-driven source. *Phys. Rev. ST Accel. Beams*, 16:101302, 2013.

[15] S. Busold, A. Almomani, V. Bagnoud, W. Barth, S. Bedacht, A. Blažević, O. Boine-Frankenheim, C. Brabetz, T. Burris-Mog, T.E. Cowan, O. Deppert, M. Droba, H. Eickhoff, U. Eisenbarth, K. Harres, G. Hoffmeister, I. Hofmann, O. Jaeckel, R. Jaeger, M. Joost, S. Kraft, F. Kroll, M. Kaluza, O. Kester, Z. Lecz, T. Merz, and F. N˙ Shaping laser accelerated ions for future applications - The LIGHT collaboration. *Nucl. Instrum. Meth. A*, 740:94 – 98, 2014.

[16] M. Temporal, R. Ramis, J. J. Honrubia, and S. Atzeni. Fast ignition induced by shocks generated by laser-accelerated proton beams. *Plasma Phys. Control. Fusion*, 51:035010, 2009.

[17] M. Roth, T. E. Cowan, M. H. Key, S. P. Hatchett, C. Brown, W. Fountain, J. Johnson, D. M. Pennington, R. A. Snavely, S. C. Wilks, K. Yasuike, H. Ruhl, F. Pegoraro, S. V. Bulanov, E. M. Campbell, M. D. Perry, and H. Powell. Fast ignition by intense laser-accelerated proton beams. *Phys. Rev. Lett.*, 86:436–439, 2001.

[18] V. Yu Bychenkov, W. Rozmus, A. Maksimchuk, D. Umstadter, and C. E. Capjack. Fast ignitor concept with light ions. *Plasma Physics Reports*, 27:1017–1020, 2001.

[19] M. Borghesi, D. H. Campbell, A. Schiavi, M. G. Haines, O. Willi, A. J. MacKinnon, P. Patel, L. A. Gizzi, M. Galimberti, R. J. Clarke, F. Pegoraro, H. Ruhl, and S. Bulanov. Electric field detection in laser-plasma interaction experiments via the proton imaging technique. *Phys. Plasmas*, 9:2214–2220, 2002.

[20] M. Borghesi, L. Romagnani, A. Schiavi, D. H. Campbell, O. Willi, A.J. Mackinnon, M. Galimberti, L. A. Gizzi, R. J. Clarke, and S. Hawkes. Measurement of highly transient electrical charging following high-intensity laser-solid interaction. *Appl. Phys. Lett.*, 82:1529–1531, 2003.

[21] M. Borghesi, A. Schiavi, D. H. Campbell, M. G. Haines, O. Willi, A. J. MacKinnon, L. A. Gizzi, M. Galimberti, R. J. Clarke, and H. Ruhl. Proton imaging: a diagnostic for inertial confinement fusion/fast ignitor studies. *Plasma Physics and Controlled Fusion*, 43(12A):A267, 2001.

[22] M. Roth, A. Blažević, M. Geißel, T. Schlegel, T. E. Cowan, M. Allen, J.-C. Gauthier, P. Audebert, J. Fuchs, J. Meyer-ter Vehn, M. Hegelich, S. Karsch, and A. Pukhov. Energetic ions generated by laser pulses: A detailed study on target properties. *Phys. Rev. ST Accel. Beams*, 5:061301, 2002.

[23] P. K. Patel, A. J. Mackinnon, M. H. Key, T. E. Cowan, M. E. Foord, M. Allen, D. F. Price, H. Ruhl, P. T. Springer, and R. Stephens. Isochoric heating of solid-density matter with an ultrafast proton beam. *Phys. Rev. Lett.*, 91:125004, 2003.

[24] A. Mancic, J. Robiche, P. Antici, P. Audebert, C. Blancard, P. Combis, F. Dorchies, G. Faussurier, S. Fourmaux, M. Harmand, R. Kodama, L. Lancia, S. Mazevet, M. Nakatsutsumi, O. Peyrusse, V. Recoules, P. Renaudin, R. Shepherd, and J. Fuchs. Isochoric heating of solids by laser-accelerated protons: Experimental characterization and self-consistent hydrodynamic modeling. *High Energy Density Physics*, 6:21 – 28, 2010.

[25] A. Pelka, G. Gregori, D. O. Gericke, J. Vorberger, S. H. Glenzer, M. M. Günther, K. Harres, R. Heathcote, A. L. Kritcher, N. L. Kugland, B. Li, M. Makita, J. Mithen, D. Neely, C. Niemann, A. Otten, D. Riley, G. Schaumann, M. Schollmeier, An. Tauschwitz, and M. Roth. Ultrafast melting of carbon induced by intense proton beams. *Phys. Rev. Lett.*, 105:265701, 2010.

[26] M. Roth, D. Jung, K. Falk, N. Guler, O. Deppert, M. Devlin, A. Favalli, J. Fernandez, D. Gautier, M. Geissel, R. Haight, C. E. Hamilton, B. M. Hegelich, R. P. Johnson, F. Merrill, G. Schaumann, K. Schoenberg, M. Schollmeier, T. Shimada, T. Taddeucci, J. L. Tybo, F. Wagner, S. A. Wender, C. H. Wilde, and G. A. Wurden. Bright laser-driven neutron source based on the relativistic transparency of solids. *Phys. Rev. Lett.*, 110:044802, 2013.

[27] S. V. Bulanov and V. S. Khoroshkov. Feasibility of using laser ion accelerators in proton therapy. *Plasma Phys. Reports*, 28:453–456, 2002.

[28] S. D. Kraft, C. Richter, K. Zeil, M. Baumann, E. Beyreuther, S. Bock, M. Bussmann, T. E. Cowan, Y. Dammene, W. Enghardt, U. Helbig, L. Karsch, T. Kluge, L. Laschinsky, E. Lessmann, J. Metzkes, D. Naumburger, R. Sauerbrey, M. Schürer, M. Sobiella, J. Woithe, U. Schramm, and J. Pawelke. Dose-dependent biological damage of tumour cells by laser-accelerated proton beams. *New J. Phys.*, 12:085003, 2010.

[29] E. Fourkal, I. Velchev, C.-M. Ma, and J. Fan. Linear energy transfer of proton clusters. *Phys. Med. Biol.*, 56:3123, 2011.

[30] U. Masood, M. Bussmann, T. E. Cowan, W. Enghardt, L. Karsch, F. Kroll, U. Schramm, and J. Pawelke. A compact solution for ion beam therapy with laser accelerated protons. *Appl. Phys. B*, pages 1–12, 2014.

[31] S. C. Wilks, A. B. Langdon, T. E. Cowan, M. Roth, M. Singh, S. Hatchett, M. H. Key, D. Pennington, A. MacKinnon, and R. A. Snavely. Energetic proton generation in ultra-intense laser-solid interactions. *Phys. Plasmas*, 8:542–549, 2001.

[32] A. J. Mackinnon, M. Borghesi, S. Hatchett, M. H. Key, P. K. Patel, H. Campbell, A. Schiavi, R. Snavely, S. C. Wilks, and O. Willi. Effect of Plasma Scale Length on Multi-MeV Proton Production by Intense Laser Pulses. *Phys. Rev. Lett.*, 86:1769–1772, 2001.

[33] M. Allen, P. K. Patel, A. Mackinnon, D. Price, S. Wilks, and E. Morse. Direct Experimental Evidence of Back-Surface Ion Acceleration from Laser-Irradiated Gold Foils. *Phys. Rev. Lett.*, 93:265004, 2004.

[34] J. Fuchs, Y. Sentoku, S. Karsch, J. Cobble, P. Audebert, A. Kemp, A. Nikroo, P. Antici, E. Brambrink, A. Blažević, E. M. Campbell, J. C. Fernández, J.-C. Gauthier, M. Geißel, M. Hegelich, H. Pépin, H. Popescu, N. Renard-LeGalloudec, M. Roth, J. Schreiber,

R. Stephens, and T. E. Cowan. Comparison of laser ion acceleration from the front and rear surfaces of thin foils. *Phys. Rev. Lett.*, 94:045004, 2005.

[35] J. Fuchs, Y. Sentoku, E. d'Humières, T. E. Cowan, J. Cobble, P. Audebert, A. Kemp, A. Nikroo, P. Antici, E. Brambrink, A. Blažević, E. M. Campbell, J. C. Fernández, J.-C. Gauthier, M. Geißel, M. Hegelich, S. Karsch, H. Popescu, N. Renard-LeGalloudec, M. Roth, J. Schreiber, R. Stephens, and H. Pépin. Comparative spectra and efficiencies of ions laser-accelerated forward from the front and rear surfaces of thin solid foils. *Phys. Plasmas*, 14:053105, 2007.

[36] Y. Sentoku, T. E. Cowan, A. Kemp, and H. Ruhl. High energy proton acceleration in interaction of short laser pulse with dense plasma target. *Phys. Plasmas*, 10:2009–2015, 2003.

[37] M. Borghesi, J. Fuchs, S. V. Bulanov, A. J. MacKinnon, P. K. Patel, and M. Roth. Fast Ion Generation by High-Intensity Laser Irradiation of Solid Targets and Applications. *Fusion Science and Technology*, 49:412–439, 2006.

[38] J. Fuchs, P. Antici, E. d'Humières, E. Lefebvre, M. Borghesi, E. Brambrink, C. A. Cecchetti, M. Kaluza, V. Malka, M. Manclossi, S. Meyroneinc, P. Mora, J. Schreiber, T. Toncian, H. Pépin, and P. Audebert. Laser-driven proton scaling laws and new paths towards energy increase. *Nat. Phys.*, 2:48–54, 2006.

[39] M. Borghesi, A. Bigongiari, S. Kar, A. Macchi, L. Romagnani, P. Audebert, J. Fuchs, T. Toncian, O. Willi, S. V. Bulanov, A. J. Mackinnon, and J. C. Gauthier. Laser-driven proton acceleration: source optimization and radiographic applications. *Plasma Physics and Controlled Fusion*, 50(12):124040, 2008.

[40] P. Mora. Plasma expansion into a vacuum. *Phys. Rev. Lett.*, 90:185002, 2003.

[41] P. Mora. Thin-foil expansion into a vacuum. *Phys. Rev. E*, 72:056401, 2005.

[42] T. Grismayer and P. Mora. Influence of a finite initial ion density gradient on plasma expansion into a vacuum. *Phys. Plasmas*, 13:032103, 2006.

[43] J. Fuchs, T. E. Cowan, P. Audebert, H. Ruhl, L. Gremillet, A. Kemp, M. Allen, A. Blažević, J.-C. Gauthier, M. Geißel, M. Hegelich, S. Karsch, P. Parks, M. Roth, Y. Sentoku, R. Stephens, and E. M. Campbell. Spatial Uniformity of Laser-Accelerated Ultrahigh-Current MeV Electron Propagation in Metals and Insulators. *Phys. Rev. Lett.*, 91:255002, 2003.

[44] J. Schreiber. *Ion Acceleration driven by High-Intensity Laser Pulses*. Phd thesis, Ludwig-Maximilians-Universität München, 2006.

[45] Z. Lécz, O. Boine-Frankenheim, and V. Kornilov. Target normal sheath acceleration for arbitrary proton layer thickness. *Nucl. Instrum. Meth. A*, 727:51– 58, 2013.

[46] D. Autrique, Z. Chen, V. Alexiades, A. Bogaerts, and B. Rethfeld. A multiphase model for pulsed ns-laser ablation of copper in an ambient gas. *AIP Conf. Proceed.*, 1464(1):648–659, 2012.

[47] C. Frischkorn and M. Wolf. Femtochemistry at Metal Surfaces: Nonadiabatic Reaction Dynamics. *Chem. Rev.*, 106:4207–4233, 2006.

[48] B. M. Hegelich, B. J. Albright, J. Cobble, K. Flippo, S. Letzring, M. Paffett, H. Ruhl, J. Schreiber, R. K. Schulze, and J. C. Fernández. Laser acceleration of quasi-monoenergetic MeV ion beams. *Nature*, 439:441–444, 2006.

[49] A. Macchi. *A Superintense Laser-Plasma Interaction Theory Primer*. Springer-Verlag, 2013.

[50] P. Mulser and D. Bauer. *High power laser-matter interaction*. Springer-Verlag, 2010.

[51] P. Gibbon. *Short pulse laser interactions with matter - An introduction*. Imperial College Press, 2005.

[52] J. D. Lawson. *IEEE Trans. Nucl. Sci.*, NS-26:4217, 1979.

[53] P. M. Woodward. *J. Inst. Electr. Eng.*, 93:1554, 1947.

[54] T. Tajima and J. M. Dawson. Laser electron accelerator. *Phys. Rev. Lett.*, 43:267–270, 1979.

[55] C. Joshi, W. B. Mori, T. Katsouleas, J. M. Dawson, J. M. Kindel, and D. W. Forslund. Ultrahigh gradient particle acceleration by intense laser-driven plasma density waves. *Nature*, 311:525–529, 1984.

[56] R. Jung. *Laser-plasma interaction with ultra-short laser pulses*. Phd thesis, Heinrich-Heine-Universität Düsseldorf, 2007.

[57] D. Bauer, P. Mulser, and W. H. Steeb. Relativistic ponderomotive force, uphill acceleration, and transition to chaos. *Phys. Rev. Lett.*, 75:4622–4625, 1995.

[58] L. Yin, B. J. Albright, B. M. Hegelich, K. J. Bowers, K. A. Flippo, T. J. T. Kwan, and J. C. Fernández. Monoenergetic and GeV ion acceleration from the laser breakout afterburner using ultrathin targets. *Phys. Plasmas*, 14:056706, 2007.

[59] J. Fuchs, J. C. Adam, F. Amiranoff, S. D. Baton, P. Gallant, L. Gremillet, A. Héron, J. C. Kieffer, G. Laval, G. Malka, J. L. Miquel, P. Mora, H. Pépin, and C. Rousseaux. Transmission through highly overdense plasma slabs with a subpicosecond relativistic laser pulse. *Phys. Rev. Lett.*, 80:2326–2329, 1998.

[60] A. Macchi, M. Borghesi, and M. Passoni. Ion acceleration by superintense laser-plasma interaction. *Rev. Mod. Phys.*, 85:751–793, 2013.

[61] S. C. Wilks, W. L. Kruer, M. Tabak, and A. B. Langdon. Absorption of ultra-intense laser pulses. *Phys. Rev. Lett.*, 69:1383–1386, 1992.

[62] P. Gibbon and A. R. Bell. Collisionless absorption in sharp-edged plasmas. *Phys. Rev. Lett.*, 68:1535–1538, 1992.

[63] F. Brunel. Not-so-resonant, resonant absorption. *Phys. Rev. Lett.*, 59:52–55, 1987.

[64] A. Pukhov, Z.-M. Sheng, and J. Meyer-ter Vehn. Particle acceleration in relativistic laser channels. *Phys. Plasmas*, 6:2847–2854, 1999.

[65] W. L. Kruer and K. Estabrook. $j \times$ B heating by very intense laser light. *Phys. Fluids*, 28:430, 1985.

[66] G. Malka and J. L. Miquel. Experimental confirmation of ponderomotive-force electrons produced by an ultrarelativistic laser pulse on a solid target. *Phys. Rev. Lett.*, 77:75–78, 1996.

[67] J. D. Jackson. *Classical Electrodynamics*. John Wiley & Sons, 1975.

[68] H. Popescu, S. D. Baton, F. Amiranoff, C. Rousseaux, M. Rabec Le Gloahec, J. J. Santos, L. Gremillet, M. Koenig, E. Martinolli, T. Hall, J. C. Adam, A. Heron, and D. Batani. Subfemtosecond, coherent, relativistic, and ballistic electron bunches generated at $1\omega_0$ and $2\omega_0$ in high intensity laser-matter interaction. *Phys. Plasmas*, 12:063106, 2005.

[69] J. J. Santos, F. Amiranoff, S. D. Baton, L. Gremillet, M. Koenig, E. Martinolli, M. Rabec Le Gloahec, C. Rousseaux, D. Batani, A. Bernardinello, G. Greison, and T. Hall. Fast electron transport in ultraintense laser pulse interaction with solid targets by rear-side self-radiation diagnostics. *Phys. Rev. Lett.*, 89:025001, 2002.

[70] S. D. Baton, J. J. Santos, F. Amiranoff, H. Popescu, L. Gremillet, M. Koenig, E. Martinolli, O. Guilbaud, C. Rousseaux, M. Rabec Le Gloahec, T. Hall, D. Batani, E. Perelli, F. Scianitti, and T. E. Cowan. Evidence of ultrashort electron bunches in laser-plasma interactions at relativistic intensities. *Phys. Rev. Lett.*, 91:105001, 2003.

[71] K. B. Wharton, S. P. Hatchett, S. C. Wilks, M. H. Key, J. D. Moody, V. Yanovsky, A. A. Offenberger, B. A. Hammel, M. D. Perry, and C. Joshi. Experimental measurements of hot electrons generated by ultraintense ( $> 10^{19}$ W/cm$^2$) laser-plasma interactions on solid-density targets. *Phys. Rev. Lett.*, 81:822–825, 1998.

[72] P. Köster, K. Akli, D. Batani, S. Baton, R. G. Evans, A. Giulietti, D. Giulietti, L. A. Gizzi, J. S. Green, M Koenig, L. Labate, A. Morace, P. Norreys, F. Perez, J. Waugh, N. Woolsey, and K. L. Lancaster. Experimental investigation of fast electron transport through K$\alpha$ imaging and spectroscopy in relativistic laser-solid interactions. *Plasma Phys. Control. Fusion*, 51:014007, 2009.

[73] K. L. Lancaster, J. S. Green, D. S. Hey, K. U. Akli, J. R. Davies, R. J. Clarke, R. R. Freeman, H. Habara, M. H. Key, R. Kodama, K. Krushelnick, C. D. Murphy, M. Nakatsutsumi, P. Simpson, R. Stephens, C. Stoeckl, T. Yabuuchi, M. Zepf, and P. A. Norreys. Measurements of energy transport patterns in solid density laser plasma interactions at intensities of $5 \times 10^{20}$ W/cm$^2$. *Phys. Rev. Lett.*, 98:125002, 2007.

[74] D. Batani. Transport in dense matter of relativistic electrons produced in ultra-high-intensity laser interactions. *Laser and Particle Beams*, 20:321–336, 2002.

[75] H. A. Bethe. Molière's theory of multiple scattering. *Phys. Rev.*, 89:1256–1266, 1953.

[76] A. R. Bell, A. P. L. Robinson, M. Sherlock, R. J. Kingham, and W. Rozmus. Fast electron transport in laser-produced plasmas and the KALOS code for solution of the Vlasov-Fokker-Planck equation. *Plasma Phys. Control. Fusion*, 48:R37–R57, 2006.

[77] A. R. Bell, J. R. Davies, S. Guerin, and H. Ruhl. Fast-electron transport in high-intensity short-pulse laser-solid experiments. *Plasma Phys. Control. Fusion*, 39:653–659, 1997.

[78] F. Pisani, A. Bernardinello, D. Batani, A. Antonicci, E. Martinolli, M. Koenig, L. Gremillet, F. Amiranoff, S. Baton, J. Davies, T. Hall, D. Scott, P. Norreys, A. Djaoui, C. Rousseaux, P. Fews, H. Bandulet, and H. Pepin. Experimental evidence of electric inhibition in fast electron penetration and of electric-field-limited fast electron transport in dense matter. *Phys. Rev. E*, 62:R5927–R5930, 2000.

[79] E. S. Weibel. Spontaneously growing transverse waves in a plasma due to an anisotropic velocity distribution. *Phys. Rev. Lett.*, 2:83–84, 1959.

[80] F. Califano, F. Pegoraro, S. V. Bulanov, and A. Mangeney. Kinetic saturation of the Weibel instability in a collisionless plasma. *Phys. Rev. E*, 57:7048–7059, 1998.

[81] R. Lee and M. Lampe. Electromagnetic instabilities, filamentation, and focusing of relativistic electron beams. *Phys. Rev. Lett.*, 31:1390–1393, 1973.

[82] M. S. Wei, F. N. Beg, E. L. Clark, A. E. Dangor, R. G. Evans, A. Gopal, K. W. D. Ledingham, P. McKenna, P. A. Norreys, M. Tatarakis, M. Zepf, and K. Krushelnick. Observations of the filamentation of high-intensity laser-produced electron beams. *Phys. Rev. E*, 70:056412, 2004.

[83] M. Manclossi, J. J. Santos, D. Batani, J. Faure, A. Debayle, V. T. Tikhonchuk, and V. Malka. Study of ultraintense laser-produced fast-electron propagation and filamentation in insulator and metal foil targets by optical emission diagnostics. *Phys. Rev. Lett.*, 96:125002, 2006.

[84] M. Schollmeier. *Optimization and control of laser-accelerated proton beams*. Phd thesis, Technische Universität Darmstadt, 2008.

[85] M. Honda, J. Meyer-ter Vehn, and A. Pukhov. Two-dimensional particle-in-cell simulation for magnetized transport of ultra-high relativistic currents in plasma. *Phys. Plasmas*, 7:1302–1308, 2000.

[86] H. Alfvén. On the motion of cosmic rays in interstellar space. *Phys. Rev.*, 55:425–429, 1939.

[87] J. R. Davies. The Alfvén limit revisited and its relevance to laser-plasma interactions. *Laser and Particle Beams*, 24:299–310, 2006.

[88] Y. Sentoku, K. Mima, Z. M. Sheng, P. Kaw, K. Nishihara, and K. Nishikawa. Three-dimensional particle-in-cell simulations of energetic electron generation and transport with relativistic laser pulses in overdense plasmas. *Phys. Rev. E*, 65:046408, 2002.

[89] Y. Sentoku, K. Mima, P. Kaw, and K. Nishikawa. Anomalous Resistivity Resulting from MeV-Electron Transport in Overdense Plasma. *Phys. Rev. Lett.*, 90:155001, 2003.

[90] J. J. Honrubia, A. Antonicci, and D. Moreno. Hybrid simulations of fast electron transport in conducting media. *Laser and Particle Beams*, 22:129–135, 2004.

[91] L. Gremillet, G. Bonnaud, and F. Amiranoff. Filamented transport of laser-generated relativistic electrons penetrating a solid target. *Phys. Plasmas*, 9:941–948, 2002.

[92] E. Martinolli, M. Koenig, S. D. Baton, J. J. Santos, F. Amiranoff, D. Batani, E. Perelli-Cippo, F. Scianitti, L. Gremillet, R. Mélizzi, A. Decoster, C. Rousseaux, T. A. Hall, M. H. Key, R. Snavely, A. J. MacKinnon, R. R. Freeman, J. A. King, R. Stephens, D. Neely, and R. J. Clarke. Fast-electron transport and heating of solid targets in high-intensity laser interactions measured by K$\alpha$ fluorescence. *Phys. Rev. E*, 73:046402, 2006.

[93] J. A. Koch, M. H. Key, R. R. Freeman, S. P. Hatchett, R. W. Lee, D. Pennington, R. B. Stephens, and M. Tabak. Experimental measurements of deep directional columnar heating by laser-generated relativistic electrons at near-solid density. *Phys. Rev. E*, 65:016410, 2001.

[94] R. B. Stephens, R. A. Snavely, Y. Aglitskiy, F. Amiranoff, C. Andersen, D. Batani, S. D. Baton, T. Cowan, R. R. Freeman, T. Hall, S. P. Hatchett, J. M. Hill, M. H. Key, J. A.

King, J. A. Koch, M. Koenig, A. J. MacKinnon, K. L. Lancaster, E. Martinolli, P. Norreys, E. Perelli-Cippo, M. Rabec Le Gloahec, C. Rousseaux, J. J. Santos, and F. Scianitti. K$\alpha$ fluorescence measurement of relativistic electron transport in the context of fast ignition. *Phys. Rev. E*, 69:066414, 2004.

[95] J. S. Green, V. M. Ovchinnikov, R. G. Evans, K. U. Akli, H. Azechi, F. N. Beg, C. Bellei, R. R. Freeman, H. Habara, R. Heathcote, M. H. Key, J. A. King, K. L. Lancaster, N. C. Lopes, T. Ma, A. J. MacKinnon, K. Markey, A. McPhee, Z. Najmudin, P. Nilson, R. Onofrei, R. Stephens, K. Takeda, K. A. Tanaka, W. Theobald, T. Tanimoto, J. Waugh, L. Van Woerkom, N. C. Woolsey, M. Zepf, J. R. Davies, and P. A. Norreys. Effect of laser intensity on fast-electron-beam divergence in solid-density plasmas. *Phys. Rev. Lett.*, 100:015003, 2008.

[96] J. R. Davies. How wrong is collisional Monte Carlo modeling of fast electron transport in high-intensity laser-solid interactions? *Phys. Rev. E*, 65:026407, 2002.

[97] M. H. Key, M. D. Cable, T. E. Cowan, K. G. Estabrook, B. A. Hammel, S. P. Hatchett, E. A. Henry, D. E. Hinkel, J. D. Kilkenny, J. A. Koch, W. L. Kruer, A. B. Langdon, B. F. Lasinski, R. W. Lee, B. J. MacGowan, A. MacKinnon, J. D. Moody, M. J. Moran, A. A. Offenberger, D. M. Pennington, M. D. Perry, T. J. Phillips, T. C. Sangster, M. S. Singh, M. A. Stoyer, M. Tabak, G. L. Tietbohl, M. Tsukamoto, K. Wharton, and S. C. Wilks. Hot electron production and heating by hot electrons in fast ignitor research. *Phys. Plasmas*, 5:1966–1972, 1998.

[98] Y. Ping, R. Shepherd, B. F. Lasinski, M. Tabak, H. Chen, H. K. Chung, K. B. Fournier, S. B. Hansen, A. Kemp, D. A. Liedahl, K. Widmann, S. C. Wilks, W. Rozmus, and M. Sherlock. Absorption of short laser pulses on solid targets in the ultrarelativistic regime. *Phys. Rev. Lett.*, 100:085004, 2008.

[99] V. Yanovsky, V. Chvykov, G. Kalinchenko, P. Rousseau, T. Planchon, T. Matsuoka, A. Maksimchuk, J. Nees, G. Cheriaux, G. Mourou, and K. Krushelnick. Ultra-high intensity-300-TW laser at 0.1 Hz repetition rate. *Opt. Express*, 16:2109–2114, 2008.

[100] S. J. Gitomer, R. D. Jones, F. Begay, A. W. Ehler, J. F. Kephart, and R. Kristal. Fast ions and hot electrons in the laser-plasma interaction. *Phys. Fluids*, 29:2679–2688, 1986.

[101] A. P. Fews, P. A. Norreys, F. N. Beg, A. R. Bell, A. E. Dangor, C. N. Danson, P. Lee, and S. J. Rose. Plasma Ion Emission from High Intensity Picosecond Laser Pulse Interactions with Solid Targets. *Phys. Rev. Lett.*, 73:1801–1804, 1994.

[102] F. N. Beg, A. R. Bell, A. E. Dangor, C. N. Danson, A. P. Fews, M. E. Glinsky, B. A. Hammel, P. Lee, P. A. Norreys, and M. Tatarakis. A study of picosecond laser-solid interactions up to $10^{19}$ Wcm$^{-2}$. *Phys. Plasmas*, 4:447–457, 1997.

[103] M. Passoni and M. Lontano. One-dimensional model of the electrostatic ion acceleration in the ultraintense laser-solid interaction. *Laser and Particle Beams*, 22:163–169, 2004.

[104] A. P. L. Robinson, M. Zepf, S. Kar, R. G. Evans, and C. Bellei. Radiation pressure acceleration of thin foils with circularly polarized laser pulses. *New Journal of Physics*, 10:013021, 2008.

[105] F. Nürnberg. *Laser-Accelerated Proton Beams as a New Particle Source*. Phd thesis, Technische Universität Darmstadt, 2010.

[106] J. E. Crow, P. L. Auer, and Allen. The expansion of plasma into vacuum. *J. Plasma Physics*, 14:65–76, 1975.

[107] A. J. Mackinnon, Y. Sentoku, P. K. Patel, D. W. Price, S. Hatchett, M. H. Key, C. Andersen, R. Snavely, and R. R. Freeman. Enhancement of proton acceleration by hot-electron recirculation in thin foils irradiated by ultraintense laser pulses. *Phys. Rev. Lett.*, 88:215006, 2002.

[108] S. Augst, D. Strickland, D. D. Meyerhofer, S. L. Chin, and J. H. Eberly. Tunneling ionization of noble gases in a high-intensity laser field. *Phys. Rev. Lett.*, 63:2212–2215, 1989.

[109] P. McKenna, D. C. Carroll, R. J. Clarke, R. G. Evans, K. W. D. Ledingham, F. Lindau, O. Lundh, T. McCanny, D. Neely, A. P. L. Robinson, L. Robson, P. T. Simpson, C.-G. Wahlström, and M. Zepf. Lateral electron transport in high-intensity laser-irradiated foils diagnosed by ion emission. *Phys. Rev. Lett.*, 98:145001, 2007.

[110] A. Thompson *et al.* *X-Ray Data Booklet*. Center for X-Ray Optis and Advanced Light Source, LBNL, 2009.

[111] B. M. Hegelich. *Acceleration of heavy Ions to MeV/nucleon Energies by Ultrahigh-Intensity Lasers*. Phd thesis, Ludwig-Maximilians-Universität München, 2002.

[112] T. Ceccotti, A. Lévy, H. Popescu, F. Réau, P. D'Oliveira, P. Monot, J. P. Geindre, E. Lefebvre, and Ph. Martin. Proton Acceleration with High-Intensity Ultrahigh-Contrast Laser Pulses. *Phys. Rev. Lett.*, 99:185002, 2007.

[113] E. Fourkal, B. Shahine, M. Ding, J. S. Li, T. Tajima, and C.-M. Ma. Particle in cell simulation of laser-accelerated proton beams for radiation therapy. *Med. Phys.*, 29:2788–2798.

[114] F. Nürnberg, M. Schollmeier, E. Brambrink, A. Blažević, D. C. Carroll, K. Flippo, D. C. Gautier, M. Geißel, K. Harres, B. M. Hegelich, , O. Lundh, K. Markey, P. McKenna, D. Neely, J. Schreiber, and M. Roth. Radiochromic film imaging spectroscopy of laser-accelerated proton beams. *Rev. Sci. Instrum.*, 80:033301, 2009.

[115] M. Passoni and M. Lontano. Theory of light-ion acceleration driven by a strong charge separation. *Phys. Rev. Lett.*, 101:115001, 2008.

[116] John M. Dawson. Particle simulation of plasmas. *Rev. Mod. Phys.*, 55:403–447, 1983.

[117] B. M. Hegelich, I. Pomerantz, L. Yin, H. C. Wu, D. Jung, B. J. Albright, D. C. Gautier, S. Letzring, S. Palaniyappan, R. Shah, K. Allinger, R. Hörlein, J. Schreiber, D. Habs, J. Blakeney, G. Dyer, L. Fuller, E. Gaul, E. Mccary, A. R. Meadows, C. Wang, T. Ditmire, and J. C. Fernández. Laser-driven ion acceleration from relativistically transparent nanotargets. *New Journal of Physics*, 15:085015, 2013.

[118] O. Buneman. Instability, turbulence, and conductivity in current-carrying plasma. *Phys. Rev. Lett.*, 1:8–9, 1958.

[119] B. J. Albright, L. Yin, Kevin J. Bowers, B. M. Hegelich, K. A. Flippo, T. J. T. Kwan, and J. C. Fernández. Relativistic Buneman instability in the laser breakout afterburner. *Phys. Plasmas*, 14:094502, 2007.

[120] B. M. Hegelich, D. Jung, B. J. Albright, J. C. Fernandez, D. C. Gautier, C. Huang, T. J. Kwan, S. Letzring, S. Palaniyappan, R. C. Shah, H.-C. Wu, L. Yin, A. Henig, R. Hörlein,

D. Kiefer, J. Schreiber, X. Q. Yan, T. Tajima, D. Habs, B. Dromey, and J. J. Honrubia. Experimental demonstration of particle energy, conversion efficiency and spectral shape required for ion-based fast ignition. *Nucl. Fusion*, 51:083011, 2011.

[121] O. Klimo, J. Psikal, J. Limpouch, and V. T. Tikhonchuk. Monoenergetic ion beams from ultrathin foils irradiated by ultrahigh-contrast circularly polarized laser pulses. *Phys. Rev. ST Accel. Beams*, 11:031301, 2008.

[122] X. Zhang, B. Shen, X. Li, Z. Jin, F. Wang, and M. Wen. Efficient GeV ion generation by ultraintense circularly polarized laser pulse. *Phys. Plasmas*, 14:123108, 2007.

[123] B. Qiao, M. Zepf, M. Borghesi, and M. Geissler. Stable GeV ion-beam acceleration from thin foils by circularly polarized laser pulses. *Phys. Rev. Lett.*, 102:145002, 2009.

[124] A. Henig, S. Steinke, M. Schnürer, T. Sokollik, R. Hörlein, D. Kiefer, D. Jung, J. Schreiber, B. M. Hegelich, X. Q. Yan, J. Meyer-ter Vehn, T. Tajima, P. V. Nickles, W. Sandner, and D. Habs. Radiation-Pressure Acceleration of ion beams driven by circularly polarized laser pulses. *Phys. Rev. Lett.*, 103:245003, 2009.

[125] F. Wagner, C. P. João, J. Fils, T. Gottschall, J. Hein, J. Körner, J. Limpert, M. Roth, T. Stöhlker, and V. Bagnoud. Temporal contrast control at the PHELIX petawatt laser facility by means of tunable sub-picosecond optical parametric amplification. *Appl. Phys. B*, pages 1–7, 2013.

[126] L. Yin, B. J. Albright, B. M. Hegelich, and J. C. Fernández. GeV laser ion acceleration from ultrathin targets: The laser break-out afterburner. *Laser and Particle Beams*, 24:291–298, 2006.

[127] A. Macchi, S. Veghini, T. V. Liseykina, and F. Pegoraro. Radiation pressure acceleration of ultrathin foils. *New J. Phys.*, 12:045013, 2010.

[128] T. Bartal, M. E. Foord, C. Bellei, M. H. Key, K. A. Flippo, S. A. Gaillard, D. T. Offermann, P. K. Patel, L. C. Jarrott, D. P. Higginson, M. Roth, A. Otten, D. Kraus, R. B. Stephens, H. S. McLean, E. M. Giraldez, M. S. Wei, D. C. Gautier, and F. N. Beg. Focusing of short-pulse high-intensity laser-accelerated proton beams. *Nature Physics*, 8:139–142, 2012.

[129] B. L. Doyle and P. S. Peercy. Technique for profiling $^{1}$H with 2.5-MeV Van de Graaff accelerators. *Appl. Phys. Lett.*, 34:811–813, 1979.

[130] B. L. Doyle and D. K. Brice. The analysis of elastic recoil detection data. *Nucl. Instrum. Meth. in Physics B*, 35:301–308, 1988.

[131] W. Assmann, H. Huber, C. Steinhausen, M. Dobler, H. Glückler, and A. Weidinger. Elastic recoil detection analysis with heavy ions. *Nucl. Instrum. Meth. B*, 89:131–139, 1994.

[132] K. Harres. *Strahltransport laserbeschleunigter Ionen*. Phd thesis, Technische Universität Darmstadt, 2010.

[133] J. C. Fernández, B. M. Hegelich, J. A. Cobble, K. A. Flippo, S. A. Letzring, R. P. Johnson, D. C. Gautier, T. Shimada, G. A. Kyrala, Y. Wang, C. J. Wetteland, and J. Schreiber. Laser-ablation treatment of short-pulse laser targets: Toward an experimental program on energetic-ion interactions with dense plasmas. *Laser and Particle Beams*, 23:267–273, 2005.

[134] A. Mele, A. Giardini Guidoni, R. Kelly, C. Flamini, and S. Orlando. Laser ablation of metals: Analysis of surface-heating and plume-expansion experiments. *Appl. Surf. Sci.*, 109–110:584–590, 1997.

[135] R. E. Russo, X. Mao, J. J. Gonzalez, and S. S. Mao. Femtosecond laser ablation ICP-MS. *J. Anal. At. Spectrom.*, 17:1072–1075, 2002.

[136] Karl Jousten. *Wutz Handbuch Vakuumtechnik, 10. Auflage*. Vieweg + Teubner, 2010.

[137] B. Rethfeld, K. Sokolowski-Tinten, D. von der Linde, and S. I. Anisimov. Ultrafast thermal melting of laser-excited solids by homogeneous nucleation. *Phys. Rev. B*, 65:092103, 2002.

[138] M. Aeschlimann, M. Bauer, and S. Pawlik. Competing nonradiative channels for hot electron induced surface photochemistry. *Chem. Phys.*, 205:127–141, 1996.

[139] C. A. Schmuttenmaer, M. Aeschlimann, H. E. Elsayed-Ali, R. J. D. Miller, D. A. Mantell, J. Cao, and Y. Gao. Time-resolved two-photon photoemission from Cu(100): Energy dependence of electron relaxation. *Phys. Rev. B*, 50:8957–8960, 1994.

[140] M. N. Polyanskiy. *http://refractiveindex.info, Refractive index database*.

[141] M. Mehlhorn. *Dynamik von CO und $D_2O$ auf Cu(111): Laserinduzierte und thermisch induzierte Prozesse*. Phd thesis, Freie Universität Berlin, 2005.

[142] E. Knoesel, A. Hotzel, T. Hertel, M. Wolf, and G. Ertl. Dynamics of photoexcited electrons in metals studied with time-resolved two-photon photoemission. *Surf. Sci.*, 368(1–3):76–81, 1996.

[143] E. Knoesel, A. Hotzel, and M. Wolf. Ultrafast dynamics of hot electrons and holes in copper: Excitation, energy relaxation, and transport effects. *Phys. Rev. B*, 57:12812–12824, 1998.

[144] W. S. Fann, R. Storz, H. W. K. Tom, and J. Bokor. Electron thermalization in gold. *Phys. Rev. B*, 46:13592–13595, 1992.

[145] S. D. Brorson, J. G. Fujimoto, and E. P. Ippen. Femtosecond electronic heat-transport dynamics in thin gold films. *Phys. Rev. Lett.*, 59:1962–1965, 1987.

[146] S. S. Wellershoff. *Untersuchungen zur Energierelaxationsdynamik in Metallen nach Anregung mit ultrakurzen Laserpulsen*. Phd thesis, Freie Universität Berlin, 2000.

[147] S. I. Anisimov, A. M. Bonch-Bruevich, M. A. El'yashevich, Y. A. Imas, N. A. Pavlenko, and G. S. Romanov. Effect of powerful light fluxes on metals. *Sov. Phys. Tech. Phys.*, 11:945, 1967.

[148] S. I. Anisimov, B. L. Kapeliovich, and T. L. Perel'man. Electron emission from metal surfaces exposed to ultrashort laser pulses. *Sov. Phys. JETP*, 39:375–377, 1974.

[149] C. Kittel. *Introduction to Solid State Physics*. John Wiley & Sons, 1996.

[150] D. S. Ivanov and B. Rethfeld. The effect of pulse duration on the interplay of electron heat conduction and electron-phonon interaction: Photo-mechanical versus photo-thermal damage of metal targets. *Applied Surface Science*, 255:9724–9728, 2009.

[151] Dmitriy S. Ivanov and Leonid V. Zhigilei. Combined atomistic-continuum modeling of short-pulse laser melting and disintegration of metal films. *Phys. Rev. B*, 68:064114, 2003.

[152] S. I. Anisimov and B. Rethfeld. Theory of ultrashort laser pulse interaction with a metal. *Proc. SPIE*, 3093:192–203, 1997.

[153] K. Vestentoft and P. Balling. Formation of an extended nanostructured metal surface by ultra-short laser pulses: single-pulse ablation in the high-fluence limit. *Appl. Phys. A*, 84(1–2):207–213, 2006.

[154] B. Y. Mueller and B. Rethfeld. Relaxation dynamics in laser-excited metals under nonequilibrium conditions. *Phys. Rev. B*, 87:035139, 2013.

[155] V. Bagnoud, B. Aurand, A. A. Blažević, S. Borneis, C. Bruske, B. Ecker, U. Eisenbarth, J. Fils, A. Frank, E. Gaul, S. Goette, C. Haefner, T. Hahn, K. Harres, H.-M. Heuck, D. Hochhaus, D. H. H. Hoffmann, D. Javorková, H.-J. Kluge, T. Kuehl, S. Kunzer, M. Kreutz, T. Merz-Mantwill, P. Neumayer, E. Onkels, D. Reemts, O. Rosmej, M. Roth, T. Stoehlker, A. Tauschwitz, B. Zielbauer, D. Zimmer, and K. Witte. Commissioning and early experiments of the PHELIX facility. *Appl. Phys. B*, 100(1):137–150, 2010.

[156] Physical Electronics. *Technician's Low Profile Ion Pumps (Angle Pole Pieces)*. Component Manual.

[157] Oerlikon Leybold Vacuum. *Totaldruck-Messgeräte*. Mai 2007.

[158] Pfeiffer Vacuum. *Prisma$^{TM}$ QMS 200 Bedienungsanleitung*. 1999.

[159] H. Kollmus, M. Bender, M. C. Bellachioma, E. Mahner, A. Krämer, L. Westerberg, E. Hedlund, O. B. Malyshev, and H. Reich-Sprenger. Measurements on ion-beam loss induced desorption at GSI. *High Intensity and High Brightness Hadron Beams*. Edited by I. Hofmann, J.-M. Lagniel and R. W. Hasse.

[160] H. Kollmus, A. Kraemer, M. Bender, M. C. Bellachioma, H. Reich-Sprenger, E. Mahner, E. Hedlun, L. Westerberg, O. B. Malyshev, M. Leandersson, and E. Edqvist. Energy scaling of the ion-induced desorption yield for perpendicular collisions of Ar and U with stainless steel in the energy range of 5 and 100 MeV/u. *J. Vac. Sci. Technol. A*, 27(2):245–247, 2009.

[161] M. Bender. *Untersuchung der Mechanismen Schwerioneninduzierter Desorption an Beschleunigerrelevanten Materialien*. Phd thesis, Johann Wolfgang Goethe-Universität Frankfurt, 2008.

[162] M. Bender, H. Kollmus, and W. Assmann. Desorption yields of differently treated copper samples characterized with ERDA. *Nucl. Instrum. Meth. B*, 256:387–391, 2007.

[163] H. Kollmus, M. Bender, W. Assmann, A. Krämer, M.C. Bellachioma, and H. Reich-Sprenger. Heavy ion-induced desorption investigations using UHV-ERDA . *Vacuum*, 82(4):402 – 407, 2007. Proceed. Conf. Vacuum Based Science and Technology.

[164] G. Hoffmeister, M. Bender, H. Kollmus, R. Jaeger, F. Wagner, M. Wengenroth, B. Zielbauer, and M. Roth. Target surface cleaning by fs laser desorption at PHELIX. *GSI Scientific Report*, PNI-INHOUSE-EXP-14, 2012.

[165] S. Nolte, C. Momma, H. Jacobs, A. Tünnermann, B. N. Chichkov, B. Wellegehausen, and H. Welling. Ablation of metals by ultrashort laser pulses. *J. Opt. Soc. Am. B*, 14(10):2716–2722, 1997.

[166] B. H. Christensen, K. Vestentoft, and P. Balling. Short-pulse ablation rates and the two-temperature model. *Appl. Surf. Sci.*, 253(15):6347 – 6352, 2007. Proceedings of the Fifth International Conference on Photo-Excited Processes and Applications (5-ICPEPA).

[167] B. Y. Mueller and B. Rethfeld. Nonequilibrium electron-phonon coupling after ultrashort laser excitation of gold. *Appl. Surf. Sci.*, 302:24–28, 2014.

[168] M. Bonn, D. N. Denzler, S. Funk, M. Wolf, S.-S. Wellershoff, and J. Hohlfeld. Ultrafast electron dynamics at metal surfaces: Competition between electron-phonon coupling and hot-electron transport. *Phys. Rev. B*, 61:1101–1105, 2000.

[169] Prof. Dr. E. Lux. *Berechnung von Durchgangswahrscheinlichkeiten bzw. Leitwerten für verschiedene vakuumtechnische Bauelemente bei Molekularströmung mit dem Monte-Carlo-Verfahren*. Version 2.0.

[170] I. Bodea. Untersuchung der Kontaminationsschicht auf Metalloberflächen mittels Femtosekunden-Laserdesorption, 2014. Bachelor thesis.

[171] J. A. Prybyla, T. F. Heinz, J. A. Misewich, M. M. T. Loy, and J. H. Glownia. Desorption induced by femtosecond laser pulses. *Phys. Rev. Lett.*, 64:1537–1540, 1990.

[172] J. R. Gibson and S. Taylor. Prediction of quadrupole mass filter performance for hyperbolic and circular cross section electrodes. *Rapid Communications in Mass Spectrometry*, 14(18):1669–1673, 2000.

[173] J. Maier. *Instrumentelle Analytik: Massenspektrometrie MS*. `http://w3-o.hm.edu/fb06/professoren/maier/analytik/Blaetter/N151_MS_GrundlagenTrennsysteme_c_BAneu.pdf`.

[174] M. C. Cowen, W. Allison, and J. H. Batey. Electron space charge effects in ion sources for residual gas analysis. *Meas. Sci. Technol.*, 4(1):72, 1993.

[175] M. Schollmeier, S. Becker, M. Geißel, K. A. Flippo, A. Blažević, S. A. Gaillard, D. C. Gautier, F. Grüner, K. Harres, M. Kimmel, F. Nürnberg, P. Rambo, U. Schramm, J. Schreiber, J. Schütrumpf, J. Schwarz, N. A. Tahir, B. Atherton, D. Habs, B. M. Hegelich, and M. Roth. Controlled transport and focusing of laser-accelerated protons with miniature magnetic devices. *Phys. Rev. Lett.*, 101:055004, 2008.

[176] K. Harres, I. Alber, A. Tauschwitz, V. Bagnoud, H. Daido, M. Günther, F. Nürnberg, A. Otten, M. Schollmeier, J. Schütrumpf, M. Tampo, and M. Roth. Beam collimation and transport of quasineutral laser-accelerated protons by a solenoid field. *Phys. Plasmas*, 17:023107, 2010.

[177] H. Schwoerer, S. Pfotenhauer, O. Jäckel, K.-U. Amthor, B. Liesfeld, W. Ziegler, R. Sauerbrey, K. W. D. Ledingham, and T. Esirkepov. Laser-plasma acceleration of quasi-monoenergetic protons from microstructured targets. *Nature*, 439:445–448, 2006.

[178] S. S. Mao, F. Quéré, S. Guizard, X. Mao, R. E. Russo, G. Petite, and P. Martin. Dynamics of femtosecond laser interactions with dielectrics. *Appl. Phys. A*, 79:1695–1709, 2004.

[179] J. D. Bonlie, F. Patterson, D. Price, B. White, and P. Springer. Production of $> 10^{21}$ W/cm$^2$ from a large-aperture Ti:sapphire laser system. *Appl. Phys. B*, 70:S155–S160, 2000.

[180] https://jlf.llnl.gov/. LLNL - Jupiter Laser Facility Group. 2014.

[181] C. E. Clayton, J. E. Ralph, F. Albert, R. A. Fonseca, S. H. Glenzer, C. Joshi, W. Lu, K. A. Marsh, S. F. Martins, W. B. Mori, A. Pak, F. S. Tsung, B. B. Pollock, J. S. Ross, L. O. Silva, and D. H. Froula. Self-guided Laser Wakefield Acceleration beyond 1 GeV using ionization-induced injection. *Phys. Rev. Lett.*, 105:105003, 2010.

[182] P. Patel. Science at the Jupiter Laser Facility - NIF/Jupiter User Group Meeting. *LLNL-PRES-417830*, 2009.

[183] D. Offermann. *The effect of erbium hydride on the conversion efficiency to accelerated protons from ultra-short pulse laser irradiated foils*. Phd thesis, The Ohio State University, 2008.

[184] M. J. Butson, P. K. N. Yu, T. Cheung, and P. Metcalfe. Radiochromic film for medical radiation dosimetry. *Materials Science and Engineering: R: Reports*, 41:61–120, 2003.

[185] http://www.ashland.com/products/gafchromic-radiotherapy-films. *Gafchromic$^{TM}$ radiotherapy films*. 2014.

[186] http://www.elimpex.com/new/products/radiation_therapy/Gafchromic/content/GAFCHROMIC%20MD-V2-55.pdf. *GAFCHROMIC® MD-V2-55 Radiochromic Dosimetry Film for High-Energy Photons*. 2010.

[187] W. L. McLaughlin, M. Al-Sheikhly, D. F. Lewis, A. Kovács, and L. Wojnárovits. Radiochromic solid-state polymerization reaction: Irradiation of polymers, fundamentals and technological applications.

[188] J. P. Biersack, J. F. Ziegler, and U. Littmark. *The Stopping and Range of Ions in Matter*. Pergamon Press, 1985.

[189] M. M. Günther, A. Britz, R. J. Clarke, K. Harres, G. Hoffmeister, F. Nürnberg, A. Otten, A. Pelka, M. Roth, and K. Vogt. NAIS: Nuclear activation-based imaging spectroscopy. *Rev. Sci. Instrum.*, 84:073305, 2013.

[190] K. Harres, M. Schollmeier, E. Brambrink, P. Audebert, A. Blažević, K. Flippo, D. C. Gautier, M. Geißel, B. M. Hegelich, F. Nürnberg, J. Schreiber, H. Wahl, and M. Roth. Development and calibration of a Thomson parabola with microchannel plate for the detection of laser-accelerated MeV ions. *Rev. Sci. Instrum.*, 79:093306, 2008.

[191] J. L. Wiza. Microchannel plate detectors. *Reprint from Nucl. Instrum. Meth.*, 162:587–601, 1979.

[192] A. P. Fews. Fully automated image analysis of etched tracks in CR-39. *Nuclear Instruments and Methods in Physics Research Section B: Beam Interactions with Materials and Atoms*, 71:465 – 478, 1992.

[193] B. Aurand, F. Klos, M. Weipert, P. D. Eversheim, and T. Kühl. Development and Test of New Thomson-Parabolas for Laser-Ion-Acceleration. *GSI Scientific Report*, PNI-PP-18:423, 2010.

[194] D. C. Carroll, P. Brummitt S. Bandyopadhyay, K. Jones, F. Lindau, O. Lundh, D. Neely, L. Robson, P. McKenna, and C.-G. Wahlström. The design, development and use of a novel Thomson spectrometer for high resolution ion detection. *Central Laser Facility Annual Report*.

[195] I. J. Paterson, R. J. Clarke, N. C. Woolsey, and G. Gregori. Image plate response for conditions relevant to laser-plasma interaction experiments. *Meas. Sci. Technol.*, 19(9):095301, 2008.

[196] A. Otten. Modellierung des Ausleseprozesses von CR-Bildplatten, 2007. Diplomarbeit.

[197] D. Kraus. *Characterization of phase transitions in warm dense matter with X-ray scattering*. Phd thesis, Technische Universität Darmstadt, 2012.

[198] A. L. Meadowcroft, C. D. Bentley, and E. N. Stott. Evaluation of the sensitivity and fading characteristics of an image plate system for x-ray diagnostics. *Rev. Sci. Instrum.*, 79:113102, 2008.

[199] CST GmbH. *https://www.cst.com/Products/CSTEMS*. 2014.

[200] M. Roth, E. Brambrink, P. Audebert, A. Blažević, R. Clarke, J. Cobble, T. E. Cowan, J. Fernández, J. Fuchs, M. Geißel, D. Habs, M. Hegelich, S. Karsch, K. Ledingham, D. Neely, H. Ruhl, T. Schlegel, and J. Schreiber. Laser accelerated ions and electron transport in ultra-intense laser matter interaction. *Laser and Particle Beams*, 23:95–100, 3 2005.

[201] R. Nuter, L. Gremillet, E. Lefebvre, A. Lévy, T. Ceccotti, and P. Martin. Field ionization model implemented in PIC code and applied to laser-accelerated carbon ions. *Phys. of Plasmas*, 18:033107, 2011.

[202] H. Ueda, Y. Omura, H. Matsumoto, and T. Okuzawa. A study of the numerical heating in electrostatic particle simulations. *Computer Physics Communications*, 79(2):249 – 259, 1994.

[203] M. Bender, H. Kollmus, H. Reich-Sprenger, M. Toulemonde, and W. Assmann. An inelastic thermal spike model to calculate ion induced desorption yields. *Nucl. Instrum. Meth. in Phys. Research B*, 267:885–890, 2009.

[204] R. Castaing. Electron probe microanalysis. volume 13 of *Advances in Electronics and Electron Physics*, pages 317 – 386. Academic Press, 1960.

[205] T. Meyer-Kuckuk. *Atomphysik*. B. G. Teubner, 1980.

[206] Y. J. Yoon, K. W. Kim, H. K. Baik, S.-W. Jang, and S.-M. Lee. Effects of catalytic surface layer on Zr-based alloy getters for hydrogen absorption. *Thin Solid Films*, 350:138–142, 1999.

[207] G. Gaussorgues. *Infrared Thermography*. Springer-Verlag.

[208] InfraTec GmbH. *http://www.infratec.de/de/thermografie/waermebildkameras.html*. 2014.

# Publications


1. S. Busold, A. Almomani, V. Bagnoud, W. Barth, S. Bedacht, A. Blažević, O. Boine-Frankenheim, C. Brabetz, T. Burris-Mog, T.E. Cowan, O. Deppert, M. Droba, H. Eickhoff, U. Eisenbarth, K. Harres, **G. Hoffmeister**, I. Hofmann, O. Jaeckel, R. Jaeger, M. Joost, S. Kraft, F. Kroll, M. Kaluza, O. Kester, Z. Lecz, T. Merz, F. Nürnberg, H. Al-Omari, A. Orzhekhovskaya, G. Paulus, J. Polz, U. Ratzinger, M. Roth, G. Schaumann, P. Schmidt, U. Schramm, G. Schreiber, D. Schumacher, T. Stoehlker, A. Tauschwitz, W. Vinzenz, F. Wagner, S. Yaramyshev, B. Zielbauer, *Shaping laser accelerated ions for future applications - The LIGHT collaboration*, Nucl. Instrum. Meth. A **740**, 94 (2014)

2. **G. Hoffmeister**, C. Bellei, K. Harres, D. Ivanov, D. Kraus, A. Pelka, B. Rethfeld, G. Schaumann and M. Roth, *Influence of fs-laser desorption on target normal sheath accelerated ions*, Phys. Rev. ST Accel. Beams **16**, 041304 (2013)

3. M. M. Günther, A. Britz, R. J. Clarke, K. Harres, **G. Hoffmeister**, F. Nürnberg, A. Otten, A. Pelka, M. Roth and K. Vogt, *NAIS - Nuclear activation-based imaging spectroscopy*, Rev. Sci. Instrum. **84**, 073305 (2013)

4. **G. Hoffmeister**, C. Bellei, K. Harres, D. Ivanov, D. Kraus, A. Pelka, B. Rethfeld, G. Schaumann and M. Roth, *Effects of fs-laser desorption on the target normal sheath acceleration*, AIP Conf. Proceed. **1464**, 418 (2012)

5. T. Burris-Mog, K. Harres, F. Nürnberg, S. Busold, M. Bussmann, O. Deppert, **G. Hoffmeister**, M. Joost, M. Sobiella, A. Tauschwitz, B. Zielbauer, V. Bagnoud, T. Herrmannsdoerfer, M. Roth and T. E. Cowan, *Laser accelerated protons captured and transported by a pulse power solenoid*, Phys. Rev. ST Accel. Beams **14**, 121301 (2011)

# Danksagung

Am Schluss dieser Arbeit möchte ich mich ganz herzlich bei all denjenigen Personen bedanken, die zum Gelingen dieser Arbeit in vielfältiger Art und Weise beigetragen haben.

An erster Stelle gilt mein ganz besonderer Dank Herrn Prof. Dr. Markus Roth, unter dessen Leitung diese Arbeit entstand. Er ermöglichte mir das Erstellen dieser Arbeit in seiner Arbeitsgruppe, betreute sie fachlich, und stellte die großzügigen finanziellen Rahmenbedingungen, insbesondere die Reisemittel für die im Rahmen dieser Arbeit durchgeführten Experimente in den USA, zur Verfügung.

Frau Prof. Dr. Christina Trautmann möchte ich ganz herzlich danken für die Übernahme des Zweitgutachtens dieser Doktorarbeit und für das Zur-Verfügung-Stellen einzelner ihrer Mitarbeiter für meine Forschungszwecke. Ferner möchte ich Herrn Prof. Dr. Robert Roth und Herrn Prof. Dr. Gerhard Birkl herzlich danken für die Übernahme eines Teils der Doktorprüfung.

Einen wesentlichen Beitrag zum Gelingen dieser Arbeit hat Herr Dr. Markus Bender geleistet, dem ich für sein großes Engagement und seine unermüdliche Geduld ganz herzlich danke. Er stand mit herausragender Tatkraft, guten Ratschlägen und Motivation zur Seite sowohl bzgl. experimenteller Belange als auch beim Korrigieren dieser Doktorarbeit. Ebenso bedanke ich mich bei den Herren Dr. Holger Kollmus, Dipl. Phys. Marc Wengenroth und Lukas Urban für deren Hilfe bei Experimenten zur Desorptionsmessung und bei Herrn Dr. Holger Kollmus zusätzlich für seine Hilfestellung bzgl. vakuumtechnischer Angelegenheiten.

Bei Herrn Dr. Gabriel Schaumann bedanke ich mich dafür, dass er stets mit Rat und Tat bzgl. der Targetherstellung zur Seite stand. Weiterhin danke ich Herrn Peter Hilz sowie den Frauen Dr. Bettina Lommel und Vera Yakusheva für ihre Unterstützung bei der Targetherstellung sowie Targetanalyse.

Frau Dr. Rachel Nuter danke ich für ihre theoretische Unterstützung bzgl. der Simulationsrechnungen zu den gewonnenen experimentellen Daten sowie zu lehrreichem Gedankenaustausch. Bei Frau Prof. Dr. Bärbel Rethfeld bedanke ich mich herzlich für hilfreiche und lehrreiche Diskussionen zur theoretischen Vorstellung der fs-Laserdesorption sowie für die zusammen mit Herrn Dr. Dmitry Ivanov durchgeführten numerischen Berechnungen zur Bestimmung der Plasmaschwelle.

Special thanks goes to the crew of the Jupiter Laser Facility for their technical and organisational support during both experiments at the Callisto laser, especially to Dr. Jim Bonlie and Steven Maricle. Furthermore, I deeply thank Prof. Dr. Robert Cauble for his shown large trust, his steady cooperativeness and his excellent guiding tour at the National Ignition Facility.

Mein weiterer Dank gilt Herrn Dr. Bernhard Zielbauer für seine technische Unterstützung und Hilfsbereitschaft während des Desorptionsexperiments am PHELIX Laser, ebenso wie Herrn Dr. Vincent Bagnoud für die Genehmigung des letzteren.

Herrn Prof. Dr. Peter Mulser danke ich herzlich für seine große und unermüdliche Einsatzbereit-

schaft, uns Studenten die theoretischen Grundlagen der Laser-Plasmaphysik näherzubringen.

Bei allen Mitgliedern unserer Arbeitsgruppe Laser-Plasmaphysik möchte ich mich vielmals bedanken für das nette Arbeitsklima und die Begleitung durch diese Arbeit auf unterschiedliche Weise in den letzten Jahren. Ein ganz besonderer Dank geht hier an Herrn Dr. Abel Blažević, der mit hilfreichen Korrekturvorschlägen zu dem Gelingen dieser Arbeit beitrug, immer ein offenes Ohr für jegliche Belange von uns Studenten hatte und auf dessen Hilfe man sich stets verlassen konnte. Weiterhin gilt mein besonderer Dank den Herren Dipl. Phys. Robert Jaeger und M. Sc. Florian Wagner für die tatkräftige experimentelle Unterstützung und ihr eingebrachtes Interesse, M. Sc. Oliver Deppert u.a. für seine Hilfe bei allen computertechnischen Angelegenheiten sowie M. Sc. Stefan Bedacht für das Korrekturlesen einzelner Passagen dieser Doktorarbeit.
Meinen Bachelorstudenten Kurt Leimeister und Isabella Bodea danke ich für ihr Mitwirken bei der Datenauswertung des Desorptionsexperiments und für anregende Diskussionen.

Zu guter Letzt gilt mein Dank auch vielen Einzelpersonen fern des physikalischen Umfelds, die mich auf meinem Weg durch die Promotionsphase auf verschiedenste Art begleitet haben.
In erster Linie danke ich meiner Mutter, die mir das Studium der Physik möglich machte und mir in all den Jahren jederzeit mit Geduld und Verständnis zur Seite stand.
Meiner Freundin Valentina Bevacqua danke ich ganz herzlich für die vielen aufmunternden Worte aus der Ferne, ebenso wie meiner Freundin Stefanie Schmahl.
Ganz besonders möchte ich mich bei einem Menschen bedanken, der mich in den letzten Jahren nicht nur als Lauftrainer immerzu mit viel Geduld motiviert hat und mich nach Niederlagen wieder aufgebaut hat, sondern der mir auch im Leben fern des Laufsports viel Kraft gegeben hat, meinen Weg weiterzugehen und mir viele Lebensweisheiten mit auf diesen Weg gegeben hat. Danke, Abdel Graine! Choukran!

# Lebenslauf

## Persönliche Daten

| | |
|---|---|
| Name: | Gabriele Hoffmeister |
| Anschrift: | Inselstr. 17<br>64287 Darmstadt |
| Geburstag/-ort: | 09.03.1984, Darmstadt |
| Nationalität: | deutsch |
| Familienstand: | ledig |

## Ausbildung

| | |
|---|---|
| seit 11/2009 | Promotionsstudium an der Technischen Universität Darmstadt, Institut für Kernphysik, AG Prof. Dr. M. Roth<br>Titel: *Influencing laser-accelerated ions by femtosecond-laser desorption* |
| 2007–2009 | Master Thesis an der TU Darmstadt,<br>Titel: *Nonthermal fixed points and the functional renormalization group*<br>Betreuer: Prof. Dr. Jürgen Berges<br>Abschlussnote sehr gut (1,3) |
| 2006–2007 | Studium des Master of Physics (1. Studienjahr) an der Università di Pisa, ERASMUS-Austauschjahr |
| 2003–2006 | Studium des Bachelor of Physics an der TU Darmstadt,<br>Bachelor Thesis Titel: *Energiekalibration des pn-CCD-Detektors des CERN Axion Solar Telescope (CAST)*<br>Betreuer: Prof. Dr. Dr. h.c./RUS Dieter Hoffmann<br>Abschlussnote sehr gut (1,5) |
| 1994–2003 | Edith-Stein-Schule Darmstadt, Abschluss mit Abitur (NC 1,1) |

## Arbeitserfahrung

| | |
|---|---|
| ab 11/2009 | wissenschaftliche Mitarbeiterin am Institut für Kernphysik, TU Darmstadt<br>Betreuerin des Fortgeschrittenen-Praktikums, Seminarbetreuung von Studenten/-innen, Betreuung von Bachelor-Studenten |
| 2005–2009 | Operateur am Elektronenbeschleuniger S-DALINAC, Institut für Kernphysik, TU Darmstadt, Aussetzung während Auslansstudium |
| 2000–2006 | Nachhilfelehrerin in Physik, Mathematik (sowie Latein und Englisch) |

## Auslandsaufenthalte

| | |
|---|---|
| seit 11/2009 | mehrwöchige Aufenthalte zur Experimentdurchführung:<br>Los Alamos National Laboratory (LANL), New Mexico, USA<br>Lawrence Livermore National Laboratory (LLNL), California, USA<br>Kurzaufenthalte zur Konferenz am GANIL, Caen, Frankreich und Hirschegg, Österreich |

# Erklärung zur Dissertation

Hiermit versichere ich, die vorliegende Dissertation ohne Hilfe Dritter nur mit den angegebenen Quellen und Hilfsmitteln angefertigt zu haben. Alle Stellen, die aus Quellen entnommen wurden, sind als solche kenntlich gemacht. Diese Arbeit hat in gleicher oder ähnlicher Form noch keiner Prüfungsbehörde vorgelegen.

Darmstadt, den 07. August 2014

_____

(Gabriele Hoffmeister)